STABILITY AND OBJECTIVITY OF A BUBBLY AND SLUG FLOW TWO-FLUID MODEL WITH WAKE ENTRAINMENT

by

Krishna Chaitanya Chetty Anamala

A Dissertation

Submitted to the Faculty of Purdue University

In Partial Fulfillment of the Requirements for the degree of

Doctor of Philosophy

School of Nuclear Engineering

West Lafayette, Indiana

December 2020

THE PURDUE UNIVERSITY GRADUATE SCHOOL
STATEMENT OF COMMITTEE APPROVAL

Dr. Martin Lopez de Bertodano, Chair

School of Nuclear Engineering

Dr. Alejandro Clausse

School of Nuclear Engineering

Dr. Mamoru Ishii

School of Nuclear Engineering

Dr. Gregory Blaisdell

School of Aeronautics and Astronautics

Dr. Allen Garner

School of Nuclear Engineering

Approved by:

Dr. Seungjin Kim

ACKNOWLEDGMENTS

I am thankful for my advisors Dr. Martin Lopez de Bertodano and Dr. Alejandro Clausse for their patience, guidance and encouragement during my doctoral studies at Purdue University. I wish to convey my gratitude to Dr. Mamoru Ishii and Dr. Allen Garner for helping to improve and complete the presented work. I am particularly grateful for the graduate level course AAE 511 taught by Dr. Gregory Blaisdell, as it piqued the interest within me to pursue mathematically rigorous graduate research. I would like to express my appreciation for my wife Angela Chetty, parents Bhaskara and Sumitha Chetty and in-laws David and Joan Carpenter, who provided me with the required support and encouragement to complete my graduate studies. I am indebted to my senior colleagues Dr. Avinash Vaidheeswaran and Dr. William Fullmer, who encouraged and guided me during the initial stages of my doctoral research. My life at Purdue University would not have been colorful and complete without the presence of the Briggs, the Klaasens, the Carrs, and the Blackwoods. The research work presented here was initially funded by Bechtel Marine Propulsion Corporation (Bettis Laboratory), so I would like to thank Dr. Buchanan and his team for their assistance.

TABLE OF CONTENTS

LIST OF TABLES

LIST OF FIGURES

LIST OF ABBREVIATIONS

CFD	Computational Fluid Dynamics
FFT	Fast Fourier Transform
IVP	Initial Value Problem
KH	Kelvin-Helmholtz
L.H.S	Left Hand Side
PDE	Partial Differential Equation
PDF	Probability Density Function
R.H.S	Right Hand Side
SMART	Sharp and Monotonic Algorithm for Realistic Transport
SWT	Shallow Water Theory
TFM	Two-Fluid Model
UD	Upwind Derivative
VOF	Volume of Fluid
1D	One Dimensional
2D	Two Dimensional

NOMENCLATURE

Latin

$\boldsymbol{A}$	Coefficient Matrix
$\hat{A}$	Action
A_i	Interfacial Area
$\widehat{A_i}$	Interfacial Area Per Unit Projected Area
a	Radius of Sphere
B	Coefficient Matrix
b	Non-dimensional Distance Between Bubble Centers
b_w	Vortex Decay Parameter
C	Eigenvalue
C_w	Propagation Speed of Void Fraction Wave
c	Coefficient
$\check{c}$	Cell Center
$\boldsymbol{D}$	Coefficient Matrix
D	Diameter
E	Elastic Energy Density
e	Unit Vector
F	Source Term
f	Friction factor
G	Gravitational Potential Energy
g	Gravitational Constant
H	Height
I	Identity Matrix
i	Imaginary Unit
J	Drift Flux
j	Superficial Velocity
$\check{j}$	Junction

K	Kinetic Energy Density
k	Wavenumber
$\check{k}$	Kinetic Energy Density Coefficient in Moving Frame
L	Length Scale
$\widetilde{L}$	Lagrangian density
$\hat{L}$	Modified Lagrangian density
m	Inertial Coupling Coefficient
P	Potential Energy Density
p	Pressure
Q	Radial Distribution Function
Re	Reynolds Number
r	Radial Distance
r_p	Gas to Liquid Density Ration
r^*	Non-dimensional Radial Distance
s	Non-dimensional Distance Between Bubbles
t	Time
$\widetilde{U}$	Momentum Density
u	Velocity
u'	Velocity Fluctuation
u^*	Velocity in Moving Frame
V	Voltage
V_{gj}	Drift Velocity
V_w	Kinematic Wave Velocity
w	Relative Velocity
X	Axial Distribution Function
X_0	Vortex Intensity Parameter
x	Axial Distance for 1D Domain
x^*	Axial Distance in Moving Frame
x^+	Modified Axial Distance

Greek

α	Void Fraction
Γ	Inertia
Γ^*	Non-dimensional Inertia
$\dot{\Delta}$	Numerator of Discriminant
ζ	Lagrange Multiplier
θ	Azimuthal Angle
κ	Interfacial Curvature
λ	Wavelength
λ_w	Wavelength of Void Fraction Wave
λ_1	Bulk Kinematic Viscosity of Liquid
ν	Kinematic Viscosity
ρ	Density
σ	Surface Tension Coefficient
τ	Shear Stress
τ_c	Continuous Liquid Phase Time Constant
τ_p	Dispersed Gas Phase Time Constant
ϕ	Velocity Potential
$\underline{\phi}$	State Variable Vector
φ	Polar Angle
χ	Variational Potential Field
Ψ	Flux Limiter Function
$\boldsymbol{\omega}$	Vorticity
ω	Angular Frequency or Growth Rate

Superscripts

B	Basset
$coll$	Collision

D	Drag
exp	Experiment
L	Lift
sim	Simulation
T	Transpose
TD	Turbulent Dispersion
t	Turbulent
Var	Variational
VM	Virtual Mass
W	Wall
WE	Wake Entrainment
$*$	Moving Frame, Non-dimensional
$'$	Gas Void Fraction Derivative

Subscripts

b	Bubble
$coll$	Collision
D	Drag
$eddy$	Eddy Induced
i	Interface
k	Phase Index
L	Lift
lam	Laminar
p	Interfacial Pressure
R	Right
Sato	Model of Sato
$\tilde{u}$	Momentum Density Derivative
vm	Virtual Mass
$Wallis$	Model of Wallis

WE	Wake Entrainment
wall	Wall
0	Initial, Steady State
1, c	Continuous Liquid Phase
$1i$	Continuous Liquid Side Interface
2, p	Dispersed Gas Phase
$2i$	Dispersed Gas Side Interface

ABSTRACT

The current study is aimed at developing a well-posed and objective, i.e., frame invariant, Eulerian one-dimensional (1D) Two-Fluid Model (TFM) to predict flow regime transition from dispersed to clustered bubbly and slug flow for vertical adiabatic two-phase flows. Two-phase flows in general are characterized by local material wave or void fraction wave instabilities and flow regime transitions are one of the important consequences of these instabilities. The physical mechanism of wake entrainment for clustering of dispersed bubbles is proposed, leading to formation of bubble clusters and Taylor bubbles. The focus of the work is on simulation of the local interfacial structures for bubble clusters and Taylor bubbles, using a well-posed, unstable and non-linearly bounded 1D Shallow Water TFM.

The first part of the current study investigates the dynamic behavior of the well posed 1D mechanistic TFM obtained from the averaging approach of Ishii [1], due to wake entrainment instability. For this, a 1D Shallow Water TFM derived from the 1D mechanistic TFM is used, which retains the same dynamic behavior as that of the latter at short wavelengths and the required wake entrainment force is derived mechanistically. Three stability approaches are followed to study the dynamic behavior of the 1D Shallow Water TFM: characteristics, dispersion analysis, and nonlinear numerical simulations. An in-house code is used for the 1D numerical simulations of the growth of void fraction waves due to wake entrainment. The simulation results are validated with the experimental data of Cheng and Azzopardi [2] and Song et al. [3] To conclude the first part, the 1D results of the two-equation Shallow Water TFM are carried over to the complete four-equation TFM for quasi 1D simulations using the commercial CFD code of ANSYS Fluent.

As an alternative to the mechanistic approach, which is based on Newtonian mathematics, a variational approach based on Lagrangian and Hamiltonian mathematics is used in the second part of the thesis. While the mechanistic approach operates in terms of forces acting on the two-phase mixture, the variational approach operates in terms of energies of the two-phase system. To derive the equations of motion using the variational approach, the extended Hamilton principle of least action is applied to the Lagrangian density of the two-phase mixture. One of the appealing features

of this procedure is that the derived equations of motion are objective (Geurst [4]), in particular the added mass terms.

Thus, the second part of the current study focuses on deriving an objective, well-posed and unstable 1D TFM as well as developing a constitutive model for the wake entrainment effect using the variational method. Additional momentum transfer terms present in both the liquid phase and gas phase momentum equations, which render the variational TFM objective, are discussed. The variational method is then used to derive the 1D Shallow Water TFM using the fixed flux assumption. The conservative interfacial momentum transfer terms require formulation of the inertial coupling between the phases. Potential flow theory is first used to derive the inertial coupling coefficient for a single bubble and then for a pair of bubbles to consider interaction between the two bubbles. Then, a lumped parameter model is used to derive the inertial coupling coefficient for the wake entrainment effect. A local drag coefficient is obtained for the non-conservative interfacial drag force from the experimental data using kinematic approximation, i.e., force balance between drag and gravity. The linear and non-linear stability analyses are used to address the stability of the 1D variational Shallow Water TFM. The presence of appropriate short-wave physics makes the 1D Shallow Water TFM hyperbolic well-posed and kinematically unstable. Finally, numerical simulations are performed to demonstrate the development of void fraction waves due wake entrainment. The growth of void fraction waves is non-linearly bounded, i.e., Lyapunov stable. The simulation results are compared with the experimental data to validate the propagation properties of void fraction waves for bubble clusters and Taylor bubbles. This work illustrates the short-wave two-phase flow simulation capability of the TFM for the bubbly to slug flow regime transition.

1. INTRODUCTION

1.1 Significance of Problem

The bubbly and slug flow regimes occur in many industrial applications and predicting these regimes and the bubbly to slug flow regime transition is critical for the safety and reliability of two-phase flow systems. The bubbly flow regime is encountered in thermal hydraulic systems used across, but not limited to, the nuclear, chemical and manufacturing industries. For example, due to the good mixing and heat transfer properties present in the bubbly flow regime, it is used for chemical processes like catalytic cracking and gasification. Within the nuclear industry, the cooling of the reactor core in the boiling water reactor involves bubbly flow. The slug flow regime is one of the characteristic flow patterns in vertical two-phase flows. The slug flow consists of a long-elongated Taylor bubble (Davies and Taylor [5]) with an adjacent liquid film flowing downwards between the bubble and the channel wall. The Taylor bubble has an axially symmetric bullet shape and it occupies almost the entire cross-sectional area of the flow channel. This is followed by the liquid slug region which may or may not have dispersed bubbles present in it. One of the most common scenarios for the slug flow regime is the two-phase flow in pipelines connecting the seabed wells to the production platforms in the oil and gas industry. Slug flow regime is also encountered in boiling water reactors and during emergency core cooling of the nuclear reactor core. The slug flow regime has enhanced heat transfer but it also has pressure fluctuations leading to undesirable vibrations and even water hammer in pipeline flows. Hence, it is important to have good modelling and simulation capabilities that can predict the complex thermo-fluid dynamics associated with bubbly and slug flows for design and development of two-phase flow systems.

Computational Fluid Dynamics (CFD) analysis has been used extensively to simulate two-phase flow regimes. Among a variety of transient two-phase flow models that can be found based on the Eulerian-Eulerian formulation approach, the Two-Fluid Model (TFM) is the most elaborate two-phase flow model that is also practical. In comparison with the Drift Flux Model (DFM) of Ishii [1], the strength of the TFM lies in its capability to simulate both local and system two-phase flow instabilities. This lies in the underlying physical basis on which the DFM and the TFM

formulations differ. The DFM uses a single velocity field for both the phases, which is the center of mass velocity. In addition, the relative velocity between the two-phases in the DFM is fixed by prescribing the drift velocity using a kinematic approximation and this removes the dynamics associated with the relative motion between the two fluids. Though this makes the DFM easier to solve and applicable to simulate the system instabilities, it cannot simulate local instabilities that depend on the relative velocity. On the other hand, since the TFM uses independent velocity fields for each phase, it allows for localized non-equilibrium effects between the two phases to be modelled. Not only does this make the TFM more complete when compared to the DFM, but it makes it complicated by requiring the constitutive relations to define the interfacial transfer terms as well as the number of equations to solve. It also raises the difficulty of ill-posed behavior. It is important to note that the local instabilities are responsible for two-phase flow regime transitions which are transient process and only the TFM can resolve these in comparison to the DFM. To model two-phase flow regime transitions, the TFM used for CFD analysis must account for the flow physics pertaining to relevant local two-phase flow instabilities. In addition, the fundamental property of objectivity, i.e. frame invariance, is also addressed in this thesis.

In general, both the mechanistic and the variational approaches have been used in the past for rigorous derivation of the TFM. The mechanistic TFM is derived using the Newtonian mathematics approach where the fluid flow behavior is analyzed in terms of the forces acting on the fluids. On the other hand, the variational approach falls within the framework of Lagrangian and Hamiltonian mathematics. The variational approach differs from the Newtonian approach as its formulation is based on analyzing the energy of the system as opposed to the forces acting on the system. Any two-phase flow formulation requires constitutive modelling with the constraint of objectivity. Though both the mechanistic and the variational approaches have been used in the past for constitutive modelling, the requirement of objectivity has been a challenge for the mechanistic approach. But the constitutive models obtained from the variational formulation are inherently objective, Geurst [4]. One of the important differences between the two approaches is that though the variational approach provides the analytical equations of motion explicitly, the physical significance of each of the individual terms in terms of forces is not obvious. The mechanistic approach does exactly the opposite, as the physical meaning of each constitutive relation is generally understood, but their analytical form is unknown. It can be stated that the variational

approach provides an alternative way to derive objective constitutive models and the two approaches complement each other.

The mechanistic TFM is the only TFM used for numerical calculations, like in the nuclear reactor safety codes such as RELAP 5 and TRAC use the mechanistic 1D TFM. In contrast, numerical simulations have never been performed using the variational TFM for two-phase flow engineering applications. Much of the literature regarding variational approach deals with the scientific development of the variational TFM and the relation between the mechanistic and the variational TFM. But the work presented here is the first demonstration of the variational approach for constitutive model development, used for performing non-linear simulations of bubbly to slug flow regime transition, relevant for designing engineering systems. The 1D TFM used in the nuclear reactor safety codes is ill-posed due to the local stability of the TFM not being addressed. Moreover, the local instabilities are responsible for two-phase flow regimes transition and this requires accurate modelling of the interfacial momentum transfer mechanisms. It is shown here that the variational modelling approach captures inertial coupling precisely to address the local short-wave linear and non-linear stability of the 1D TFM, which will be beneficial to improve TFM used for nuclear safety assessment.

1.2 Previous Work

A unique feature of the two-phase flow systems is the existence of a broad range of system and local instabilities. The system instabilities are associated with the entire response of the system and occur at the length scale of the entire flow channel. Some examples of these include the density wave instability and flow excursion (Ruspini et al. [6]). The local instabilities are associated with the interaction of the two-phases at the length scale of the local interfacial structures and include the Shallow Water Theory (SWT) or kinematic instability and the Kelvin-Helmholtz (KH) instability (Lopez de Bertodano et al. [7]). The KH instability arises at the interface between two fluids of different densities and velocities and is unique to two-phase flows. The SWT instability is associated with the kinematic waves i.e. continuity waves, and is caused by the interfacial drag forces between the two-phases. This instability arises when the drag experienced by the flow structures decreases as they grow in size and has been extensively studied for single-phase flows (Whitham [8]).

Wallis [9] suggested the use of wave theory for analyzing the propagation of material or void fraction waves to examine flow regime transitions. Several experimental studies have been pursued towards understanding the propagation of the void fraction waves. Nassos and Bankoff [10] were the first to measure the void fraction waves. Mercadier [11] found that bubbly flow exhibited damping of void fractions waves, which decreased with increase in the mean void fraction. Matuszkiewicz et al. [12] performed statistical analysis of void fraction disturbances to prove the existence of a relation between the local void fraction instability and bubbly to slug flow regime transition. Park et al. [13] measured the void fraction wave propagation speeds and amplifications for bubbly clusters in oil-water two-phase flow, implying bubble coalescence and Taylor bubble formation. A more elaborate study on void fraction waves for bubbly to slug flow regime transition was presented by Song et al. [3] and Cheng and Azzopardi [2]. The probability density function (PDF) was used to describe the local void fraction distribution for air-water two-phase flow regimes. The PDF had a single peak for dispersed bubbles, followed by broadening of the PDF and an elongated tail for bubble clusters. For the slug flow regime, the PDF exhibited two distinct peaks: one representing the low void fraction in the liquid slug and the other representing high void fraction in the Taylor bubble region. Furthermore, Park et al. [13] suggested using experimental data about void fraction waves to develop mechanistic models to predict bubbly to slug flow regime transition due to local instabilities. Hence, a two-phase flow Computational Fluid Dynamics (CFD) model should be able to resolve local instabilities to simulate the bubbly to slug flow regime transition.

Numerical simulations of vertical slug flow have been performed in the past. Taha and Cui [14] used the Volume of Fluid (VOF) Model to resolve the shape and flow around Taylor bubbles. Abdulikadir et al. [15] also used the VOF model to simulate development of Taylor bubbles. But the TFM has been scarcely used to simulate the development of Taylor bubbles in vertical slug flows. A 1D TFM was used by Galleni and Issa [16] to simulate development of the Taylor bubbles in vertical channels due to SWT instability. However, it did not have the conservative inertial forces due to virtual mass. In addition, the requirement of objectivity, i.e., frame invariance, was not addressed. Within the mechanistic framework, Ishii and Hibiki [17] provide a comprehensive list of the conservative inertial forces due to virtual mass in the TFM. Drew and Lahey [18] showed that the lift force needs to be added along with the symmetric virtual mass term as an ad-hoc in the

mechanistic TFM to attain objectivity. But Wallis [19] stated that there is always the issue of the same physical mechanism being double counted when the physical mechanisms are included via ad-hoc basis. As an alternative approach for modelling and objectivity, Geurst [4] first applied the variational approach or formulation of the TFM for dispersed bubbly flows. Pauchon and Smereka [20] performed an equivalent variational TFM derivation to Geurst [21]. The variational approach starts from the Lagrangian of the two-phase mixture defined in terms of the averaged variables. The conservative equations of motion are then derived systematically from the Lagrangian by applying the extended Hamilton principle of least action. In the variational TFM, the interfacial momentum transfer terms due to virtual mass require formulation of the inertial coupling coefficient for closure, which accounts for the inertial interactions between the two phases. The potential flow theory was used by Wallis [22], Wijngaarden [23], Smereka and Militon [24] and Kok [25] for formulating the inertial coupling coefficient for dilute and non-dilute bubbly flows. Wallis [22] applied the variational technique to derive the inertial coupling for various flow configurations including potential slug flow. To use the TFM to simulate two-phase flow instabilities, which are physically valid phenomena, the TFM needs to transition from being stable to an unstable model. This is feasible only when appropriate two-phase models are present that account for the inertial coupling between the two-phases.

The stability of the TFM, which is dependent on the mathematical behavior of the governing partial differential equations (PDEs), plays an important role in understanding its capability to simulate two-phase instabilities. Significant issues where found when the one-dimensional (1D) TFM was used to perform CFD analysis in the nuclear reactor safety codes. Gidaspow [26] stated that the 1D TFM without the viscous dissipation terms is ill-posed or elliptic as an Initial Value Problem (IVP) depending on the constitutive models and flow conditions. It is important for any system of governing differential equations for fluid flow to be well-posed, so that a physically meaningful solution is obtained. This led to the common misconception that the TFM is flawed. Historically, the ill-posedness has been addressed by using either excessive numerical damping or adding unphysical closure models implemented to remove the unstable behavior of the TFM. Unfortunately, these methods remove the inherent dynamics associated with the two-phase flows, making the TFM incapable of resolving the very two-phase flow instabilities, which only the TFM can resolve.

The linear stability theory consisting of the charteristic and dispersion analysis has been widely used for understanding the mathematical behavior of the TFM. A model is considered as ill-posed when the growth rate is infinite at zero wavelengths for the two-phase waves. Using characteristic analysis for the compressible TFM, it was shown by Drew and Passman [27] that the problem of ill-posedness is associated with the material waves or the void fraction waves, and not the acoustic as they are always real. This led to change in focus towards the local material wave stability analysis of the TFM. The ill-posedness of the TFM is due to lack of appropriate short-wave physics which get often neglected due to the incomplete averaging and over simplification of the TFM when used for CFD simulations. It is the physical mechanisms operating at short wavelengths, of the scale of the local interfacial structures, that make the TFM well-posed or ill-posed. Lopez de Bertodano et al. [7] stated that the TFM by default has the KH instability embedded in it due to the existence of two independent velocity fields in its fundamental formulation. Ramshaw and Trapp [28] and Pauchon and Banerjee [29] proposed that addition of physically relevant short-wave mechanisms like surface tension and interfacial pressure within the TFM can make it well-posed at least in the linear stability sense while retaining the unstable nature of it leading to material wave growth. It was shown by Barnea and Taitel [30] and Fullmer et al. [31] that the TFM can become unstable due to either kinematic instability (SWT instability) or the dynamic instability (KH instability) or both. But the non-linear stability, in the sense of boundedness of the material wave growth, of the linearly well-posed and unstable TFM was not explored and resolved in detail until the work of Lopez de Bertodano et al. [7] They clearly demonstrated the evolution of the growth of material waves and the inherent chaos associated with their non-linear evolution, while being non-linearly bounded or Lyapunov stable at the same time.

1.3 Outline of the Thesis

The goal of the work presented here is to derive objective constitutive models and address the stability of the 1D TFM to simulate bubbly to slug flow regime transition using a 1D Shallow Water TFM. The wake entrainment phenomenon is proposed as the physical mechanism causing clustering of dispersed bubbles to form bubble clusters and Taylor bubbles. The mechanistic approach towards development of the constitutive models, the linear and nonlinear stability analysis of the time averaged 1D TFM of Ishii [1] is presented first in Section 2. To begin with, the mechanistic TFM is discussed and following Lopez de Bertodano et al. [7], it is demonstrated

that the 1D Shallow Water TFM is an asymptotic case of the 1D TFM. To include appropriate physics relevant for growth of the void fraction waves due to clustering, the wake entrainment force model is developed. This is followed by inclusion of the elastic collision force model to account for the random bubble interactions and viscous diffusion model. To analyze the stability of the TFM, the characteristic and the dispersion analyses are used to determine the nature of the governing PDEs and the local wake entrainment instability, as well as the well-posedness. This is followed by the non-linear stability analysis in which, the numerical method used for the simulations is first described. The numerical simulations of the development of the local interfacial structures for clustered bubbly flow regime are validated with experimental data. The propagation properties of the void fraction waves for bubble clusters are compared with the data. The mechanistic approach is followed by the variational approach in Section 3 to address both the stability and objectivity of the TFM. Following Geurst [4] and Pauchon and Smereka [20], the variational derivation of the 1D TFM is presented. A comparison is made between the variational and the 1D mechanistic TFM to show that there are additional momentum transfer terms in variational TFM making it objective or frame invariant. Then, the variational derivation of 1D Shallow Water TFM of Pauchon and Smereka [20] is presented and modified to include conservative surface tension and gravity forces. The non-conservative interfacial drag force is added as an ad-hoc. It is demonstrated that the variational and mechanistic equations are equivalent when written in terms of the primitive variables. The constitutive models for conservative inertial forces for wake entrainment are developed through formulation of inertial coupling using the lumped parameter model of Wallis [22]. A local drag coefficient is obtained from the experimental data for the interfacial drag force. Similar to the mechanistic approach in Section 2, the linear stability analysis is then used to study the stability of the 1D variational TFM. The well-posed and unstable 1D variational Shallow Water TFM is then solved numerically to show the development of local interfacial structures associated with bubble clusters and Taylor bubbles. The wave propagation properties of the void fraction waves are then compared with experimental data.

2. MECHANISTIC TWO-FLUID MODEL

The Two-Fluid Model (TFM) is the most detailed Eulerian multiphase flow model for two-phase flows. In the TFM, each phase has its own transport equation for conservation of mass, momentum and energy, and these equations are linked through interfacial transfer terms supplemented by the jump conditions. The difficult aspect of modeling two-phase flows using a Eulerian framework is the presence of multiple moving and deformable interfaces based on the flow pattern. Apart from having Navier-Stokes equations for each for the two-phases, matching boundary conditions are required at the interface and local instantaneous formulation ends up being a multi-boundary problem which is mathematically impractical to solve (Ishii and Hibiki [17]). This issue has been tackled by using proper averaging techniques to obtain macroscopic two-phase flows formulation (Ishii and Mishima [32]). The mechanistic approach uses the averaging as the very first step for formulation of the TFM to be applicable for macroscopic analysis of two-phase systems. Three distinct averaging techniques have been used so far for rigorous derivation of the TFM from the local instantaneous governing equations; the ensemble averaging by Drew [33] , time averaging by Ishii [1] and volume averaging by Morel [34]. The averaging procedure filters out the local instantaneous fluctuations of flow variables by averaging across the interface. In essence, the interface is no longer tracked, but the contribution of the interfaces affecting the macroscopic flow is considered in a statistical sense. This is achieved through constitutive relations for the interfacial transfer terms.

The Eulerian time averaging was used by Ishii [1] to formulate the three-dimensional (3D) TFM. The 3D TFM equations for dispersed two-phase vertical flows without phase change are:

$$\frac{\partial}{\partial t}\alpha_k\rho_k + \nabla.\,\alpha_k\rho_k\bar{u}_k = 0 \tag{1}$$

$$\begin{aligned}\frac{\partial}{\partial t}\alpha_k\rho_k\bar{u}_k + \nabla.\,\alpha_k\rho_k\bar{u}_k\,\bar{u}_k \\ = -\alpha_k\nabla\bar{p}_k + \nabla.\,\alpha_k(\bar{\tau}_k + \bar{\tau}_k^t) + \alpha_k\rho_k\bar{g} + \bar{M}_{ki} + (\bar{p}_{ki} - \bar{p}_k)\nabla\alpha_k + (\bar{\tau}_{ki} \\ - \bar{\tau}_k).\nabla\alpha_k\end{aligned} \tag{2}$$

where the index $k = 1$ is for the continuous liquid phase and 2 is for the dispersed gas phase. Here, α_k, ρ_k, $\bar{u}_k$ and $\bar{p}_k$ are the averaged phasic void fraction, density, velocity, and pressure, respectively. Eq. (1) is the continuity or mass conservation equation without mass transfer between

the phases. Eq. (2) is the momentum conservation equation representing the Newtonian principle of rate of change of momentum being equal to net force acting on the system. $\bar{\tau}_k$ and $\bar{\tau}_k^t$ are laminar and turbulent Reynolds stresses in the bulk fluid. and $\bar{\tau}_{ki}$ is the interfacial shear stress. The term $\bar{M}_{ki}$ collectively represents interfacial forces per unit volume, defining the interfacial momentum transfer across the interface. From interfacial jump conditions, the void fractions satisfy

$$\sum_{k=1}^{2} \alpha_k = 0 \tag{3}$$

and the interfacial momentum transfer terms satisfy

$$\sum_{k=1}^{2} \bar{M}_{ki} = 0 \tag{4}$$

which basically means that the interfacial momentum transfer terms for both the phases form an action-reaction pair, satisfying Newton's third law of motion. Depending on the flow regime, the constitutive relations for interfacial momentum transfer terms are different and much of the challenge in two-phase flow modelling is attributed to $\bar{M}_{ki}$ formulation. For a dispersed two-phase mixture, $\bar{M}_{ki}$ in general consists of drag $\bar{M}_{ki}^D$, lift $\bar{M}_{ki}^L$, turbulent dispersion $\bar{M}_{ki}^{TD}$, wall $\bar{M}_{ki}^W$, virtual mass $\bar{M}_{ki}^{VM}$ and Basset force $\bar{M}_{ki}^B$ such that

$$\bar{M}_{ki} = \bar{M}_{ki}^D + \bar{M}_{ki}^L + \bar{M}_{ki}^{TD} + \bar{M}_{ki}^W + \bar{M}_{ki}^{VM} + \bar{M}_{ki}^B \tag{5}$$

A detailed description regarding individual forces within $\bar{M}_{ki}$ can be found in Ishii and Hibiki [17]and only a brief explanation is given here.

The momentum transfer due to virtual mass represents the transient inviscid force acting on the dispersed phase, when it tries to accelerate in a continuum. It defines the additional drag force a bubble experiences when it tries to push liquid behind to move ahead. Following Drew and Lahey [18],

$$\bar{M}_{2i}^{VM} = \alpha_2 \rho_1 c_{vm} \left(\frac{D_1 \bar{u}_1}{Dt} - \frac{D_2 \bar{u}_2}{Dt} \right)$$
$$\frac{D_k}{Dt} = \frac{\partial}{\partial t} + \bar{u}_k \,.\, \nabla \tag{6}$$

where c_{vm} is the virtual mass coefficient and is 1/2 for dilute bubby flows. For void fractions above the dilute limit ($\alpha_1 \rightarrow 1$), interaction between the bubbles becomes significant and its effect on the virtual mass coefficient was formulated by Zuber [35] as

$$c_{vm} = \frac{1}{2}\left(\frac{1+2\alpha_2}{1-\alpha_2}\right) \tag{7}$$

The virtual mass term plays a significant role on the propagation properties of the void fraction waves and hence plays an important role on stability of the TFM.

The distribution of dispersed flow structures is influenced by the pressure between the interface and the bulk region of the fluid. Using potential flow of liquid past a solid sphere, Stuhmiller [36] proposed the following definition for the interfacial pressure difference,

$$\bar{p}_{1i} - \bar{p}_1 = -c_p \rho_1 |\bar{u}_r|^2 \tag{8}$$

with $c_p = 0.25$ for dilute bubbly flows and is a function of α_2 just like the virtual mass coefficient for void fractions higher than the dilute limit. $\bar{u}_r = \bar{u}_2 - \bar{u}_1$ is the relative velocity betweent the gas and liquid phase. According to Drew and Passman [27] the pressure in the bulk region of the dispersed phase is almost equal to the pressure at the interface and hence $\bar{p}_{2i} \approx \bar{p}_1$. Pauchon and Banerjee [29] found that for vertical bubbly flows, the interfacial pressure difference gives real Eigenvalues to the TFM. Just like virtual mass force, the void fraction wave propagation properties are also dependent on the interfacial pressure difference.

The general form of momentum transfer due to steady state drag force is given by,

$$\bar{M}_{ki}^D = -\frac{3}{4}\alpha_2 \rho_1 \frac{c_D}{L_D} |\bar{u}_r| \bar{u}_r \tag{9}$$

where C_D is the interfacial drag coefficient and is a function of void fraction α_2. The definition of C_D is unique for a given flow regime. For example, the c_D for distorted particles is given by (Ishii and Hibiki [17]),

$$c_D = \frac{2D_b}{3}\sqrt{\frac{g\Delta\rho}{\sigma}}\left(\frac{1+17.67\, f(\alpha_2)^{\frac{6}{7}}}{18.67\, f(\alpha_2)}\right)^2 \tag{10}$$

where

$$f(\alpha_2) = (1-\alpha_2)^{1.5} \tag{11}$$

In the above equations, the mean bubble diameter is given by D_b, σ is the surface tension coefficient, and $\Delta\rho = \rho_1 - \rho_2$ is the density difference. In addition, L_D is an appropriate length scale for interfacial drag force and represents the characteristic length scale of the interfacial structures.

Due to the presence of wall surface, liquid flow past a bubble has difference in velocity between the wall side and bulk side of the liquid. This generates a force that pushes bubbles away from the near-wall region and is known as the wall force. Following Antal [37],

$$\bar{M}_{2i}^{W} = -\alpha_2 \rho_1 c_{wall} |\bar{u}_r|^2 \tag{12}$$

The wall coefficient c_{wall} is given by,

$$c_{wall} = min\left\{0, \left(\frac{c_{w1}^{\cdot}}{D_b} + \frac{c_{w2}^{\cdot}}{y_{wall}}\right)\right\} \tag{13}$$

where $c_{w1}^{\cdot}$ and $c_{w2}^{\cdot}$ are constants and D_b is the bubble diameter. The wall force plays an important role in near-wall modelling for CFD and enables realization of physically relevant void fractions in the region closer to the wall.

The presence of bubbles induces additional turbulence in the flow. The turbulent liquid eddies disperse bubbles from regions of higher to lower void fractions and the force representing this phenomenon following Lopez de Bertodano [38] is the turbulent dispersion force defined as

$$\bar{M}_{2i}^{TD} = -c_{TD} \rho_1 k_1 \nabla \alpha_2 \tag{14}$$

where the turbulent dispersion coefficient $c_{TD} = 0.25$ is generally used for bubbly flows.

The velocity gradients in the liquid phase cause transverse displacement of the dispersed flow structures through lift force. Important for the near-wall region, following Drew and Lahey [18] and Auton [39], the lift force is given by,

$$\bar{M}_{2i}^{L} = -\alpha_2 \rho_1 c_L \times (\nabla \times \bar{u}_1) \tag{15}$$

For bubbly flows, the lift coefficient $c_L = 0.25$ and a wide variety of empirical correlations have been proposed by Tomiyama et al. [40] and Frank et al. [41].

Finally, for the continuous liquid phase, the stress terms due to viscous diffusion are represented by,

$$\bar{\tau}_1 + \bar{\tau}_1^t = \rho_1 \left(\nu_{1,net} \left(\nabla \bar{u}_1 + \nabla \bar{u}_1{}^{+}\right) - \left(\frac{2}{3}\nu_{1,net} - \lambda_1\right) \nabla . \bar{u}_1{}^{I}\right) \tag{16}$$

In the above equation, the net effective kinematic viscosity is denoted by $\nu_{1,net}$ and λ_1 is the bulk viscosity of the of the liquid phase.

2.1 1D Two-Fluid Model

The three-dimensional (3D) TFM obtained from averaging the local balance equations describes the phasic interactions in detail. In general, when the flow features are more dominant along the axial direction of the flow channel, a one-dimensional (1D) TFM derived from area averaging the 3D TFM is more convenient. Since this dissertation focuses on the local KH and SWT instabilities in the void fraction, 1D form of the TFM is used as it eliminates the hydrodynamics associated with turbulence. Following Lopez de Bertodano et al. [7], the 1D approximation has been found to be sufficient to address the ill-posed nature of the TFM caused by the lack of short-wave physics. Moreover, 1D approximation helps focus towards development of constitutive relations for interfacial momentum transfer terms and their effect on the stability of the TFM, since these interfacial terms are the most important characteristic feature of the TFM.

The 1D TFM is obtained by area averaging the full 3D TFM. Ishii and Hibiki [17] provide more information regarding the area averaging procedure. For vertical adiabatic and incompressible dispersed two-phase flows, the 1D TFM is given by

$$\frac{\partial \alpha_1}{\partial t} + \frac{\partial}{\partial x}\alpha_1 u_1 = 0 \tag{17}$$

$$\frac{\partial \alpha_2}{\partial t} + \frac{\partial}{\partial x}\alpha_2 u_2 = 0 \tag{18}$$

$$\begin{aligned}\rho_1 \alpha_1 \left(\frac{\partial u_1}{\partial t} + u_1 \frac{\partial u_1}{\partial x}\right) \\ = -\alpha_1 \frac{\partial p_1}{\partial x} + \frac{\partial}{\partial x}\alpha_1(\tau_k + \tau_k^t) - \alpha_1 \rho_1 g - M_{2i}^{VM} - M_{2i}^{D} \\ - (p_{1i} - p_1)\frac{\partial \alpha_1}{\partial x}\end{aligned} \tag{19}$$

$$\rho_2 \alpha_2 \left(\frac{\partial u_2}{\partial t} + u_2 \frac{\partial u_2}{\partial x}\right) = -\alpha_2 \frac{\partial p_{1i}}{\partial x} - \alpha_2 \rho_2 g + M_{2i}^{VM} + M_{2i}^{D} \tag{20}$$

In the above equations, α_k , ρ_k, u_k and p_k are the area averaged phasic void fraction, density, velocity and bulk pressure for phase k. The laminar and turbulent axial liquid shear stresses are denoted by τ_k and τ_k^t respectively. The momentum transfer term due to mass flux is absent as there is no mass transfer. Under the 1D assumption, lift and wall forces are dropped.

2.2 Wake Entrainment

Wake entrainment phenomenon is proposed as the physical mechanism responsible for clustering of dispersed bubbles to form bubbles clusters and slug flow. The bubble in the wake of a leading bubble experiences less drag, which results in the trailing bubbles accelerating and eventually catching up with the leading bubble. It is important to include this mechanism in the TFM formulation to model the flow regime transition from discrete bubbly flow to clustered bubbly and slug flow. As a first order approximation, the momentum transfer term due to wake entrainment is based on linearization of the interfacial drag force term. For a 1D framework, the drag coefficient of churn-turbulent flow from Ishii and Chawla [42], given by

$$c_D = \frac{8}{3}(1-\alpha_2)^2 \tag{21}$$

is used for deriving wake entrainment force from M_{2i}^D.The decreasing trend of drag coefficient in Eq. (21) with increasing α_2 is due to wake entrainment. The interfacial drag force can be linearized with respect to α_2 by

$$M_{2i}^D = M_{2i}^D|_{\alpha_{20}} + M_2^{WE}|_{\alpha_{20}} \tag{22}$$

Using Taylor's expansion and taking into consideration only first order terms,

$$M_{2i}^D = M_{2i}^D|_{\alpha_{20}} + \left.\frac{\partial M_{2i}^D}{\partial \alpha_2}\right|_{\alpha_{20}} \delta\alpha_2 \tag{23}$$

Combining Eqs. (21)-(23) gives the momentum transfer term due to wake entrainment as

$$M_2^{WE} = \rho_1 C_{WE} \frac{L_{WE}}{L_D}(3{\alpha_2}^2 - 4\alpha_2 + 1)u_r^2 \frac{\partial \alpha_2}{\partial x} \tag{24}$$

where linearization of the interfacial drag gives $C_{WE} = 2$. Distinct length scales for the interfacial drag force L_{Drag} and wake entrainment term L_{WE} are proposed for dispersed and clustered bubbly flow regimes. For dispersed bubbly flows, $L_{WE} = 10\ D_b$ and $L_D = D_b$ and $L_{WE} = 20\ D_b$ and $L_D = 2\ D_b$ for clustered bubbly flows and the reader can refer to Appendix A for more details.

2.3 Collision

In addition to the wake entrainment, another important mechanism that needs to be taken into consideration when bubbles interact with each other is collision. The increase in packing fraction with increase in gas flow rate (higher void fraction) increases the bubble collision frequency. The kinetic theory of finite sized particles was developed by Chapman and Cowling [43] using the Enskog kinetic equation. Following their work, several models to account for the collision effect in the field of fluid-particle flows were formulated. For the current work, the model of Alajbegovic et al. [44] for collision induced momentum transfer term M^{coll} is considered,

$$M^{coll} = -\nabla.\left[(\rho_2 + \rho_1 c_{vm})\, q(\alpha_2)\alpha_2^2\left(2\overline{u_2' u_2'} + \overline{u_2'.u_2'}I\right)\right] \tag{25}$$

It is important to note that the collision force term is only valid for the dispersed gas phase momentum equation and hence its action-reaction counterpart is absent in the liquid phase momentum equation. The increase in collision frequency due to increase in void fraction is defined by $q(\alpha_2)$, which is the pair distribution function. Following Carnahan and Starling [45],

$$q(\alpha_2) = \frac{2 - \alpha_2}{2(1 - \alpha_2)^3} \tag{26}$$

Eq. (25) is further simplified to give,

$$M^{coll} = -c_{coll}\rho_1 C_{vm}^2 \nabla.\,[q(\alpha_2)\alpha_2^3 |u_r|^2 I] \tag{27}$$

Assuming an isotropic particle stress tensor (Vaidheeswaran [46]), M^{coll} reduces to following form for the 1D TFM with c_{coll} = 1.8 and more details are given in Appendix B,

$$M^{coll} = -c_{coll}\rho_1 C_{vm}^2 \left[\left(3\alpha_2^2 u_r^2 q(\alpha_2) + \alpha_2^3 u_r^2 \frac{dq(\alpha_2)}{d\alpha_2}\right)\frac{\partial \alpha_2}{\partial x} + 2\alpha_2^3 u_r q(\alpha_2)\frac{\partial u_r}{\partial x}\right] \tag{28}$$

2.4 Viscous Stresses

Following Lopez de Bertodano et al. [38], two viscous diffusion mechanisms, bubble induced and eddy induced viscosity, are taken into consideration using linear superposition. The bubble induced diffusion is given by the bubble induced viscosity ν_{Sato} of Sato [47] and, likewise, the

eddy diffusivity ν_{eddy} is based on Prandtl's mixing length model (Pope [48]). Hence, the net effective kinematic viscosity follows,

$$\begin{aligned} \nu_{1,net} &= \nu_{lam} + \nu_{Sato} + \nu_{eddy} \\ \nu_{lam} &= 1.03 \times 10^{-6} \\ \nu_{Sato} &= c_{Sato}|u_r|D_b\alpha_2 \\ \nu_{eddy} &= \left(\frac{D_{pipe}}{10}\right)|u_r| \end{aligned} \tag{29}$$

where $c_{Sato} = 0.6$, D_{pipe} and D_b are the pipe and bubble diameters. The importance of viscous diffusion mechanism will be discussed in the linear stability analysis.

2.5 1D Shallow Water Two-Fluid Model

As stated earlier, the TFM has the capability to resolve both system/global and local instabilities. To focus solely on the local void fraction wave instabilities, an asymptotic case of the 1D TFM was presented by Lopez de Bertodano et al. [7] for dispersed two-phase flows by using the fixed-flux assumption. The full 4-equation 1D TFM was then reduced to a 2-equation Shallow Water TFM. This greatly simplified the analysis of the two local instabilities, i.e., the KH and SWT/kinematic instabilities for adiabatic incompressible two-phase flows.

The 1D TFM presented in the previous section for adiabatic dispersed two-phase flows serves as the starting point for derivation of the Shallow Water TFM. The first step involves adding the two continuity equations without phase change to obtain

$$\frac{\partial}{\partial t}(\rho_1\alpha_1 + \rho_2\alpha_2) + \frac{\partial}{\partial x}(\rho_1\alpha_1u_1 + \rho_2\alpha_2u_2) = 0 \tag{30}$$

The next step is to subtract the liquid momentum equation Eq. (19) and the gas momentum equation Eq. (20) as,

$$\begin{aligned} \left(1 + \frac{c_{vm}}{\alpha_1}\right)\frac{D_1}{Dt}\rho_1u_1 - \left(1 + \frac{c_{vm}}{r_p\alpha_1}\right)\frac{D_2}{Dt}\rho_2u_2 + \frac{\partial}{\partial x}c_p\rho_1(u_2 - u_1)|u_2 - u_1| \\ + \frac{c_p\rho_1(u_2 - u_1)^2}{\alpha_1}\frac{\partial\alpha_1}{\partial x} = -(\rho_1 - \rho_2)|g| + \frac{M_{2i}^D}{\alpha_1\alpha_2} \end{aligned} \tag{31}$$

where $r_p = \rho_2/\rho_1$. The fixed flux condition is obtained when the incompressible (constant densities) and adiabatic flow conditions (no phase change) are imposed. Then sum of the continuity equations using $\alpha_1 + \alpha_2 = 1$ constraint follows,

$$\frac{\partial}{\partial t}(\alpha_1 + \alpha_2) + \frac{\partial}{\partial x}(\alpha_1 u_1 + \alpha_2 u_2) = \frac{\partial}{\partial x}(\alpha_1 u_1 + \alpha_2 u_2) = \frac{\partial j}{\partial x} = 0 \tag{32}$$

From Eq. (32), it can be seen that the net volumetric flux of the two-phase mixture is only a function of time, i.e., $j(x,t) = j(t)$ and is constant at every axial location of the 1D domain. Now the fixed-flux condition is obtained when it is further assumed that the net volumetric flux *j* is independent of time such that $j(x,t) = j_0 = constant$. In vector form, $\nabla.\boldsymbol{j} = 0$ is equivalent to the incompressible single-phase flow condition of the divergence of the of velocity being zero. Physically, from Ishii and Hibiki [49] (Eq. (13-88) of Chapter-13), the fixed-flux condition means that there is no change in the volumetric flux due to the amount of phase change and compressibility of the two-phase flow. This renders the flow adiabatic (no heat transfer) and isochoric (constant density). An important consequence of the fixed-flux assumption is that the flow dynamics associated with net change in the volumetric flux due to large acoustic interactions (from sudden pressurization or depressurization) and mass generation, which cause long wave system instabilities like level swell and density wave instabilities, are eliminated. Furthermore, the TFM momentum equations are reduced to a single equation, representing the two phases together as a pseudo fluid and solves for the relative velocity between the phases. This is essential for addressing the ill-posedness issue of the TFM, which is a local short-wave stability problem.

To obtain the Shallow Water TFM equations, the two PDEs from the sum of the continuity equations and the difference of the momentum equations are recast into

$$\frac{d}{dt}\underline{\psi} + \frac{d}{dx}\underline{\Phi} = \underline{\zeta} \tag{33}$$

where

$$\underline{\psi} = \begin{bmatrix} \rho_1\alpha_1 + \rho_2\alpha_2 \\ \left(1 + \frac{c_{vm}}{\alpha_1}\right)\rho_1 u_1 - \left(1 + \frac{c_{vm}}{r_p\alpha_1}\right)\rho_2 u_2 \end{bmatrix} \tag{34}$$

$$\underline{\Phi} = \begin{bmatrix} \rho_1\alpha_1 u_1 + \rho_2\alpha_2 u_2 \\ \frac{1}{2}\left(1 + \frac{c_{vm}}{\alpha_1}\right)\rho_1 {u_1}^2 - \frac{1}{2}\left(1 + \frac{c_{vm}}{r_p\alpha_1}\right)\rho_2 {u_2}^2 + 2c_p\rho_1(u_2 - u_1)^2 \end{bmatrix} \tag{35}$$

$$\underline{\zeta} = \begin{bmatrix} 0 \\ -(\rho_1 - \rho_2)|g| - \dfrac{f_1}{\alpha_1 D_{pipe}} \rho_1 |u_1| u_1 + \dfrac{M_{2i}^D}{\alpha_1 \alpha_2} \end{bmatrix} \tag{36}$$

Writing the above system of PDEs in terms of the primitive variables $\underline{\varphi} = [\alpha_1, u_1]^T$ gives

$$\boldsymbol{A} \frac{\partial}{\partial t} \underline{\varphi} + \boldsymbol{B} \frac{\partial}{\partial t} \underline{\varphi} = \underline{F} \tag{37}$$

where $\boldsymbol{A} = \boldsymbol{I}$. Using Taylor series expansion of the terms in $\boldsymbol{B}$ for low density ration $r_p \ll 1$ applicable for air-water two-phase mixture, the simplified matrix $\boldsymbol{B}$ will be

$$\boldsymbol{B} \cong \begin{bmatrix} u_1 & \alpha_1 \\ \dfrac{(1+\alpha_1)c_{vm} - c_p}{c_{vm} + \alpha_1 - {\alpha_1}^2} (u_2 - u_1)^2 & u_1 + \dfrac{2\alpha_1 (c_{vm} - c_p)}{c_{vm} + \alpha_1 - {\alpha_1}^2} (u_2 - u_1) \end{bmatrix} \tag{38}$$

and the source term is

$$\underline{F} \cong \begin{bmatrix} 0 \\ -|g| - \dfrac{f_1}{\alpha_1 D_{pipe}} |u_1| u_1 + \dfrac{M_{2i}^D}{\rho_1 \alpha_1 \alpha_2} \end{bmatrix} \tag{39}$$

The 1D mechanistic Shallow Water TFM as an asymptotic case of the 1D TFM using the fixed-flux assumption is,

$$\frac{\partial\, \alpha_1}{\partial t} + u_1 \frac{\partial \alpha_1}{\partial x} + \alpha_1 \frac{\partial u_1}{\partial x} = 0 \tag{40}$$

$$\frac{\partial u_1}{\partial t} + B_{21} \frac{\partial \alpha_1}{\partial x} + B_{22} \frac{\partial u_1}{\partial x} = \frac{\alpha_1 \alpha_2}{c_{vm} + \alpha_1 \alpha_2} \left[-|g| + \frac{M_{2i}^D}{\rho_1 \alpha_1 \alpha_2} \right] \tag{41}$$

where

$$B_{21} = \frac{(1+\alpha_1)c_p - c_{vm}}{c_{vm} + \alpha_1 \alpha_2} {u_r}^2 \tag{42}$$

$$B_{22} = u_1 + \frac{2\alpha_1 (c_{vm} - c_p)}{c_{vm} + \alpha_1 \alpha_2} u_r \tag{43}$$

Now, the addition of the collision force terms modifies the B_{21} and B_{22} as,

$$B'_{21} = B_{21} + \frac{c_{Coll}\, c_{vm}^2\, u_r^2}{\alpha_1^3} \frac{(1-\alpha_1)^2 (3 - \alpha_1^2)}{(c_{vm} + \alpha_1 - \alpha_1^2)} \tag{44}$$

$$B'_{22} = B_{22} - \frac{c_{Coll}\, c_{vm}^2 u_r}{\alpha_1^2} \frac{(1-\alpha_1)^2(1+\alpha_1)}{(c_{vm}+\alpha_1-\alpha_1^2)} \tag{45}$$

Furthermore, when the wake entrainment force terms is included, the coefficient for the void gradient term follows,

$$B"_{21} = B'_{21} + \frac{L_{WE}}{L_{Drag}} c_{WE}\,(3{\alpha_2}^2 - 4\alpha_2 + 1) \frac{1-{\alpha_1}^2}{c_{vm}+\alpha_1-\alpha_1^2} u_r^2 \tag{46}$$

Finally, the second order viscous diffusion term modifies the momentum equation and inclusion completes the 1D mechanistic Shallow Water TFM as,

$$\frac{\partial \alpha_1}{\partial t} + u_1 \frac{\partial \alpha_1}{\partial x} + \alpha_1 \frac{\partial u_1}{\partial x} = 0 \tag{47}$$

$$\frac{\partial u_1}{\partial t} + B_{21} \frac{\partial \alpha_1}{\partial x} + B_{22} \frac{\partial u_1}{\partial x} = \frac{\alpha_1 \alpha_2}{c_{vm}+\alpha_1\alpha_2}\left[-|g| + \frac{M_{2i}^D}{\rho_1 \alpha_1 \alpha_2} + \left(\frac{\nu_{1,net}}{\alpha_1}\right)\frac{\partial}{\partial x}\left(\alpha_1 \frac{\partial u_1}{\partial x}\right)\right] \tag{48}$$

A remarkable feature of the 1D Shallow Water TFM equations in Eqs. (47)-(48) is that their mathematical form is similar to the 1D SWT equations, which have been extensively studied for solving problems dealing with SWT instability and kinematic wave propagation (Whitham [8]). However, in terms of the local physical instabilities, the 1D Shallow Water TFM has the KH instability in addition to the kinematic instability and hence in terms of the stability analysis, it is more complex. Moreover, the two-equation 1D Shallow Water TFM is computationally simpler and less expensive than the full four-equation 1D TFM because it eliminates pressure and provides an elegant mathematical formulation to address the local stability issue of the 1D TFM.

2.6 Linear Stability

A model represented by a system of equations is well-posed if apart from the fact that a solution exists, the solution should be unique based on the flow conditions. The 1D Shallow Water TFM needs to be well-posed and unstable to be able to simulate flow regime transitions due to the presence of local instabilities. Following Ishii and Hibiki [17], the number of unknows in the TFM can be as high as 33 and formulation of constitutive models for interfacial transfer terms is not straightforward and remains under development. To solve the TFM numerically, it is often the

tendency to neglect terms to simplify it based on flow regime of interest. This can make the TFM ill-posed if one of the neglected terms is associated with short wave physics. Ramshaw and Trapp [28] and Lopez de Bertodano et al. [7] demonstrated the significance of short-wave physical mechanisms such as surface tension and viscous diffusion for making the TFM well-posed. Since the 1D Shallow Water TFM is an asymptotic case of the 1D TFM, the ill-posedness caused due to lack of short-wave physics in the 1D TFM is the same as for the 1D Shallow Water TFM. The linear stability analysis helps to address the ill-posedness of the 1D Shallow Water TFM when appropriate short-wave physics is included in the model pertaining to the specific flow regimes.
Using the linear stability theory comprising of the characteristic and the dispersion analysis, the nature of the PDEs in the TFM and the effect of appropriate physical mechanisms on the TFM stability and well-posedness can be addressed. Since the acoustic roots of the TFM are always real (Drew and Passman [27]), the incompressible TFM is used to perform linear stability analysis as the ill-posedness is associated with the material roots which are the void fraction waves for the work presented here.

2.6.1 Characteristic Analysis

Since flow regime transitions can be analyzed using wave theory, the TFM is nevertheless expected to be a wave propagation model. In the characteristic analysis, the eigenvalues of the 1D Shallow Water TFM are solved and they indicate its mathematical behavior. A model is hyperbolic if it has two real and distinct characteristic speeds, which are the Eigenvalues of the systems of PDEs. The presence of imaginary Eigenvalues makes the model elliptic. Another interesting case is when the system of PDEs has only one real Eigenvalue and this renders the model parabolic.

The mathematical nature of the 1D Shallow Water TFM equations can be examined by solving for the Eigenvalues. The system of PDEs are first recast into a quasi-linear form as,

$$\boldsymbol{A}\frac{\partial}{\partial t}\underline{\phi}+\boldsymbol{B}\frac{\partial}{\partial x}\underline{\phi}+\boldsymbol{D}\frac{\partial^2}{\partial x^2}\underline{\phi}+\boldsymbol{F}=0 \tag{49}$$

where, $\underline{\phi}=[\alpha_1 \;\; u_1 \;]^T$. The Eigenvalues are obtained by solving the following constraint equation,

$$\mathrm{Det}(\boldsymbol{A}\,C-\boldsymbol{B})=0 \tag{50}$$

This results in two Eigenvalues,

$$C = [C_1 \;\; C_2]^T \tag{51}$$

which define the propagation speed of the void fraction waves. Following Pauchon and Banerjee [29] the non-dimensional eigenvalues are given by,

$$C_{1,2}^* = \frac{C_{1,2} - u_1}{u_r} \tag{52}$$

The non-dimensional eigenvalues are shown in Fig. 1 to examine the effect of interfacial pressure, virtual mass, collision and wake entrainment. The virtual mass force present in all the cases by default. Pauchon and Banerjee [29] found that that without the interfacial pressure, the 1D Shallow Water TFM is ill-posed as an initial value problem over the entire void fraction range when $u_1 \neq u_2$, which represents the inhomogeneous flow. But when the interfacial pressure is included in the analysis with $c_p = 0.25$, the model becomes well-posed conditionally up to α_2= 0.26 only as seen for the P-B curve (Pauchon and Banerjee [29]). Due to addition of the bubble collision mechanism for $c_{coll} = 1.8$, the 1D Shallow Water TFM ends up being unconditionally hyperbolic for $0 \leq \alpha_2 \leq 1$. Now when the wake entrainment force is included with distinct length scales as stated in Section 2.2, for the stable dispersed bubbly flow case, the model is hyperbolic only for $0 \leq \alpha_2 \leq 0.15$ and $0.36 \leq \alpha_2 \leq 1$. Finally, for the unstable clustered bubbly flow case the model becomes elliptic for $0 \leq \alpha_2 \leq 0.04$ and $0.44 \leq \alpha_2 \leq 1$.

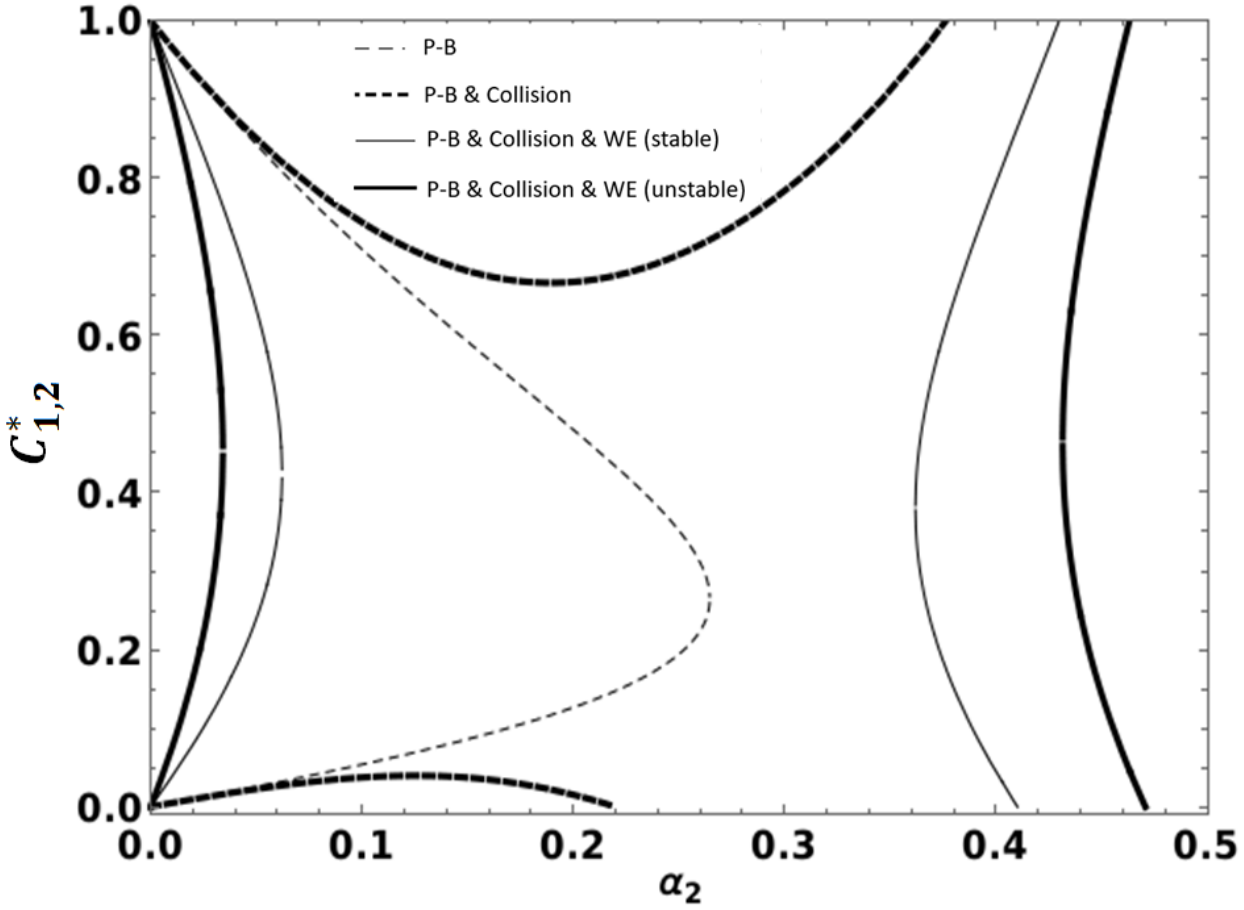

Figure 1 : Eigenvalues of mechanistic 1D Shallow Water TFM

2.6.2 Dispersion Analysis

Unlike the characteristic analysis, the dispersion relation allows the inclusion of the interfacial drag, gravity as well as higher order viscous dissipation and surface tension forces. So, in terms of the flow physics, dispersion analysis gives a more comprehensive picture regarding the stability. In particular, the dispersion analysis helps in addressing the issue of ill-posedness as it helps analyzing the propagation properties of the void fraction waves for all the wavelengths λ in the Fourier space as opposed to the characteristic analysis which is only applicable for $\lambda \to 0$.

In the dispersion analysis, the system of PDEs of the 1D Shallow Water TFM are perturbed and linearized to solve for the dispersion relation, i.e., the relation between the angular frequency $\omega\ (1/s)$ and the wave number $k = 2\pi/\lambda\ \ (1/m)$. The 1D Shallow Water TFM equations are first recast into the form,

$$\boldsymbol{A}\frac{\partial}{\partial t}\delta\underline{\phi} + \boldsymbol{B}\frac{\partial}{\partial x}\delta\underline{\phi} + \boldsymbol{D}\frac{\partial^2}{\partial x^2}\delta\underline{\phi} + \frac{\partial \boldsymbol{F}}{\partial \underline{\phi}}\delta\underline{\phi} = 0 \tag{53}$$

The perturbation of the forma of travelling wave is introduced as,

$$\delta\underline{\phi} = \delta\underline{\phi}_0 e^{i(kx-\omega t)} \tag{54}$$

For a non-trivial solution to exist, the constraint equation reduces to,

$$\det\left[\omega\boldsymbol{A} - k\boldsymbol{B} - ik^2\boldsymbol{D} + \frac{\partial \boldsymbol{F}}{\partial \underline{\phi}}\right]\delta\underline{\phi} = 0 \tag{55}$$

The dispersion relation is obtained by solving the above equation for $\omega(k)$. The real part of ω corresponds to the propagation speed of the void fraction waves defined by ω/k. The presence of an imaginary ω represents an unstable model due to the presence of local instabilities in the void fraction waves. When there is an instability, there are two imaginary components of ω and the larger of the two dominates the growth of void fractions waves leading to development of interfacial structures. In the context of the dispersion analysis, the model is ill-posed when there is infinite growth rate, i.e., very large ω_i as $\lambda \to 0$. Similar to the characteristic analysis, the effect of interfacial pressure, collision and wake entrainment forces on the stability and the well-posedness of the 1D Shallow Water TFM is discussed here. The complete picture of linear stability analysis and fulfillment of the two required attributes of the 1D Shallow Water TFM, namely the well-posedness and unstable becomes clearer by looking at dispersion relation in Fig. 2.

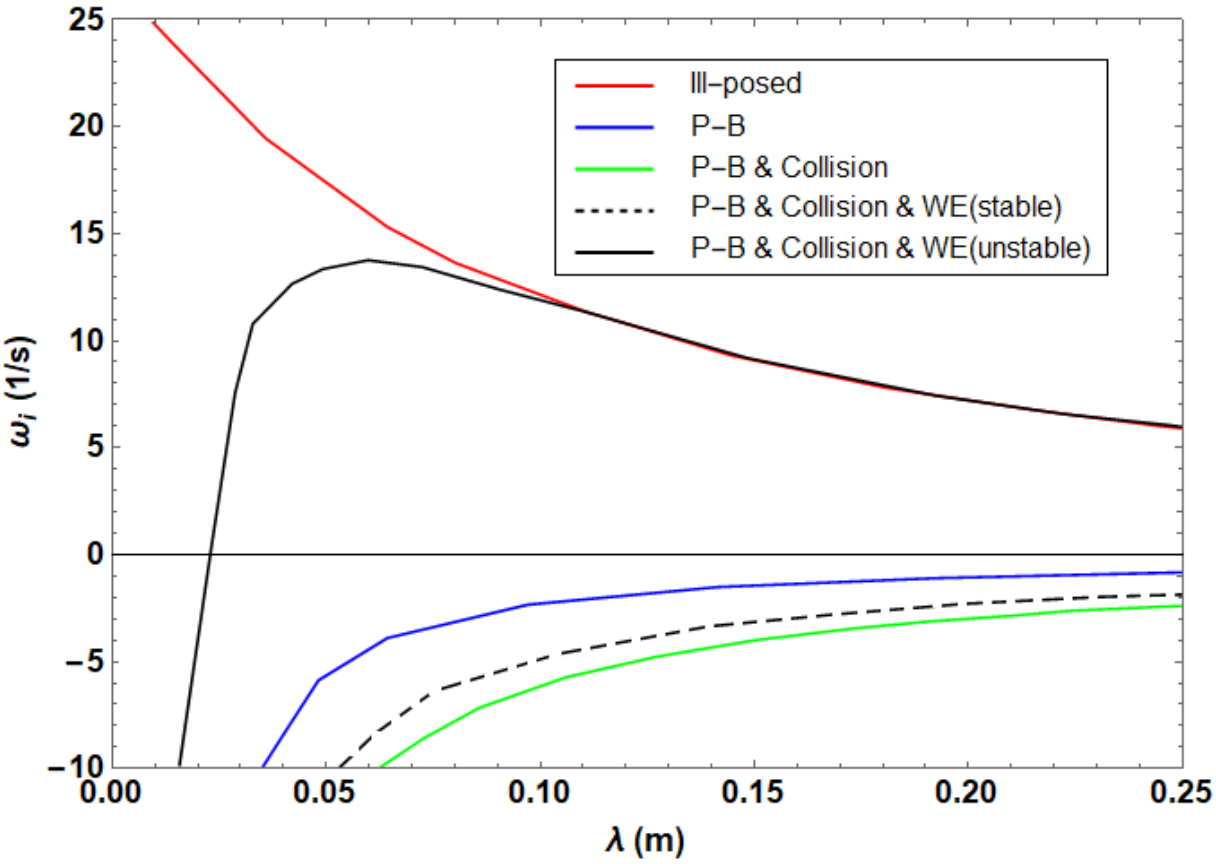

Figure 2: Dispersion relation of mechanistic 1D Shallow Water TFM

The presence of viscosity along with the first order derivative terms make the 1D Shallow Water TFM well-posed as ω_i is finite as $\lambda \to 0$. The absence of real characteristics in Fig. 1 due to presence of local wake entrainment instability is confirmed by positive wave growth rate seen in Fig. 2. It is crucial to note the role played by viscous diffusion mechanisms makes the wave growth rate negative at zero wavelength, which is required for the 1D Shallow Water TFM to be well-posed. To summarize, well-posedness of the model is confirmed by negative wave growth rate at zero wavelengths instead of infinite growth rate and the unstable nature is corroborated by a positive wave growth rate at finite (non-zero) short wavelengths.

2.7 Numercial Simulations

2.7.1 Numerical Method

The 1D Shallow Water TFM equations were solved numerically using in an in-house 1D subchannel code in FORTRAN language. The equations are discretized using a finite difference

method on a staggered grid arrangement as shown in Fig. 3. The 1D spatial domain is divided into finite volumes, with each volume having a cell center c and junctions j and j+1 at its two ends. The void fractions α_k are located at the cell centers and the velocity u_k is located at the junctions.

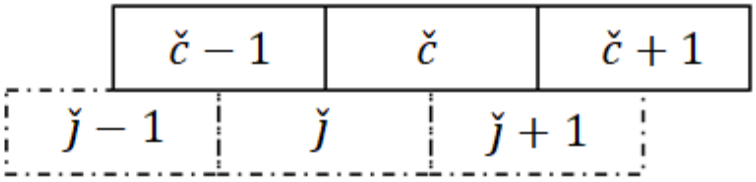

Figure 3: Staggered grid arrangement for 1D domain

The staggered grid arrangement in Fig. 3 is based on a uniform grid with $x_{\check{j}+1} - x_{\check{j}} = x_{\check{c}+1} - x_{\check{c}} = \Delta x$ is constant and a constant time step Δt is used. For a staggered grid, the variables for convection not defined at the required cell centers or junctions are determined by donoring based on the SMART flux limiter scheme of Gaskell and Lau [49] described here briefly. For positive local velocity, the donoring of void fraction at right face with respect to the cell center c is,

$$\hat{\alpha}^n_{k,R} = \alpha^n_{k,\check{c}} + \delta x_{\check{c}} \Psi(\bar{r}) \left(\frac{\partial \alpha_k}{\partial x}\right)_{UD} \tag{56}$$

where the subscript R refers to the right center or junction of the reference location. The upwind derivative is given by,

$$\left(\frac{\partial \alpha_k}{\partial x}\right)_{UD} = \frac{\alpha^n_{k,\check{c}} - \alpha^n_{k,\check{c}-1}}{\Delta x} \tag{57}$$

and the variable $\bar{r}$ is,

$$\bar{r} = \frac{\alpha^n_{k,\check{c}+1} - \alpha^n_{k,\check{c}}}{\alpha^n_{k,\check{c}} - \alpha^n_{k,\check{c}-1}} \tag{58}$$

Likewise, for negative velocity, donoring of void fraction is from the cell center $\check{c}+1$ and the upwind derivative and r are defined by $\alpha^n_{k,\check{c}+2} - \alpha^n_{k,\check{c}+1}$. In Eq. (56), $\Psi(\bar{r})$ is the flux limiter function based on general-piecewise limiter scheme of Waterson and Deconick [50] defined as,

$$\Psi(\bar{r}) = \max\left[0, min\left\{(2+a)\bar{r}, \frac{(1+\grave{k})\bar{r}}{2} + \frac{(1-\grave{k})\bar{r}}{2}, \breve{M}\right\}\right] \tag{59}$$

In the general piecewise limiter function, the SMART flux limiter scheme is defined for $a = 0, \grave{k} = 1/2$ and $\breve{M} = 4$. The SMART scheme was chosen due to its capability to resolve shock like structures compared to the other flux limiter schemes. The donoring of velocity follows similar procedure given by Eqs. (56)-(59) with the spatial location shifted by $\Delta x/2$. For time advancement of the state variables $\underline{\phi} = [\alpha_1 \;\; u_1]^T$, the three stage third order Runge-Katta scheme of Gottlieb and Shu [51] is used as,

$$\begin{aligned} \frac{\partial \underline{\phi}}{\partial t} &= \breve{F}\left(\underline{\phi}\right) \\ \underline{\phi}^{(1)} &= \underline{\phi}^{n} + \Delta t\, \breve{F}\left(\underline{\phi}^{n}\right) \\ \underline{\phi}^{(2)} &= \frac{1}{4}\underline{\phi}^{(1)} + \frac{3}{4}\underline{\phi}^{n} + \frac{1}{4}\Delta t\, \breve{F}\left(\underline{\phi}^{(1)}\right) \\ \underline{\phi}^{(n+1)} &= \frac{2}{3}\underline{\phi}^{(2)} + \frac{1}{3}\underline{\phi}^{n} + \frac{2}{3}\Delta t\, \breve{F}\left(\underline{\phi}^{(2)}\right) \end{aligned} \tag{60}$$

It was demonstrated by Lopez de Bertodano et al. [7] that the overall order of accuracy of the SWT TFM code being used is higher than second order but less than third order accuracy.

2.7.2 Validation

The 1D Shallow Water TFM simulations with the wake entrainment instability are validated against the experimental results of Cheng and Azzopardi [2] and Song et al. [3] to capture transition from dispersed to clustered bubbly flow. Cheng and Azzopardi [2] performed air-water two-phase flow experiments in a 4 m long vertical annular pipe, having a diameter of 28.9 mm, for flow pattern transition from bubbly to slug flow. For a constant liquid velocity of 0.356 m/s, bubbly two-phase phase mixture was injected into the pipe by varying the gas flow rate. The liquid and gas flow rates were measured using flowmeters and the void fraction waves were measuring using impedance void fraction meters. It was found that the critical void fraction for bubbly to slug flow transition decreased with increase in the initial bubble size. Song et al. [3] performed similar air-water two-phase bubbly flow experiments using a 25 mm diameter pipe having a height of 3 m for different bubble sizes over a wide range of flow conditions. The void fraction signals were measured using impedance void fraction meters to statistically analyze the void fraction wave propagation properties, such as spatial growth rates, wavelengths and wave speeds. It was found that spatial amplification rates were sensitive to the bubble size for a given liquid flux. The smaller

bubbles of 2.7 mm mean diameter did not form clusters, but larger bubbles of 4.78 mm mean diameter formed clusters. In both experiments, the transition from bubbly to slug flow, which involves the formation of bubble clusters depending on the bubble size and net volumetric flux, was analyzed due to instabilities in the void fraction waves.

Table 1 : Experimental conditions for dispersed and clustered bubbly flow

Experiment	D_b(mm)	Dispersed Bubbly Flow			Clustered Bubbly Flow		
		α_2	j_2(m/s)	j_1(m/s)	α_2	j_2(m/s)	j_1(m/s)
Cheng and Azzopardi [2]	3.62	0.13	0.1315	0.356	0.20	0.138	0.356
Song et al. [3]	4.8	0.05	0.021	0.18	0.139	0.084	0.18

Table 1 summarizes the experimental conditions used for validation of non-linear numerical simulation results of the 1D Shallow Water TFM. The temporal evolution of void fraction waves from the numerical simulations are compared with that of the experimental cases given in Table 1. For the non-linear simulation results presented here, a mesh size $\Delta x = 5$ mm for the 1D spatial domain of length 1 m and the time step Δt, defined based on $\Delta t = 0.001$ s were used. Fig. 4 and Fig. 5 show the stable bubbly and unstable clustered bubbly flow simulations of Cheng and Azzopardi [2] for the mean bubble diameter of 3.62 mm respectively. It can be seen for lower void fractions, which correspond to the stable bubbly flow, the void fraction waves do not grow from their initial condition and we have a uniform void fraction distribution. This is due to the fact that the wake entrainment force is not strong enough as the bubbles are dispersed or spread out such that the interaction between the bubbles is negligible in terms of wake entrainment. But when the void fraction is increased, which corresponds to the case of the clustered bubbly flow case, the perturbations in the initial condition grow and distinct interfacial structures unique to bubble clusters are formed. At higher void fractions, the wake entrainment is strong and a trailing bubble experiences lesser drag due to the wake of the leading bubble. But the amplitude of interfacial structures for bubble clusters obtained from the numerical calculations are significantly lower than the experimental observations. While at present, the onset of instability and wave characteristics including wavelengths and wave propagation speeds have been characterized with the proposed model, the reason for significant deviation in the amplitude predictions remains to be understood.

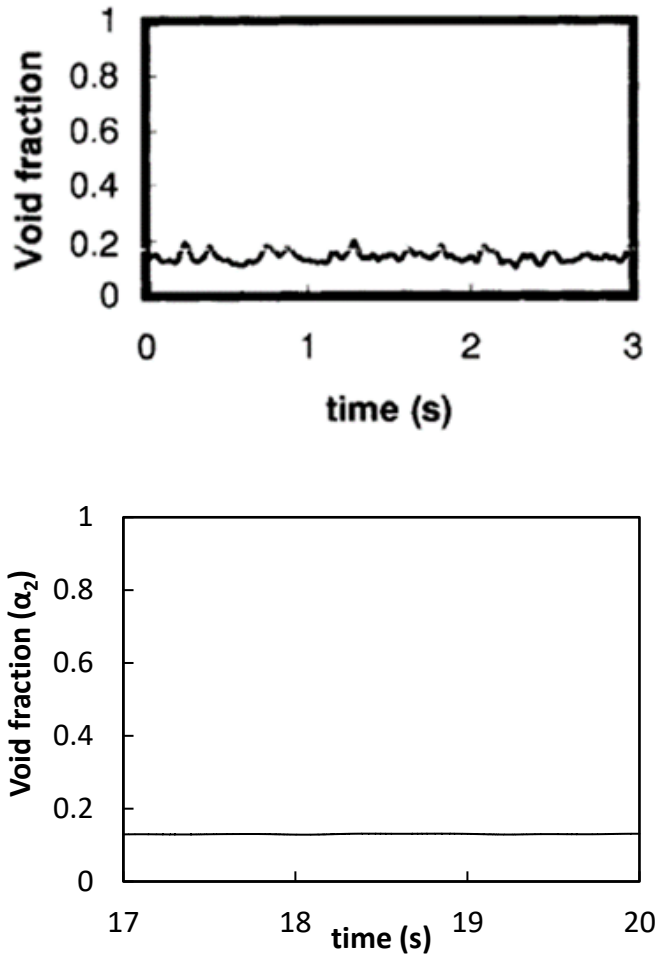

Figure 4: Comparison of data and simulation for bubbly flow at 13% void fraction

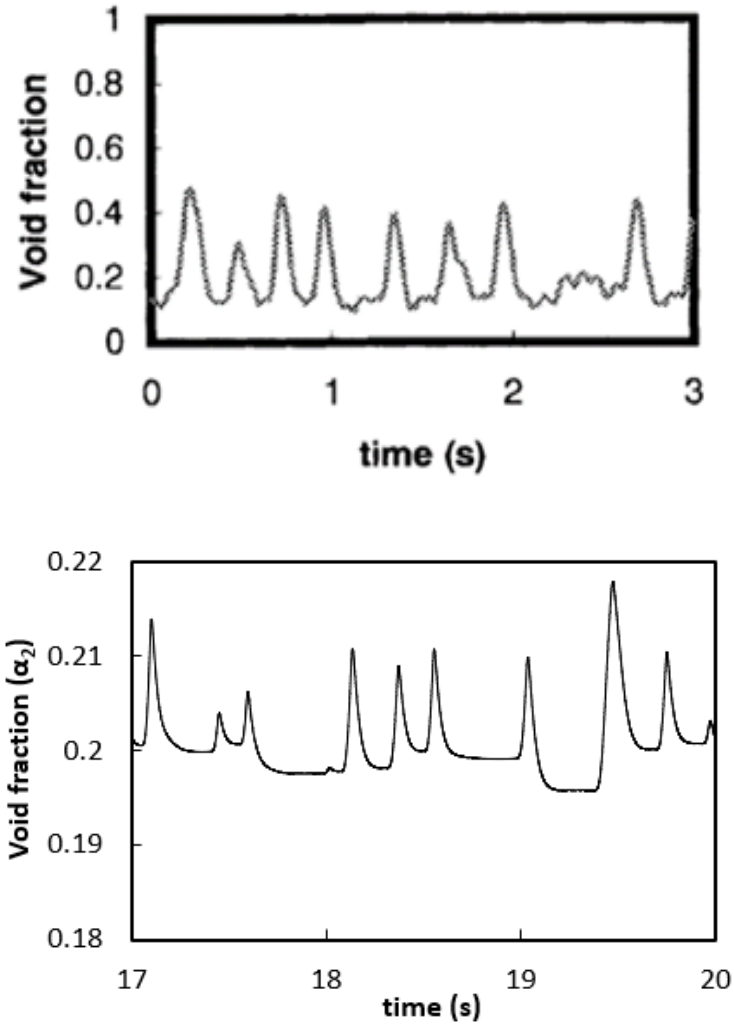

Figure 5: Comparison of data and simulation for clustered bubbly flow at 20% void fraction

Fig. 6 and Fig. 7 show the simulation results for the dispersed and clustered bubbly flow of Song et al. [3], where the simulation data had been collected at distance of 2.5 m from the inlet. Song et. al. [3] provide time series data for the voltage signal from impedance void meters. An empirical correlation defines the void fraction α_2 in terms of the voltage as,

$$\frac{V}{V_0} = 0.996 - 1.674\ \alpha_2 + 0.134\alpha_2^2 \tag{61}$$

where V_0 is the voltage signal for $\alpha_2 = 0$, not given explicitly by the authors. When the mean void fraction is 0.05, the instability does not occur as observed previously for the low void fraction case

of Cheng and Azzopardi [2]. When a mean void fraction of 0.10 is used to prescribe the initial conditions, wave growth can be seen.

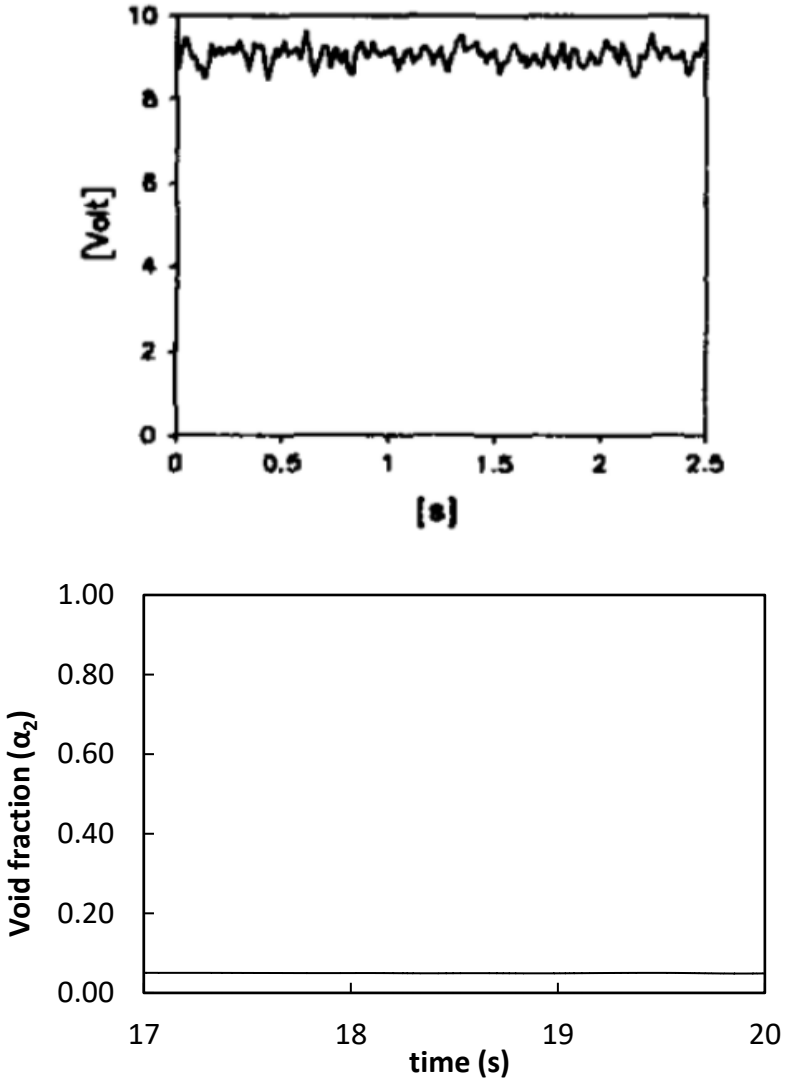

Figure 6: Comparison of data and simulation for discrete bubbly flow of Song et al. [3]

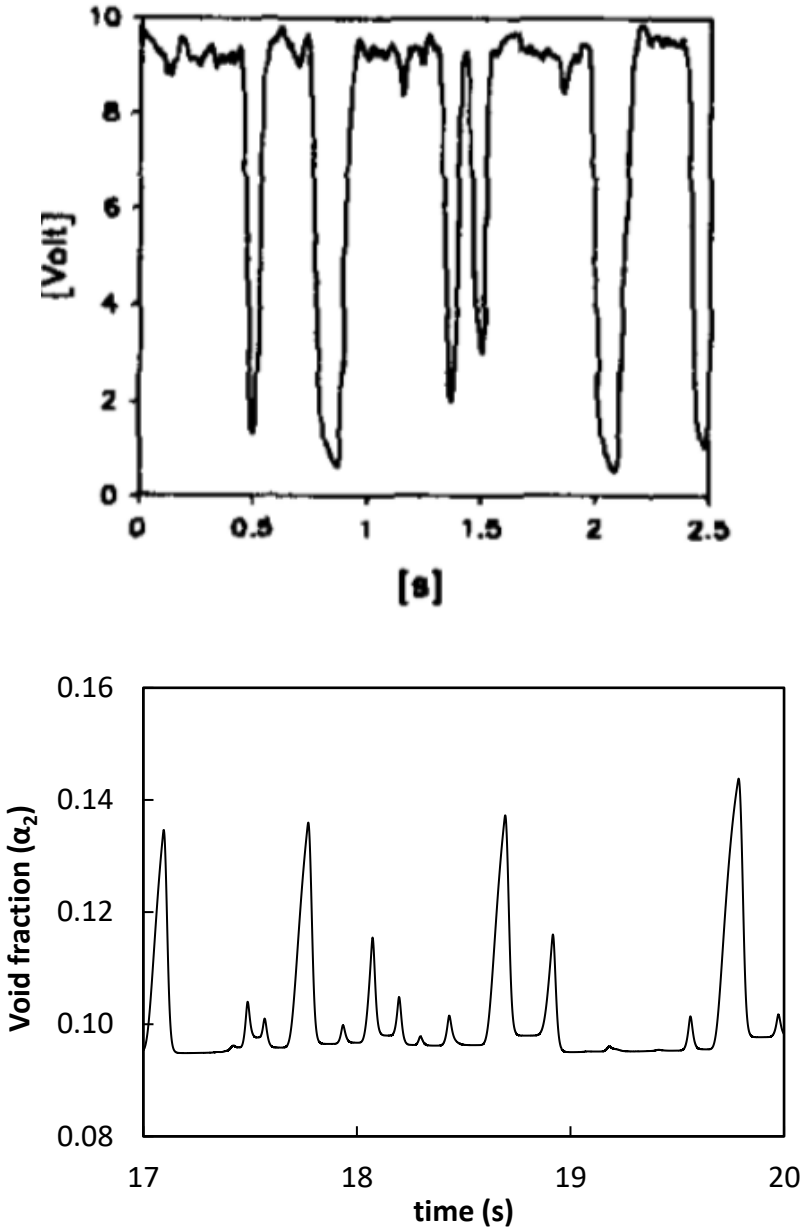

Figure 7: Comparison of data and simulation for clustered bubbly flow of Song et al. [3]

Table 2 summarizes the wave speeds C_w, wavelengths λ_w and relative velocities of the bubble cluster waves obtained from the experimental data and simulations. Though wavelengths and wave speeds are in reasonable agreement with the experiments, the amplitudes of bubble cluster waves obtained from the numerical calculations are under-predicted. Hence, it can be concluded that it is possible to model the instability resulting in the clustered bubbly flows using the 1D Shallow Water TFM when the wake entrainment mechanism is considered. It is important to note that the

wake entrainment effect is present only in the axial direction in the present model. Other physical clustering mechanisms present along the transverse and longitudinal directions, which require additional modelling efforts and are out of the scope of the present work.

Table 2: Comparison of wavelengths and wave speeds

Experiment	λ_w^{exp}	λ_w^{sim}	C_w^{exp}	C_w^{sim}	u_r^{exp}	u_r^{sim}
Cheng and Azzopardi [2]	30 cm	27 cm	80 cm/s	71 cm/s	28 cm/s	27 cm/s
Song et al. [3]	33 cm	25 cm	45 cm/s	40 cm/s	34 cm/s	32 cm/s

3. VARIATIONAL TWO-FLUID MODEL

Historically, two-phase flow formulations using the Eulerian description have been approached in using two different ways. The most well-known approach is the mechanistic approach based on Newtonian physics. The mechanistic approach starts with two separate local instantaneous equations for conservation of mass, momentum and energy for the two phases at the microscopic level. The microscopic equations are then linked together using interfacial jump conditions. But for engineering design applications, such a detailed microscopic description of the flow physics is not very useful. So the local instantaneous equations are averaged using different averaging techniques. In order to complete the macroscopic formulation based on averaging, the constitutive relations for the interfacial force terms need to be defined in terms of the macroscopic state variables. And this is where significant challenges have been encountered in the past. For each and every different physical mechanism, a force term is added into the momentum equation. Even though objectivity (material frame invariance) has been used as one of the criteria for obtaining constitutive relations, a general consensus is yet to be attained for the interfacial momentum transfer terms. It is important to note that use of mathematically and physically incoherent constitutive terms will not only induce unphysical/artificial instabilities within the flow, but will also violate the objectivity constraint.

To address the stability and objectivity issues posed by the mechanistic formulation for two-phase mixtures, a second approach based on Hamilton's variational principle in Eulerian coordinates by Seliger and Whitham [52] offers an alternative. The variational principle has been used in the past for deriving the single-phase Euler equations by Bedford and Drumheller [53] and Clausse [54] and was extended for immiscible adiabatic two-phase mixtures. The application of variational principles for two-phase mixtures was motivated by its use for the two-phase behavior of superfluid ^{4}He by Zilsel [55] and it was presented comprehensively for adiabatic two-phase dispersed flows by Geurst [21] for the first time. The variational approach starts with the definition of the Lagrangian density defined in terms of the average state variables (macroscopic) and hence averaging is done at the beginning of the formulation approach. Whereas, averaging is performed at the end in the mechanistic approach. This is followed by application of the extended Hamilton's principle of least action to the Lagrangian density, which yields the non-dissipative momentum

equations for the two phases, proved to be objective by Geurst [21]. At least for objectivity, the variational approach is superior, but the physical meaning of the momentum transfer terms is not always clear. Moreover, Wallis [22] suggested that adding each force term separately, as in the mechanistic approach, can lead to double counting the effects of the same physical mechanism. It is reasonable to state that both the mechanistic and variational approaches should be considered as complimentary to each other.

3.1 1D Two-Fluid Model

The procedure presented here to derive the 1D variational TFM follows Geurst [4] and Pauchon and Smereka [20]. For an adiabatic two-phase mixture, the phasic void fraction α_k ($k = 1$ for continuous liquid phase and $k = 2$ for dispersed gas phase) with $\alpha_1 + \alpha_2 = 1$ and the volume averaged velocity u_k are the state variables. The volume averaged Lagrangian density $\widetilde{L}$ is the difference between the kinetic energy K and the potential energy P density as,

$$\widetilde{L} = K - P \tag{62}$$

The volume averaged kinetic energy density K consists of contributions from individual phases and an additional part due to coupling/interaction between the two phases which accounts for the virtual mass effect.

$$K = \frac{1}{2}\,\rho_1\,\alpha_1\,u_1^2 + \frac{1}{2}\,\rho_2\,\alpha_2\,u_2^2 + \frac{1}{2}\,\rho_1\,m(\alpha_2)\,(u_2 - u_1)^2 \tag{63}$$

In the above definition for K, ρ_k is the phasic density, $m(\alpha_2)$ is the inertial coupling/virtual mass coefficient (discussed later) and $u_r = u_2 - u_1$ is the relative velocity. The additional kinetic energy due to phasic interactions represents the energy due to motion of liquid with respect to its mass center and it is neglected for the gas phase (Geurst [4]). For isothermal, adiabatic and incompressible flow, the potential energy density $P = 0$. Since mass conservation principle and $\alpha_1 + \alpha_2 = 1$ have not been considered in the Lagrangian density, the Lagrangian is modified as,

$$\hat{L} = \widetilde{L} + \zeta_1\left(\frac{\partial \rho_1\alpha_1}{\partial t} + \frac{\partial \rho_1\alpha_1 u_1}{\partial x}\right) + \zeta_2\left(\frac{\partial \rho_2\alpha_2}{\partial t} + \frac{\partial \rho_2\alpha_2 u_2}{\partial x}\right) + \zeta_3\,(\alpha_1 + \alpha_2\,) \tag{64}$$

where ζ_1, ζ_2 and ζ_3 are the Lagrange multipliers. The introduction of constraints through Lagrange multipliers is a common practice followed for finding the optimum value of a functional, which is the Lagrangian here.

The extended Hamilton's principle for classical fluid mechanics states that the equations of fluid motion are equivalent to minimization of the action,

$$\hat{A} = \delta \int dt \int dx \, \hat{L} = 0 \tag{65}$$

The above statement is also known as the least action principle and it states that of all the trajectories a system can follow, the system will follow the one that will minimize $\hat{A}$. Using integration by parts,

$$\hat{A} = \delta \int dt \int dx \, \hat{L} = 0 \tag{66}$$

where

$$\hat{L} = \widetilde{L} - \rho_1 \alpha_1 \left(\frac{\partial \zeta_1}{\partial t} + u_1 \frac{\partial \zeta_1}{\partial x} \right) - \rho_2 \alpha_2 \left(\frac{\partial \zeta_2}{\partial t} + u_2 \frac{\partial \zeta_2}{\partial x} \right) + \zeta_3 \, (\alpha_1 + \alpha_2) \tag{67}$$

Taking variations with respect to the state variables gives following Euler-Lagrange equations,

$$\delta\alpha_1 : \ \frac{1}{2} \rho_1 u_1^2 - \rho_1 \left(\frac{\partial \zeta_1}{\partial t} + u_1 \frac{\partial \zeta_1}{\partial x} \right) + \zeta_3 = 0 \tag{68}$$

$$\delta\alpha_2 : \ \frac{1}{2} \rho_2 u_2^2 + \frac{1}{2} \rho_1 m'(\alpha_2) u_r^2 - \rho_2 \left(\frac{\partial \zeta_2}{\partial t} + u_2 \frac{\partial \zeta_2}{\partial x} \right) + \zeta_3 = 0 \tag{69}$$

$$\delta u_1 : \ \rho_1 \alpha_1 u_1 - \rho_1 m(\alpha_2) (u_2 - u_1) - \rho_1 \alpha_1 \frac{\partial \zeta_1}{\partial x} = 0 \tag{70}$$

$$\delta u_2 : \ \rho_2 \alpha_2 u_2 + \rho_2 m(\alpha_2) (u_2 - u_1) - \rho_2 \alpha_2 \frac{\partial \zeta_2}{\partial x} = 0 \tag{71}$$

The following momentum equations are obtained by eliminating the Lagrange multipliers,

$$\begin{aligned} \left(\frac{\partial}{\partial t} + u_1 \frac{\partial}{\partial x} \right) \left(u_1 - \frac{m(\alpha_2)}{\alpha_1} (u_2 - u_1) \right) - \frac{m(\alpha_2)}{\alpha_1} (u_2 - u_1) \frac{\partial u_1}{\partial x} \\ + \frac{\partial}{\partial x} \left(\frac{\zeta_2}{\rho_1} + \frac{1}{2} m'(\alpha_2) (u_2 - u_1)^2 \right) = 0 \end{aligned} \tag{72}$$

$$\left(\frac{\partial}{\partial t}+u_2\frac{\partial}{\partial x}\right)\left(u_2-\frac{\rho_1 m(\alpha_2)}{\rho_2\alpha_1}(u_2-u_1)\right)+\frac{\rho_1 m(\alpha_2)}{\rho_2}(u_2-u_1)\frac{\partial u_2}{\partial x}+\frac{\partial \zeta_2}{\partial x}=0 \qquad (73)$$

where $\zeta_2 = p_2$. It can be seen that the variational approach for derivation of the TFM gives equations of motion similar to averaging technique and the relevant physical forces are present in the momentum equation along with their constitutive relations. It is important to note that the variational approach presented here leads to equations of motion corresponding to the conservative/non-dissipative mechanisms and hence non-conservative/dissipative forces like interfacial drag and viscous stresses need to be added as ad-hoc for completion.

3.1.1 Comparison of Variational and Mechanistic TFM

This section focuses first and foremost on the fundamental 1D TFM equations derived from the variational approach in the previous section. Then a comparison is made with the mechanistic 1D TFM equations. The TFM used by Pauchon and Banerjee [29] for stable and dispersed bubbly flows is chosen as the reference model to study the variational TFM. The extra terms present in the variational 1D TFM when compared with the mechanistic 1D TFM are stated clearly in this section and the implications of these terms at present are still under study and are yet to be understood. From the previous section, the 1D momentum equations for the continuous liquid phase and the dispersed gas phase can be written as,

$$\begin{aligned}\rho_1\left(\frac{\partial u_1}{\partial t}+u_1\frac{\partial u_1}{\partial x}\right) = &-\frac{\partial}{\partial x}\left(p_2+\left(\frac{m(\alpha_2)+\alpha_1 m(\alpha_2)'}{2\alpha_1}\right)\rho_1 {u_r}^2\right)\\ &-\left(\frac{m(\alpha_2)+\alpha_1 m(\alpha_2)'}{2{\alpha_1}^2}\right){u_r}^2\frac{\partial \alpha_1}{\partial x}\\ &-\rho_1\left(\frac{m(\alpha_2)}{\alpha_1}\right)\left(\frac{\partial u_1}{\partial t}+u_1\frac{\partial u_1}{\partial x}-\frac{\partial u_2}{\partial t}-u_2\frac{\partial u_2}{\partial x}\right)\\ &+(\rho_1 u_r)\left(\frac{\partial}{\partial t}\left(\frac{m(\alpha_2)}{\alpha_1}\right)+u_1\frac{\partial}{\partial x}\left(\frac{m(\alpha_2)}{\alpha_1}\right)\right)\end{aligned} \qquad (74)$$

$$\rho_2\left(\frac{\partial u_2}{\partial t}+u_2\frac{\partial u_2}{\partial x}\right) = -\frac{\partial P_2}{\partial x} \qquad (75)$$

$$-\rho_1\left(\frac{m(\alpha_2)}{\alpha_2}\right)\left(\frac{\partial u_1}{\partial t}+\ u_1\frac{\partial u_1}{\partial x}-\frac{\partial u_2}{\partial t}-\ u_2\frac{\partial u_2}{\partial x}\right)$$

$$-\rho_1 u_r\left(\frac{\partial}{\partial t}\left(\frac{m(\alpha_2)}{\alpha_2}\right)-\left(\frac{m(\alpha_2)}{\alpha_2}\right)\frac{\partial u_r}{\partial x}\right)$$

The momentum equations of the mechanistic 1D TFM with just the conservative forces are,

$$\rho_1\left(\frac{\partial u_1}{\partial t}+\ u_1\frac{\partial u_1}{\partial x}\right)=\ -\frac{\partial p_1}{\partial x}-\frac{(p_{1i}-p_1)}{\alpha_1}\frac{\partial \alpha_1}{\partial x}-\frac{M_{2i}^{VM}}{\alpha_1} \tag{76}$$

$$\rho_2\left(\frac{\partial u_2}{\partial t}+\ u_2\frac{\partial u_2}{\partial x}\right)=\ -\frac{\partial p_2}{\partial x}+\frac{M_{2i}^{VM}}{\alpha_2} \tag{77}$$

When Eqs. (74)-(75) are compared with Eqs. (76)-(77), the virtual mass term in the momentum equation can be written alternatively as,

$$\begin{aligned} M_{2i}^{VM} &= \alpha_2\rho_1 c_{vm}\left[\left(\frac{\partial u_1}{\partial t}+u_1\frac{\partial u_1}{\partial x}\right)-\left(\frac{\partial u_2}{\partial t}+u_2\frac{\partial u_2}{\partial x}\right)\right] \\ &= \rho_1 m(\alpha_2)\left[\left(\frac{\partial u_1}{\partial t}+u_1\frac{\partial u_1}{\partial x}\right)-\left(\frac{\partial u_2}{\partial t}+u_2\frac{\partial u_2}{\partial x}\right)\right] \end{aligned} \tag{78}$$

The virtual mass term in Eq. (78) is the same as the one proposed by Drew and Lahey [27] and relation between c_{vm} and $m(\alpha_2)$ was given by Wallis [19] as ,

$$c_{vm}=\frac{m(\alpha_2)}{\alpha_2} \tag{79}$$

Regarding the interfacial pressure force, Stuhmiller [36] proposed the following expression,

$$p_{1i}-p_1=-C_p\rho_1(u_1-u_2)^2 \tag{80}$$

where c_p is the interfacial pressure coefficient and its relation with the inertial coupling coefficient $m(\alpha_2)$ according to Wallis [19] is.

$$c_p=\frac{m(\alpha_2)+\alpha_1 m'(\alpha_2)}{2\alpha_1} \tag{81}$$

An important inference from the comparison of variational 1D TFM and the mechanistic 1D TFM is that mechanistic model is present within the variational model. In addition, comparison of Eq.

(74)-(75) and Eqs. (76)-(77) gives few terms that are missing in the R.H.S of the mechanistic 1D TFM equations as shown below,

$$\bar{M}_{1i}^{Var} = u_r \rho_1 \left(\frac{\partial}{\partial t}\left(\frac{m(\alpha_2)}{\alpha_1}\right) + u_1 \frac{\partial}{\partial x}\left(\frac{m(\alpha_2)}{\alpha_1}\right)\right)$$
$$\bar{M}_{2i}^{Var} = -\rho_1 u_r \left(\frac{\partial c_{vm}}{\partial t} + c_{vm}\frac{\partial u_r}{\partial x}\right) \quad (82)$$

where $\bar{M}_{1i}^{Var}$ and $\bar{M}_{2i}^{Var}$ are the missing terms in the mechanistic 1D TFM momentum equations of the liquid phase and the gas phase respectively. By analyzing the mathematical form of the missing terms, Wallis [19] calls the missing terms in the liquid momentum equation, $\bar{M}_{1i}^{Var}$, a transport term for the inertial coupling coefficient, $m(\alpha_2)$. Further simplification of $\bar{M}_{1i}^{Var}$ gives,

$$\bar{M}_{1i}^{Var} = \left(-2\rho_1 u_r \frac{c_p}{\alpha_1}\right)\left(\frac{\partial \alpha_1}{\partial t} + u_1 \frac{\partial \alpha_1}{\partial x}\right) \quad (83)$$

Meanwhile, the missing term in the gas momentum equation, $\bar{M}_{2i}^{Var}$, has a more complicated form and is yet to have a convincing interpretation. Nevertheless, since both the terms relate to the inertial coupling coefficient, they are assumed to be good models for phase-configuration mechanisms. At present, the importance of these missing terms is yet to be understood.

3.2 1D Shallow Water Two-Fluid Model

Similar to the previous section, the use of variational approach to derive the two-equation 1D Shallow Water TFM equations is presented here. It is shown that the mechanistic and the variational Shallow Water TFM equations are equivalent, except for few additional momentum transfer terms present in the variational equations, as was the case even with the full 4-equation TFM. Pauchon and Smereka [20] were the first to demonstrate the use of variational method for deriving the 1D fixed flux TFM using the fixed-flux assumption, i.e., $j_0 = constant$. In order to derive the Shallow Water TFM equations, a frame of reference moving with $j_0 = constant$ is used. This transforms the phasic velocities in the moving frame as,

$$u_2{}^* = u_2 - j = u_2 - (\alpha_1 u_1 + \alpha_2 u_2) = (1-\alpha_2)u_r$$
$$u_1{}^* = u_1 - j = -\alpha_2 u_r \quad (84)$$

A remarkable result of writing the phasic velocities in the moving frame in terms of the relative velocity $u_r = u_2 - u_1 = u_2^* - u_1^*$ is that the two continuity equations are the same,

$$\frac{\partial \alpha_2}{\partial t} + \frac{\partial J}{\partial x^*} = 0 \tag{85}$$

where $x^* = x - j_0\, t$ and the superscript * will be dropped from here for convenience. The drift flux J is defined as,

$$J = \alpha_2(1-\alpha_2)u_r = \alpha_2 V_{gj} \tag{86}$$

and V_{gj} is the drift velocity. Now the volume average Lagrangian density of the two-phase mixture, which is the difference between the kinetic energy K and potential energy P density is,

$$\widetilde{L} = K - P \tag{87}$$

where the kinetic energy density for the dispersed two-phase mixture can be written as,

$$K = \frac{1}{2}\, \Gamma J^{\,2} \tag{88}$$

The net effective inertia Γ is defined as,

$$\Gamma = \frac{\rho_1}{(1-\alpha_2)} + \frac{\rho_2}{\alpha_2} + \frac{\rho_1\, m(\alpha_2)}{{\alpha_2}^2(1-\alpha_2)^2} \tag{89}$$

In the definition of Γ, $m(\alpha_2)$ is the inertial coupling coefficient. Use of Γ enables representation of the two-phase mixture collectively as a pseudo fluid with added mass included in it. The potential energy density consists of contributions from the elastic energy of the interface as well as the gravitational energy,

$$P = E + G \tag{90}$$

The interfacial elastic energy is derived using a geometrical representation of interface for the two-phase mixture in an averaged sense as shown in Fig. 8. The differential interfacial area ∂A_i is,

$$\partial A_i = \partial z \sqrt{\partial x^2 + {D_{pipe}}^2 (\partial \alpha_2)^2} \tag{91}$$

This will give the interfacial area per unit projected area as,

$$\bar{A_i} = \frac{\partial A_i}{\partial z\, \partial x} = \sqrt{1 + {D_{pipe}}^2 \left(\frac{\partial \alpha_2}{\partial x}\right)^2} \tag{92}$$

Then the elastic energy of the interface per unit volume is,

$$E = \frac{\sigma \bar{A}_\iota}{D_{pipe}} \tag{93}$$

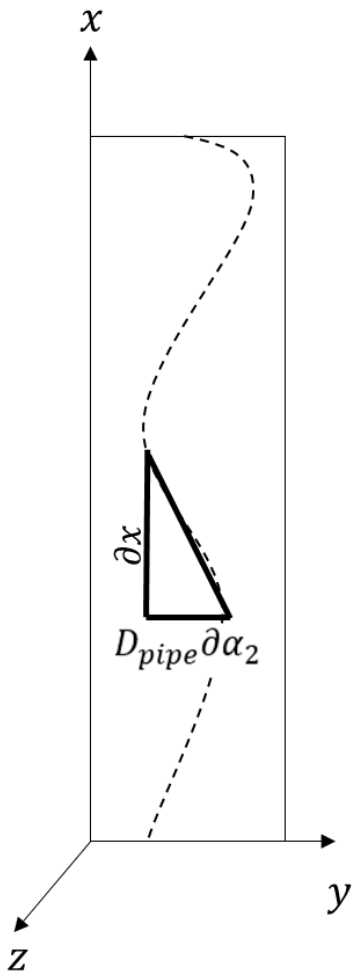

Figure 8: Interfacial geometry for elastic potential energy calculation

where D_{pipe} the pipe diameter is used as the length scale and σ is the surface tension coefficient. Hence the elastic energy of the interface per unit volume will be,

$$E = \frac{\sigma \bar{A}_\iota}{D_{pipe}} = \frac{\sigma}{D_{pipe}} \sqrt{1 + {D_{pipe}}^2 \left(\frac{\partial \alpha_2}{\partial x}\right)^2} \tag{94}$$

The gravitational potential energy per unit volume for the two-phase mixture can be written as,

$$G = gx(\rho_1 - \rho_2)(1 - \alpha_2) \tag{95}$$

If the fields (state variables) α_2 and J are defined using the potential $\chi(x,t)$ as,

$$\alpha_2 = \frac{\partial \chi}{\partial x} = \chi_x$$
$$J = \frac{-\partial \chi}{\partial t} = -\chi_t \tag{96}$$

then Lagrangian density can be rewritten as,

$$\widetilde{L}\left(\chi_t, \chi_x, \chi_{xx}\right) = \frac{\Gamma(\chi_x)}{2}\chi_t^2 - E(\chi_{xx}) - \mathrm{G}(\chi_x) \tag{97}$$

From the least action principle for fields, the Euler-Lagrange equation is,

$$\frac{\partial}{\partial t}\left(\frac{\partial \widetilde{L}}{\partial \chi_t}\right)\frac{\partial}{\partial x}\left(\frac{\partial \widetilde{L}}{\partial \chi_x}\right) - \frac{\partial^2}{\partial x^2}\left(\frac{\partial \widetilde{L}}{\partial \chi_{xx}}\right) = 0 \tag{98}$$

which gives the following momentum conservation equation,

$$\frac{\partial \Gamma J}{\partial t} + \frac{\partial}{\partial x}\left(-\frac{1}{2}\Gamma' J^2 + \sigma\, \mathrm{K}\right) + (\rho_1 - \rho_2)|g| = 0 \tag{99}$$

where the interfacial curvature K assuming ${D_{pipe}}^2\ {\alpha_2}_x{}^2 \ll 1$ is,

$$\mathrm{K} = \frac{D_{pipe}\ \alpha_{2_{xx}}}{\left(1 + {D_{pipe}}^2\ {\alpha_2}_x{}^2\right)^{\frac{3}{2}}} \cong D_{pipe}\frac{\partial^2 \alpha_2}{\partial x^2} \tag{100}$$

To complete the model, the dissipative interfacial drag force term is added ad-hoc to Eq. (99) to get the complete two-equation 1D variational Shallow Water TFM as,

$$\frac{\partial \alpha_2}{\partial t} + \frac{\partial J}{\partial x} = 0 \tag{101}$$

$$\frac{\partial \Gamma J}{\partial t} - \frac{\partial}{\partial x}\left(\frac{1}{2}\Gamma' J^2\right) + \sigma D_{pipe}\frac{\partial^3 \alpha_2}{\partial x^3} = -\rho_1\left(\frac{c_D}{D_{pipe}}\ \frac{J}{\alpha_2(1-\alpha_2)}\left|\frac{J}{\alpha_2(1-\alpha_2)}\right| + \left(1 - \frac{\rho_2}{\rho_1}\right)|g|\right) \tag{102}$$

The first equation is the mass conservation equation and the second equation is the momentum conservation equation in a frame of reference moving at j_0. The relative velocity u_r has been written in terms of the state variable J as $u_r = J/\alpha_2(1-\alpha_2)$, c_D is the interfacial drag coefficient and D_{pipe} is the pipe diameter. For the closure of the conservative momentum transfer terms, formulation of the inertial coupling coefficient $m(\alpha_2)$ is required.

3.2.1 Comparison of Variational and Mechanistic Shallow Water TFM

Interestingly enough, the variational Shallow Water TFM equations can be written in terms of the primitive variables α_1 and u_1 .The non-dimensional inertia Γ^* for $r_p \ll 1$ follows,

$$\Gamma^* = \frac{1}{(1-\alpha_2)} + \frac{m(\alpha_2)}{{\alpha_2}^2(1-\alpha_2)^2} \tag{103}$$

Following Wallis [19], $c_{vm} = m(\alpha_2)/\ \alpha_2$ and using $J = \ -(1-\alpha_2)u_1$, Eqs. (101)-(102) without the surface tension force terms in terms of α_1 and u_1 are,

$$\frac{\partial\ \alpha_1}{\partial t} + u_1\frac{\partial \alpha_1}{\partial x} + \alpha_1\frac{\partial u_1}{\partial x} = 0 \tag{104}$$

$$\frac{\partial u_1}{\partial t} + {B_{21}}^{var}\frac{\partial \alpha_1}{\partial x} + {B_{22}}^{var}\frac{\partial u_1}{\partial x} = \frac{\alpha_1\alpha_2}{c_{vm}+\alpha_1\alpha_2}\left[-|g| + \frac{M_{2i}^D}{\rho_1\alpha_1\alpha_2}\right] \tag{105}$$

where,

$${B_{21}}^{var} = {\alpha_2}^2\alpha_1\left[2\Gamma^{*\prime} - \alpha_1\Gamma^{*\prime\prime} - \left(\frac{m(\alpha_2)}{{\alpha_2}^2\alpha_1}\right)'\right]{u_r}^2 \tag{106}$$

$${B_{22}}^{var} = -\alpha_2\left[(1-\alpha_2)\left(\frac{m(\alpha_2)}{{\alpha_2}^2\alpha_1}\right)' + 2\Gamma^*{\alpha_1}^2u_1\right]u_r \tag{107}$$

The superscript $'$ refers to derivative with respect to α_2. By comparing the Eqs. (104)-(105) with Eqs. (47)-(48), we can see the that the variational and the mechanistic Shallow Water TFM equations are equivalent mathematical representations when written in terms of the primitive variables α_1 and u_1. This reveals that void fraction α_2 and drift flux J are natural variables for modeling adiabatic incompressible two-phase mixture with the fixed flux assumption. Using these as the state variables leads to an elegant and concise mathematical representation of the equations of motion. The inertial coupling coefficient $m(\alpha_2)$ is the relevant constitutive model which for interaction between the phases.

3.3 Bubbly Flow Inertial Coupling

The momentum transfer terms in the variational TFM require formulation of the inertial coupling coefficient $m(\alpha_2\ )$ for closure. The distribution of the dispersed phase and the nature of interaction between the two phases determines the inertial coupling coefficient. The variational approach for

deriving constitutive relations for TFM only becomes practically feasible provided $m(\alpha_2)$ is known for a given flow regime. For formulation of $m(\alpha_2)$, potential flow theory has been suggested and used over the years by Wallis [22], Wijngaarden [23], Smereka and Militon [24] and Kok [25] . From potential flow theory calculation, $m(\alpha_2)$ is the coefficient of the kinetic energy density of two-phase mixture due to coupling between the phases. This part of the report starts with the use of potential flow theory for formulation of $m(\alpha_2)$ for single bubble motion, followed by interaction between a pair of bubbles.

To begin with, a short introduction is given regarding basics of potential flow theory. The formulation of potential functions for different kinds of flows is described briefly to outline in particular the potential functions to be used for two-phase flow problems being analyzed. For an irrotational flow, the vorticity $\boldsymbol{\omega}$ follows $\boldsymbol{\omega} = \nabla \times \boldsymbol{u} = 0$. Since the curl of a gradient of any scalar field is zero, the velocity field can be written as,

$$\boldsymbol{u} = \nabla\phi \tag{108}$$

where, ϕ ($\boldsymbol{r}$, t) is called the velocity potential. Since $\nabla . \boldsymbol{u} = 0$ from the mass conservation equation for steady incompressible flow, the velocity field can be rewritten as,

$$\nabla . \boldsymbol{u} = \nabla . (\nabla\phi) = \nabla^2\phi\ (\boldsymbol{r}) \tag{109}$$

where ϕ ($\boldsymbol{r}$) is a harmonic function satisfying the Laplace equation. The Laplace equation can be solved using the method of separation of variables in a spherical geometric representation.

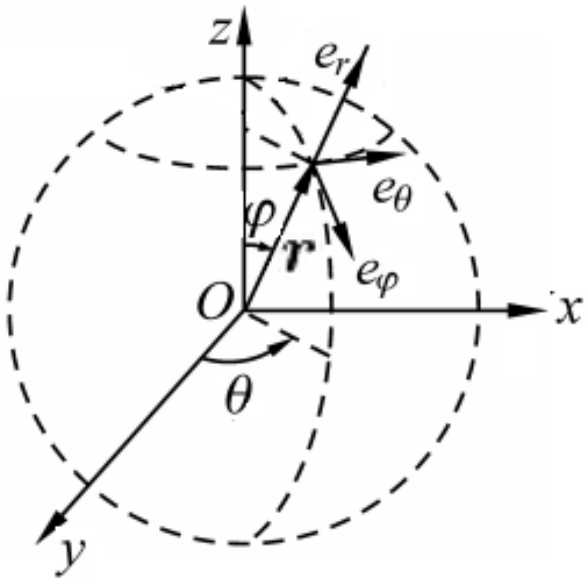

Figure 9: Spherical Coordinate System

For the spherical geometry shown in Fig. 9, the azimuthal angle θ is measured from the y-axis and the polar angle φ is measured from the z-axis. Using spherical coordinate system and assuming azimuthal symmetry, i.e., symmetric in θ with $0 \leq \theta \leq 2\pi$, the velocity potential can be written in terms of harmonic functions as,

$$\phi\,(\boldsymbol{r}) = R(r)\;\delta\;(\varphi) = \sum_{n=0}^{\infty}\left\{A_n r^n + B_n r^{-(n+1)}\right\}\dot{P}_n\,(cos\varphi) \tag{110}$$

In Eq. (110), φ is the polar angle, A_n and B_n are arbitrary constants yet to be defined, $\dot{P}_n$ represents the Legendre polynomial of degree n $\left(\dot{P}_0(\dot{\mu}) = 1,\ \dot{P}_1(\dot{\mu}) = \mu,\ \ \dot{P}_2(\dot{\mu}) = \frac{3}{2}\dot{\mu}^2 - \frac{1}{2}\right)$ and r is the spherical radius such that $r^2 = z^2 + y^2 + x^2$ with $z = r\,cos\varphi$. It is worthwhile to note that Laplace equation is linear and solutions of Laplace equation can be linearly superimposed. So considering only the first three non-trivial terms with coefficients B_0, A_1 and B_1, the velocity potentials for uniform flow, a dipole and uniform flow over a sphere can be determined .

Uniform Flow

Let $B_n's = 0$ and $A_n = 0$ except A_1. This will give,

$$\phi_{Uniform\ Flow} = A_1 r\, cos\varphi = A_1 z$$
or
$$\boldsymbol{u} = \nabla\phi = A_1 e_z \tag{111}$$

where e_z is the unit vector along z-axis. Eq. (111) represents uniform flow along the z-direction and the velocity magnitude is given by constant A_1.

Dipole

Let $A_n's = 0$ and $B_n's = 0$ except for B_1. The velocity potential will then be,

$$\phi_{Dipole} = \frac{B_1 cos\varphi}{r^2} = \frac{B_1 z}{r^3}$$
$$= \lim_{\delta z \to 0} \frac{-B_1/\delta z}{\left[\left(z + \frac{\delta z}{2}\right)^2 + y^2 + x^2\right]^{1/2}} + \frac{B_1/\delta z}{\left[\left(z - \frac{\delta z}{2}\right)^2 + y^2 + x^2\right]^{1/2}} \tag{112}$$

Now Eq. (112) represents a dipole (velocity dipole), also known as doublet (velocity doublet).

Uniform Flow over a Sphere

By linear superposition of the potentials due to dipole and uniform flow, the axisymmetric potential flow over a sphere is

$$\phi_{Sphere} = \left(A_1 r + \frac{B_1}{r^2}\right) cos\varphi \tag{113}$$

Choosing $A_1 = w$ will satisfy $\phi_{Sphere} \to w\, r\, cos\varphi$ as $r \to \infty$. By applying kinematic boundary condition $\partial\phi_{Sphere}/\partial r = 0$ at $r = a$ and solving for B_1 yields $B_1 = a^3 w/2$. The final form of Eq. (113) turns out to be,

$$\phi_{Sphere} = \phi_{Dipole} + \phi_{Uniform\ Flow} = w\left(r + \frac{a^3}{2r^2}\right) cos\varphi \tag{114}$$

Eq. (114) gives uniform flow along z-direction with the sphere being stationary, which means visualizing the motion of liquid and the sphere from a frame of reference moving with the velocity of the sphere. This gives physical meaning to the w as the relative velocity. To look at the same problem from a frame moving within the liquid, additional potential of $\phi_1 = -wz = -w\, r\, cos\varphi$ needs to be added. This additional potential ϕ_1 will give the potential for a single sphere moving through the liquid given by,

$$\phi(r, \varphi) = \frac{wa^3}{2r^2} cos\varphi \tag{115}$$

3.3.1 Single Bubble

Now consider the motion of a single bubble (dilute limit) moving through a liquid. The bubble is considered to be incompressible and perfectly spherical in shape and the velocity potential is given by Eq. (114). Let the void fraction of the bubble and the liquid be defined as

$$\alpha_2 = \frac{V_{bubble}}{V_{total}} = \frac{\frac{4}{3}\pi a^3}{V_{total}}$$
$$\alpha_1 = \frac{V_{liquid}}{V_{total}} = 1 - \frac{V_{bubble}}{V_{total}} = 1 - \alpha_2 \tag{116}$$

where a is the radius of the spherical bubble. The potential for a single spherical bubble moving at a vertical speed w through a fluid in spherical coordinates is given by,

$$\phi(r, \varphi) = \frac{wa^3 cos\varphi}{2\, r^2} \tag{117}$$

The above velocity potential in Eq. (117) takes into consideration the azimuthal symmetry. The total liquid kinetic energy is then given by,

$$K'_1 = \frac{\rho_1}{2} \int u^2 \, dV = \frac{\rho_1}{2} \int \nabla\phi . \nabla\phi \, dV \tag{118}$$

where K'_1 represents the kinetic energy of the liquid with respect to a reference frame moving with the average liquid velocity. Eq. (118) can be simplified using the well know vector identity

$$\nabla\phi . \nabla\phi \; = \; \nabla . (\phi \nabla\phi) - \; \phi \nabla^2 \phi = \; \nabla . (\phi \nabla\phi) \tag{119}$$

Applying Gauss divergence theorem, Eq. (119) can be written as,

$$K'_1 = \frac{\rho_1}{2} \int \nabla\phi . \nabla\phi \, dV = \frac{\rho_1}{2} \int \nabla . (\phi \nabla\phi) \; dV$$
$$= \frac{\rho_1}{2} \int n . (\phi \, \nabla\phi) \, ds = \frac{\rho_1}{2} \int \phi \, \boldsymbol{u} . \boldsymbol{n} \, ds \tag{120}$$

Now Eq. (120) needs to be evaluated at two surfaces, one on the sphere S_b and the other one S far away from the sphere as,

$$K'_1 = \frac{\rho_1}{2} \int_{S_b} \emptyset \, \boldsymbol{u} . \boldsymbol{e_r} ds + \int_S \emptyset \, \boldsymbol{u} . \boldsymbol{e_r} ds \tag{121}$$

where S_b stands for the surface of the bubble and $\boldsymbol{e_r}$ is the unit vector along the radial direction. Since the velocity varies with distance from the center of the sphere as $1/r^3$, the surface integral at infinity is negligible and Eq. (121) yields,

$$K'_1 = \frac{\rho_1 w^2}{4} \int_0^{\pi} \left(\frac{a\, cos\varphi}{2}\right) 2\pi\, a^2\, sin\varphi\, cos\varphi\, d\varphi = \frac{\rho_1 w^2}{2}\left(\frac{1}{2}\right)\left(\frac{4}{3}\pi a^3\right) \tag{122}$$

Eq. (122) gives kinetic energy of the liquid for the entire volume of the liquid; kinetic energy of the liquid per unit volume of the two-phase mixture will be

$$K'_1 = \frac{\frac{\rho_1 w^2}{2}\left(\frac{1}{2}\right)\left(\frac{4}{3}\pi a^3\right)}{V_{total}} = \frac{\rho_1 w^2}{2}\left(\frac{\alpha_2}{2}\right) \tag{123}$$

Assuming that the single-bubble configuration (isolated) is the most elemental one can think for bubbly flow, for a more general case, Eq. (123) can be written alternatively as,

$$K'_1 = \frac{\rho_1 w^2}{2}\breve{k}(\alpha_2) \tag{124}$$

In the dilute limit,

$$\lim_{\alpha_2 \to 0} \breve{k}(\alpha_2) = \frac{\alpha_2}{2} \tag{125}$$

The $\breve{k}(\alpha_2)$ represents the liquid kinetic energy density coefficient in the reference frame moving with the average liquid velocity. The relation between $m(\alpha_2)$ in the Lagrangian density defined by Geurst [21] and $\breve{k}(\alpha_2)$ was given by Kok [25] through coordinate transformations as,

$$\breve{k}(\alpha_2) = 0.5\, M_1\alpha_2(1 + M_2\alpha_2 + M_3{\alpha_2}^2 + \cdots + M_n{\alpha_2}^n) + O({\alpha_2}^{n+1})$$

$$m(\alpha_2) = 0.5\, M_1\alpha_2\left[1 - \frac{M_1(2 - M_2) + 2}{M_1}\alpha_2 + \frac{M_1(1 - 2M_2 + M_3) + 2}{M_1}{\alpha_2}^2\right] + O({\alpha_2}^4) \tag{126}$$

From Eqs. (125)-(126), $M_1 = 1$ and $M_i = 0$, for i = 2, 3…n. Hence the inertial coupling coefficient of the net kinetic energy density of the single bubble motion will be,

$$m(\alpha_2) = \frac{\alpha_2}{2} \tag{127}$$

Following Wallis [22], the virtual mass and interfacial pressure coefficients can be calculated for a single sphere in the dilute limit $\alpha_2 \to 0$ as,

$$c_{vm} = \frac{m(\alpha_2)}{\alpha_2} = \frac{1}{2}$$
$$c_p = \frac{m(\alpha_2) + \alpha_1 m'(\alpha_2)}{2\alpha_1} = \frac{1}{4} \quad (128)$$

The $c_{vm} = 0.5$ and $c_p = 0.25$ in Eq. (128) here correspond to the values used for dispersed bubbly flows in the mechanistic TFM and are valid only in the limit $\alpha_2 \to 0$. It is worthwhile to note that $m(\alpha_2)$ in Eq. (127) is for single bubble and lacks the physics of interaction with other bubbles, but considers the kinetic coupling with the surrounding liquid.

3.3.2 Two-Body: Motion along the line of centers

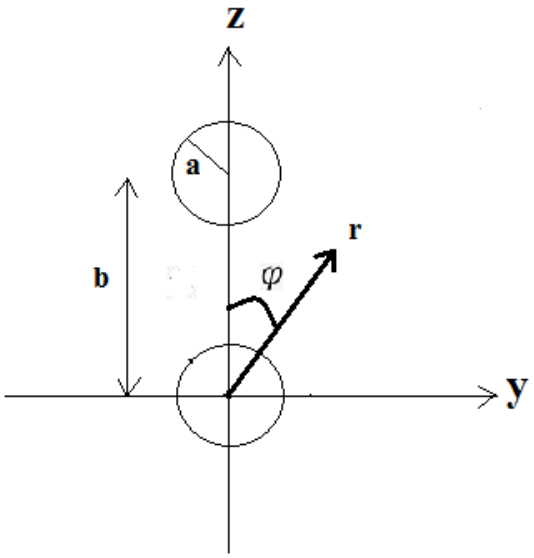

Figure 10: Motion of two bubbles along the line joining their centers

Consider the problem of two bubbles (two spheres) of same radii and equal velocities moving along the line joining their centers in polar coordinates, assuming azimuthal symmetry as shown in Fig. 10. Since both the spheres are of same radius a, the dipole strengths should be the same due to symmetry. By linear superposition of potential functions of each velocity dipoles, the net potential for motion of the two bubbles can be written as,

$$\phi_{net} = \phi_1(r, \varphi) + \phi_2(r', \varphi') = \frac{wa^3 cos\varphi}{2\, r^2} + \frac{wa^3 cos\varphi'}{2\, r'^2} \quad (129)$$

where φ' and r'^2 correspond to the second sphere and are defined using transformation of coordinates as,

$$\varphi' = tan^{-1}\left[\frac{y'}{z'}\right] = tan^{-1}[\frac{r\,sin\varphi}{r\,cos\varphi - b}]$$
$$r'^2 = r^2 + b^2 - 2rbcos\varphi \tag{130}$$

The net kinetic energy of the liquid will be,

$$K'_1 = \frac{\rho_1}{2}\int_{S_1}\phi_{net}\,\boldsymbol{u}.\boldsymbol{e_r}ds + \int_{S_2}\phi_{net}\,\boldsymbol{u}.\boldsymbol{e_r}ds \tag{131}$$

where S_1 and S_2 represent the two bubble surfaces over which, the surface integral needs to be evaluated. Eq. (131) gives the net liquid kinetic energy as,

$$K'_1 = \frac{\rho_1 w^2}{2}\breve{k}(\alpha_2, b) \tag{132}$$

Using Eqn. 132, The coefficients $k(\alpha_2, s)$ and $m(\alpha_2, s)$, where $s = b/a$ is the non-dimensional distance between the bubbles, are,

$$\begin{aligned}\breve{k}(\alpha_2, s) &= m(\alpha_2, s)\\ &= \frac{\alpha_2}{32s^3\sqrt{1+s^2}}\Big[-12s + 36s^3 + 16s^3\sqrt{1+s^2}\\ &\quad - (3 + 6s^2 + 9s^4)\text{Log}(1-s)^2 + (3 - 6s^2 - 9s^4)\text{Log}(1+s)^2\Big]\end{aligned} \tag{133}$$

The virtual mass coefficient, $c_{vm}(s)$, for the configuration shown in Fig. 16 using $c_{vm} = m(\alpha_2)/\alpha_2$ will be,

$$\begin{aligned}C_{vm}(s) &= \frac{1}{32s^3\sqrt{1+s^2}}\Big[-12s + 36s^3 + 16s^3\sqrt{1+s^2} - (3 + 6s^2 + 9s^4)\text{Log}(1-s)^2\\ &\quad + (3 - 6s^2 - 9s^4)\text{Log}(1+s)^2\Big]\end{aligned} \tag{134}$$

In Eq. (92), $c_{vm}(s)$ decreases as the distance between the bubbles is decreasing and similar trend was been obtained by Wijngaarden [23] given by,

$$c_{vm}^{Wijngaarden} = \frac{1}{2}\left[1 - 3\left(\frac{1}{s}\right)^3 + 3\left(\frac{1}{s}\right)^6 + 9\left(\frac{1}{s}\right)^8 - 3\left(\frac{1}{s}\right)^9 + \cdots\right] \tag{135}$$

Eq. (135) was obtained by Wijngaarden [23] by solving 3D potential over two spheres in spherical coordinates and using a complete spherical harmonic solution of the Laplace equation for the velocity potential. From Eq. (134), the virtual mass coefficient for a pair of bubbles (s = 2) is 0.33,

a value close to 0.35 obtained by Bentwich and Miloh [56] .By solving for the liquid kinetic energy using stream function rather than potential function, Bentwich and Miloh [56] derived the exact solution for the two-body problem using bi-spherical coordinates. The variation of C_{vm} (s) with respect to non-dimensional distance s, along with its comparison with the analytical solutions of Wijngaarden [23] and Bentwich and Miloh [56] is shown in Fig. 11.

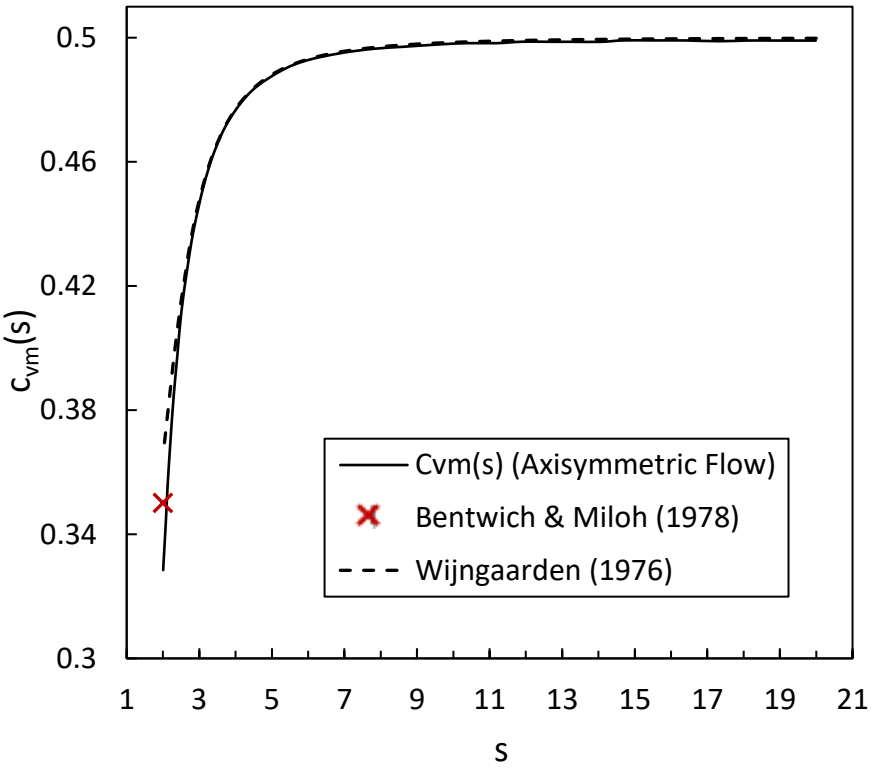

Figure 11: Virtual mass coefficient for bubbles moving along the center line

3.4 Slug Flow Inertial Coupling

In the first part of this section, the derivation of an analytical expression for inertial coupling coefficient $m(\alpha_2)$ is performed using the lumped parameter model proposed by Wallis [22] and will referred to as Wallis model and also discussed by Clausse. The lumped parameter model uses an idealized flow pattern and corresponding average flow velocities for the two-phase distribution. The essence of this model lies in analyzing the kinetic coupling (interaction) between the gas phase and the liquid phase. In the second part, the wake entrainment effect is proposed as the physical mechanism responsible for clustering of Taylor bubbles. Therefore, a modified model with a trailing vortex is developed.

3.4.1 Wallis Model

Consider a unit cell configuration of a cylindrical bubble moving in the axial direction along with the liquid in a vertical pipe as shown in Fig. 12. The bubble moves with velocity u_2 and it occupies a fraction α_s of the cross-section of the pipe. The liquid has two different velocities, u_f in the film around the bubble, and u_s in the liquid slug, where $u_s = 0$ because the reference frame is moving at j_0. From Fig. 12, the volume averaged gas void fraction,

$$\alpha_2 = \frac{H_g\, D_g^2}{H\, D^2} \tag{136}$$

The fraction of the cross-sectional area of the pipe occupied by the cylindrical bubble is given by,

$$\alpha_s = \frac{D_g^2}{D^2} \tag{137}$$

Using the fixed flux approximation with respect to the moving frame $j = \alpha_2 u_2 + \alpha_1 u_1 = 0$ across the Taylor bubble and liquid slug region, we have,

$$u_1 = \frac{-\alpha_2 u_2}{\alpha_1}, \qquad u_s = 0, \qquad u_f = \left(\frac{\alpha_s}{1-\alpha_s}\right) u_2 \tag{138}$$

where α_1 and u_1 are the void fraction and volume averaged velocity of the liquid region in the unit cell. Now we can define the volume averaged kinetic energy density K of the two-phase mixture in the unit cell as,

$$K = \frac{1}{2}\rho_2 \alpha_2 {u_2}^2 + \frac{1}{2}\rho_1 (1-\alpha_s)\left(\frac{H_g}{H}\right){u_f}^2 \tag{139}$$

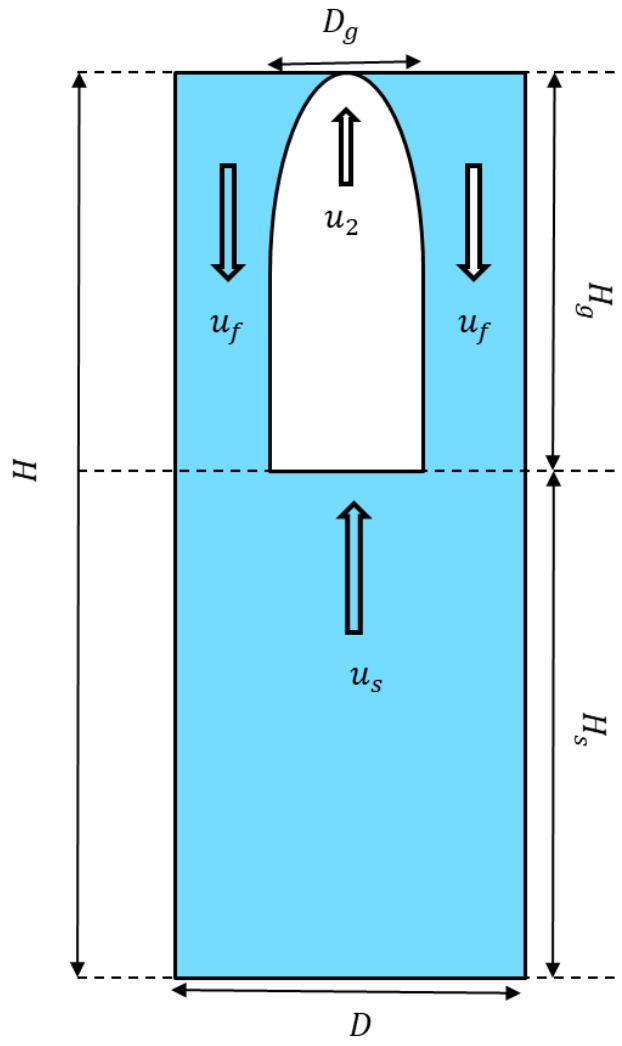

Figure 12: Wallis model for slug flow

By using the definition $J = \alpha_1 \alpha_2 u_r$ for drift flux, u_1, u_2 and u_f can be written as,

$$\begin{aligned} u_1 &= \frac{-J}{\alpha_1} \\ u_2 &= \frac{J}{\alpha_2} \\ u_f &= \left(\frac{-\alpha_s}{1-\alpha_s}\right)\frac{J}{\alpha_2} \end{aligned} \tag{140}$$

Using $H_g/H = \alpha_2/\alpha_s$, the kinetic energy density K in can be rewritten as,

$$K = \frac{1}{2}\frac{J^2}{\alpha_2}\left(\rho_2 + \rho_1\left(\frac{\alpha_s}{1-\alpha_s}\right)\right) \tag{141}$$

Representing the net effective inertia of the two-phase mixture as Γ_{Wallis}, following Pauchon and Smereka [20], the kinetic energy density can be written as,

$$K = \frac{1}{2}\Gamma J^2 \tag{142}$$

where

$$\Gamma = \frac{\left(\rho_2 + \rho_1\left(\frac{\alpha_s}{1-\alpha_s}\right)\right)}{\alpha_2} \tag{143}$$

Now the definition of the inertial coupling coefficient $m(\alpha_2)$ can be obtained from the definition of Γ by using the following relation (Pauchon and Smereka [20]),

$$\Gamma = \frac{\rho_1}{\alpha_1} + \frac{\rho_2}{\alpha_2} + \frac{\rho_1\, m(\alpha_2)}{{\alpha_1}^2{\alpha_2}^2} \tag{144}$$

Using Eq. (142) and Eq. (144), $m(\alpha_2)$ may be obtained by performing some elementary algebraic operations. However, a much more physically intuitive way to obtain $m(\alpha_2)_{Wallis}$ is to rewrite the volume averaged kinetic energy density K given by Eq. (142), using the definitions of $J = \alpha_1\alpha_2 u_r$ and u_1, u_2 and u_f in Eq. (47), in the following form,

$$K = \frac{\rho_1}{2}\alpha_1{u_1}^2 + \frac{\rho_2}{2}\alpha_2{u_2}^2 + \frac{\rho_1}{2}m(\alpha_2)_{Wallis}{u_r}^2 \tag{145}$$

and this gives,

$$m(\alpha_2)_{Wallis} = (1-\alpha_2)\alpha_2\left(\frac{\alpha_s - \alpha_2}{1-\alpha_s}\right) \tag{146}$$

It is important to note that the $m(\alpha_2)_{Wallis}$ has been obtained for a moving Taylor bubble in a fixed j_0 frame of reference. A nice feature of the $m(\alpha_2)_{Wallis}$ in Eq. (146) is that it leads to zero added mass for the limiting case of $\alpha_1 = 0$ and $\alpha_2 = 0$. Fig. 13 shows the plot of the behavior of $m(\alpha_2)_{Wallis}$ for $\alpha_s = 0.87$.

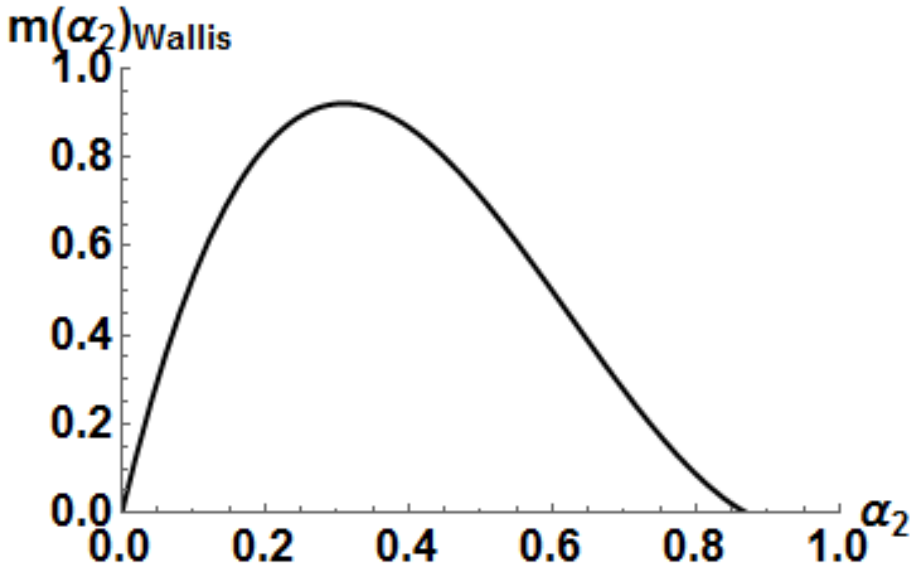

Figure 13: Inertial coupling coefficient for Wallis model

The $m(\alpha_2)_{Wallis}$ in Eq. (146) can be verified by comparing it with the mechanistic inertial coupling coefficient for slug flows derived by Ishii and Mishima [32]. By using potential flow theory to derive the virtual mass force based on relative acceleration between a Taylor bubble and the liquid, Ishii and Mishima [32] obtain the virtual mass force acting for the Taylor bubble $\vec{M}_{2i}^{VM}$ as,

$$\vec{M}_{2i}^{VM} = -\rho_1 5\alpha_2 \left[0.66 + 0.34\left(\frac{1-\frac{D_g}{H_g}}{1-\frac{D_g}{3H_g}}\right)\right]\left(\frac{D_2 u_r}{Dt} - u_r\frac{\partial u_1}{\partial x}\right) \tag{147}$$

According to the variational formulation of the 1D Two-Fluid Model of Pauchon and Smereka [20], the virtual mass force acting on the dispersed phase $\vec{M}_{2i}^{VM}$ is,

$$\vec{M}_{2i}^{VM} = -\rho_1 m(\alpha_2)\left(\frac{D_2 u_r}{Dt} - u_r\frac{\partial u_1}{\partial x}\right) \tag{148}$$

It can be inferred from a straight forward comparison between Eq. (147) and Eq. (148) that the $m(\alpha_2)$ from the virtual mass force term of Ishii and Mishima [32] is,

$$m(\alpha_2)_{Mechanistic} = 5\alpha_2\left(0.66 + 0.34\left(\frac{1-\frac{D_g}{H_g}}{1-\frac{D_g}{3H_g}}\right)\right) \tag{149}$$

For the case of a cylindrical bubble, using $H_g \gg D_g$, Eq. (56) simplifies to a linear relation in α_2,

$$m(\alpha_2)_{Mechanistic} = 5\alpha_2 + O[\alpha_2]^2 \quad (150)$$

which is a first order approximation of $m(\alpha_2)_{Mechanistic}$. In the current analysis of Wallis's slug flow model without the Taylor bubble's confined vortex, for $\alpha_s = 0.90$ (which is a physically reasonable approximation for slug flows), Eq. (146) gives,

$$m(\alpha_2)_{Wallis} = 5.67\alpha_2 + O[\alpha_2]^2 \quad (151)$$

3.4.2 Averaging and Inertial Coupling

The purpose of this section is to demonstrate analytically, the range of applicability and mathematical accuracy of the formulation of the inertial coupling coefficient using the variational method. It is shown here that the inertial coupling coefficient derived from variational principles can be used for solving both the local interfacial structures as well for the averaged solution where there are no flow structures being resolved (uniform profile). The kinetic energy of the liquid, obtained from the SWT using variational approach for three different conceptual models is analyzed and compared.

Model-1:

The lumped parameter model with $\alpha_2 = \alpha_s$ represents the model of Wallis [22] in theory as shown in Fig. 14.

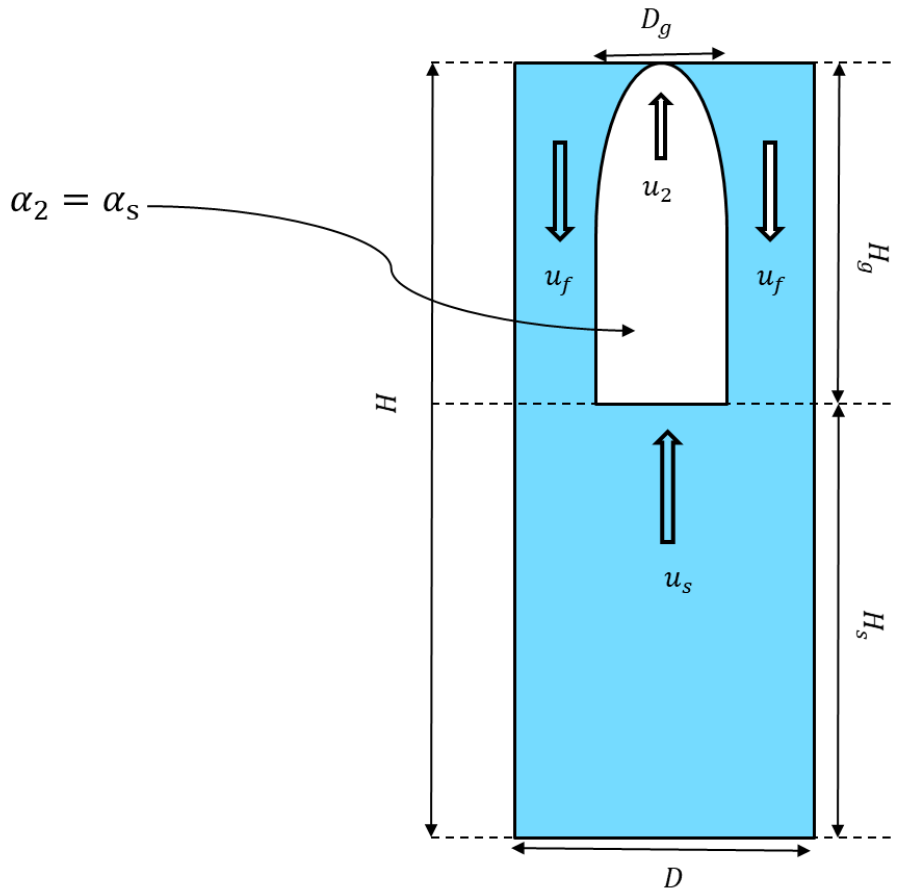

Figure 14: Slug flow unit cell of Wallis model for Model-1

The volume averaged kinetic energy density of the liquid phase in the unit cell from theory is,

$$K_{1,theory} = \frac{1}{2}\left(\frac{H_g}{H}\right)\rho_1(1-\alpha_2){u_1}^2 = \left(\frac{H_g}{H}\right)\frac{\rho_1}{2}\frac{J^2}{(1-\alpha_s)} \tag{152}$$

Now consider the Wallis' slug flow model for the case when $\alpha_2 = \alpha_s$, since α_s is the maximum value the local void fraction α_2 can attain. From the Lagrangian,

$$K_{1,model1} = \frac{1}{H}\int_0^{H_g}\frac{1}{2}\,\Gamma\,\langle J\rangle^2\,dx = \left(\frac{H_g}{H}\right)\frac{1}{2}\,\Gamma\,\langle J\rangle^2 \tag{153}$$

If the kinetic energy density of the Taylor bubble is not considered due to $\rho_2 \ll \rho_1$, then with $\alpha_2 = \alpha_s$, $\langle J\rangle = \alpha_2 u_2$ and $J = \alpha_s u_2$ we have,

$$K_{1,model1} = \left(\frac{H_g}{H}\right)\frac{\rho_1}{2}\frac{J^2}{(1-\alpha_s)} \tag{154}$$

which agrees with $K_{1,theory}$. This shows that if the local void fraction ever reaches α_s, then the inertial coupling terms vanish and this case corresponds to a Direct Numerical Simulation (DNS) type model which has no virtual mass in it.

Model-2

Now consider the averaged case as shown in Fig. 15, in which the local interfacial structures are not resolved.

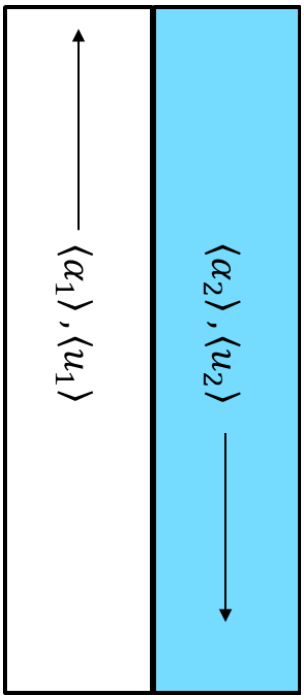

Figure 15 : Averaged two-phase flow model

For this case, the averaged void fraction $\langle\alpha_2\rangle = \alpha_2$ and uniform averaged values for void fraction, bubble velocity and the drift flux and the local drift flux follow,

$$\langle\alpha_2\rangle = \alpha_s\left(\frac{H_g}{H}\right), \qquad \langle u_2\rangle = u_2 \tag{155}$$

$$\langle J\rangle = \alpha_2\, u_2\,, \qquad J = \alpha_s\, u_2$$

Then the averaged kinetic energy density from the Lagrangian for the liquid phase gives,

$$K_{1,model2} = \frac{1}{2}\rho_1\left(\frac{1}{1-\alpha_2} + \frac{\alpha_s - \alpha_2}{\alpha_2(1-\alpha_2)(1-\alpha_s)}\right)\langle J\rangle^2 \tag{156}$$

Using Eq. (155),

$$K_{1,model2} = \left(\frac{H_g}{H}\right)\frac{\rho_1}{2}\frac{J^2}{(1-\alpha_s)} \tag{157}$$

The $K_{1,model2}$ is same as the theory if $K_{1,theory}$ is written in terms of α_s. Model-2 represents the stable averaged case generally used for CFD simulations using the TFM.

Model-3:

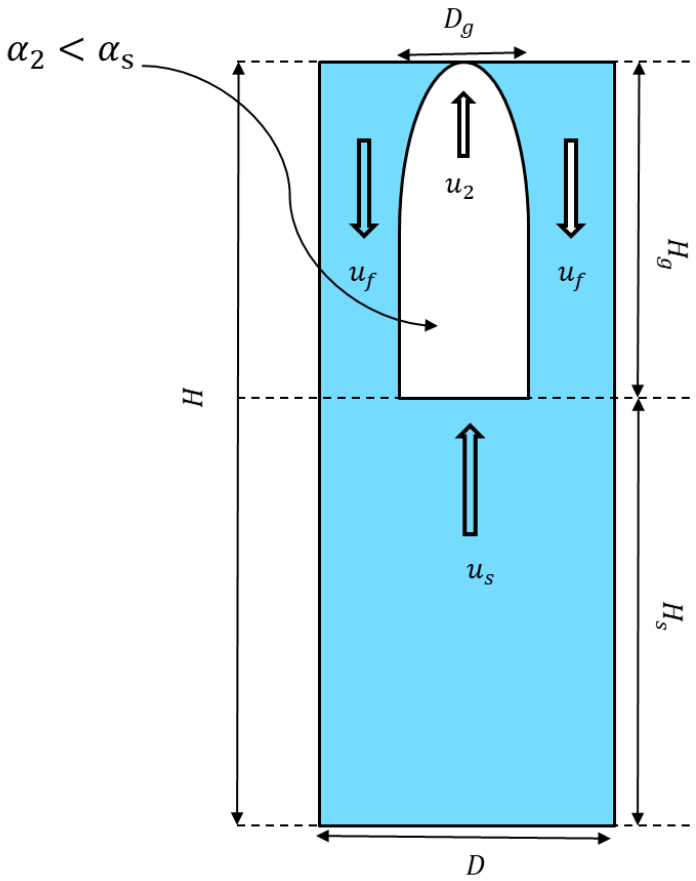

Figure 16: Slug flow unit cell of Wallis model for unstable simulations

Now consider the case for $\alpha_2 < \alpha_s$ as shown in Fig. 16. This case corresponds to the simulation type in which the liquid film is thicker and the length of the Taylor bubble H_{g2} is longer than H_g of Wallis' model, such that the void fraction in the cell remains the same. This gives the following relation,

$$\frac{H_{g2}}{H} = \frac{\alpha_s}{\alpha_2}\left(\frac{H_g}{H}\right) \tag{158}$$

The volume averaged kinetic energy density for liquid in the unit cell is,

$$K_{1,model3} = \frac{1}{H}\int_0^{H_{g2}} \frac{1}{2}\,\Gamma\,J^2\,dx = \frac{\alpha_s}{\alpha_2}\left(\frac{H_g}{H}\right)\frac{1}{2}\,\Gamma\,J^2 \tag{159}$$

where,

$$\begin{gathered}\alpha_2 = \alpha_s \frac{H_{g2}}{H} \\ \langle J \rangle = \alpha_2\, u_2 \\ J = \alpha_s\, u_2\end{gathered} \tag{160}$$

Using the definitions in Eq. (159) and assuming $\langle \alpha_2 \rangle = \alpha_2$,

$$K_{1,model3} = \left(\frac{H_g}{H}\right)\frac{\rho_1}{2}\frac{J^2}{1-\alpha_s} \tag{161}$$

According to the Wallis' model, writing the kinetic energy density of the liquid in terms of the liquid film gives,

$$K_{theory} = \frac{\rho_1}{2}\left(\frac{H_g}{H}\right)(1-\alpha_s)\,{u_f}^2 = \left(\frac{H_g}{H}\right)\frac{\rho_1}{2}\frac{J^2}{1-\alpha_s} \tag{162}$$

which agrees with the model as required. For this case where $\alpha_2 < \alpha_s$, certain amount of averaging is still present, and this is the model being used for present work for unstable simulations of SWT-TFM. Also, this case lies between the other two extremes, the one which corresponds to the DNS type and the other where the stable averaged solution is solved for.

3.4.3 Vortex Model

The purpose of this section is to develop a model for the presence of a confined toroidal vortex behind a Taylor bubble using data obtained by Shemer et al. [57]in air-water slug flow in vertical circular pipes, for different pipe diameters at various Reynolds numbers based on average liquid velocity Re_L. The flow field obtained by Shemer et al. [57] using the PIV technique for a confined vortex behind the Taylor for turbulent wake (Re_L = 7400) given in Fig. 17.

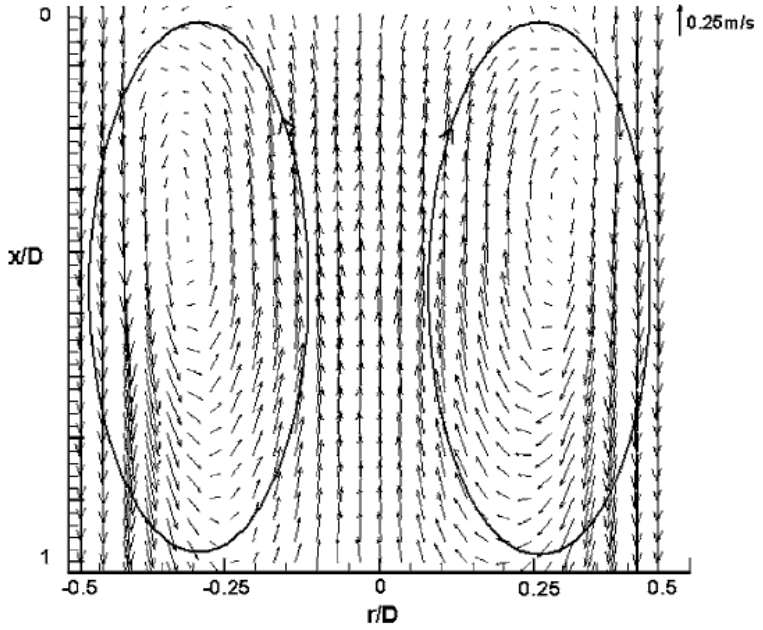

Figure 17: Mean flow field of confined vortex for Re = 7400 (Shemer et al. [57])

Shemer et al. [57] measured the axial distribution of the wake's axial velocity (u_{cl}) normalized using the Taylor bubble's terminal velocity u_{tr} and the mean liquid velocity u_1 (u_L) as shown in Fig. 18.

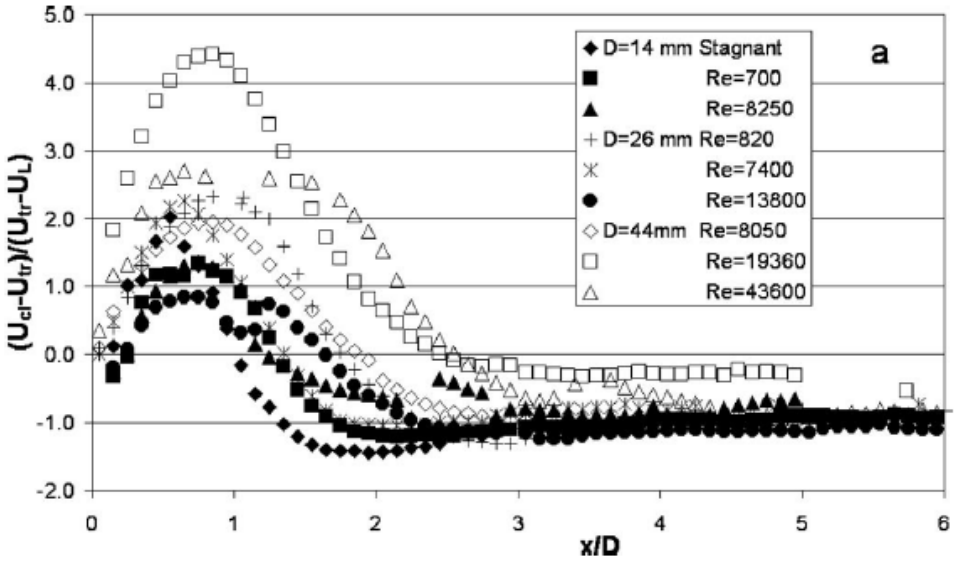

Figure 18: Axial distribution of centerline axial velocity of confined vortex

Let us assume, for simplicity, separation of the spatial variables, x and r, is applicable. Then the spatial distribution of the confined vortex velocity field in the reference system for which $j = 0$ can be written as,

$$u_w(x^*, r^*) = u_2\, Q(r^*)\, X(x^*) \tag{163}$$

where $x^* = x/H_w$ and $r^* = r/R_{pipe}$, with H_w and R_{pipe} being an appropriate length scale for vortex decay and radius of the pipe respectively. $Q(r^*)$ and $X(x^*)$ are the radial and axial distribution functions respectively. Since the flow is incompressible and adiabatic, for the fixed flux assumption $j_0 = 0$ to be satisfied, the radial distribution of the type in Eq. (164) displayed in in Fig. 20 is assumed, which is consistent with the experimental data of Shemer et al. [57].

$$Q(r^*) = cos\left(\pi\, r^{*2}\right) \tag{164}$$

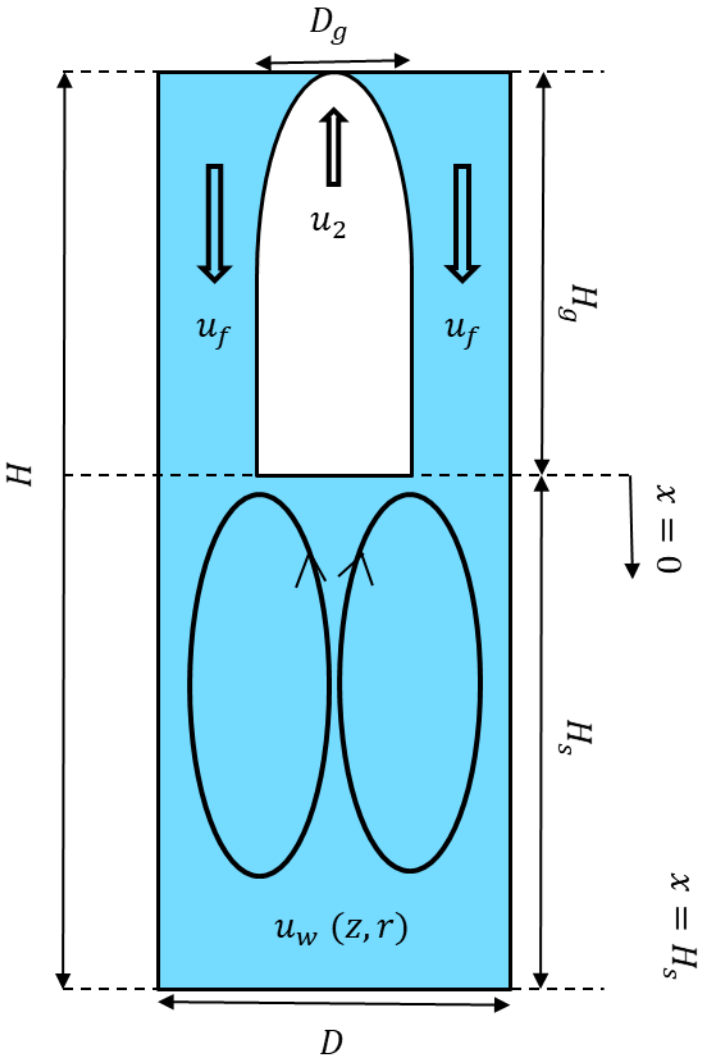

Figure 19: Lumped parameter unit cell with confined vortex behind the Taylor bubble

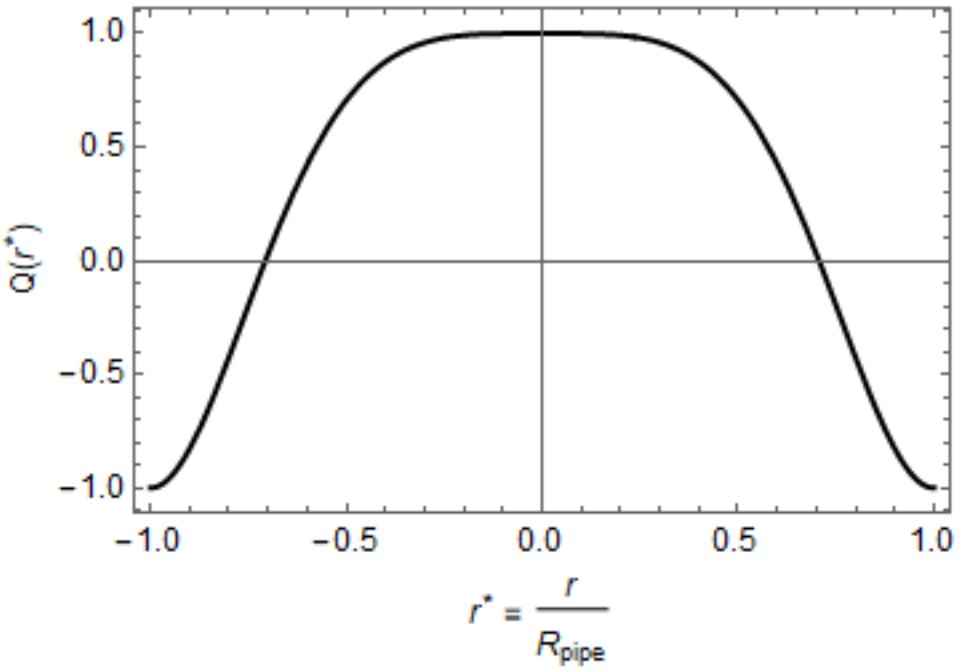

Figure 20: Radial distribution function of vortex

The $Q(r^*)$ in Eq. (164) makes sure that *j* vanishes at any axial position *x* and also ensures that u_w vanishes at any position x^* independently of the axial distribution function $X(x^*)$ since,

$$\int_0^1 Q(r^*)\, 2\pi r^*\, dr^* = 0 \tag{165}$$

The axial distribution function $X(x^*)$ is chosen to be,

$$X(x^*) = X_0 \left(\frac{1}{x^* + 1}\right) \tag{166}$$

as visualized by Fig. 21 for $X_0 = 1$,

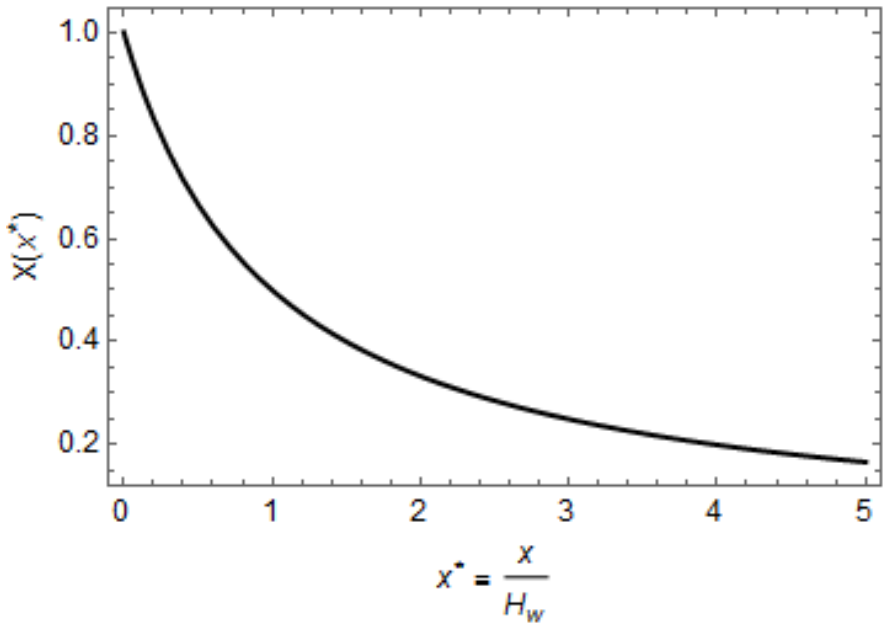

Figure 21: Axial distribution function of vortex

Now the confined vortex' contribution to the volume averaged kinetic energy density will be,

$$K_w = \frac{\rho_1}{2}\frac{\int_0^{H_s/H_w}\int_0^1 {u_w}^2(x^*,r^*)\ 2\pi r^* dr^*\ dx^*}{\int_0^{H/H_w}\int_0^1 2\pi r^* dr^*\ dx^*} \tag{167}$$

In terms of the spatial distribution functions, K_w will be,

$$K_w = \frac{\rho_1 {u_2}^2}{2}\left(\frac{H_w}{H}\right)\left(\int_0^1 Q(r^*)^2\, 2\pi r^*\, dr^*\right)\left(\int_0^{H_s/H_w} X(x^*)^2 dx^*\right) \tag{168}$$

Using Eq. (166) and Eq. (164), the net volume averaged kinetic energy density associated with the confined toroidal vortex is,

$$K_w = \frac{\rho_1 {u_2}^2}{2}\left[\frac{{X_0}^2 b_w}{2}\left(\frac{(\alpha_s-\alpha_2)}{(\alpha_s-\alpha_2)+\alpha_s b_w}\right)\right] \tag{169}$$

where $b_w = H_w/H$. In terms of the drift-flux J, K_w can be written as,

$$K_w = \frac{\rho_1 J^2}{2}\left[\frac{{X_0}^2\, b_w}{2\,\alpha_2^2}\left(\frac{(\alpha_s-\alpha_2)}{(\alpha_s-\alpha_2)+\alpha_s b_w}\right)\right] = \frac{J^2}{2}\Gamma_{vortex} \tag{170}$$

The net Γ is obtained by adding the net effective inertia from Wallis model and that of the confined vortex Γ_{vortex} as,

$$\Gamma = \left[\frac{\rho_2 + \rho_1\left(\frac{\alpha_s}{(1-\alpha_s)}\right)}{\alpha_2}\right] + \rho_1\left[\frac{{X_o}^2\, b_w}{2\,\alpha_2^2}\left(\frac{(\alpha_s - \alpha_2)}{(\alpha_s - \alpha_2) + \alpha_s b_w}\right)\right] \tag{171}$$

The net inertial coupling coefficient with contribution from the confined vortex behind the Taylor bubble is,

$$m(\alpha_2)_{vortex} = \alpha_2(1-\alpha_2)\left(\frac{\alpha_s - \alpha_2}{1-\alpha_s}\right) + (1-\alpha_2)^2\left(\frac{{X_o}^2\, b_w}{2}\right)\left(\frac{\alpha_s - \alpha_2}{(\alpha_s - \alpha_2) + \alpha_s b_w}\right) \tag{172}$$

A comparison of $m(\alpha_2)_{vortex}$ and $m(\alpha_2)_{wallis}$ is shown in Fig. 22 for $X_0 = 4$, $b_w = 0.1$ and a constant value of $\alpha_s = 0.87$. The $m(\alpha_2)_{vortex}$ from the lumped parameter model is only valid for $0.2 \leq \alpha_2 \leq \alpha_s$. The higher value of $m(\alpha_2)_{vortex}$ is attributed to the additional kinetic energy from the confined vortex. It is important to note that for lower void fractions, i.e., as $\alpha_2 \to 0$, the value of $\alpha_s = 0.87$ is no longer valid and an approximation similar to $\alpha_s \cong \alpha_2$ would be more appropriate.

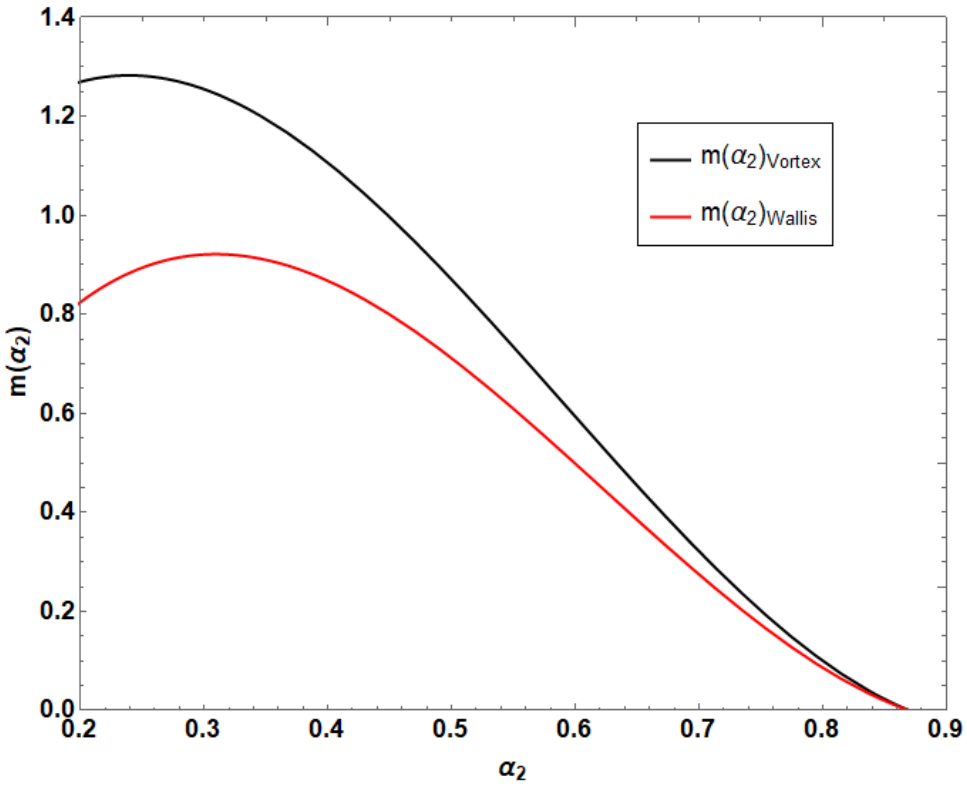

Figure 22: Comparison of inertial coupling coefficients with and without confined vortex

3.5 Linear Stability

3.5.1 Characteristic Analysis

The analysis of eigenvalues of a system of equations give an understanding of the mathematical behavior. As mentioned before, depending on the nature of the characteristic roots, the TFM system can be classified as either well-posed or ill-posed. To understand the linear stability of the variational fixed-flux model due to the inertial coupling between the two phases, the 1D variational Shallow Water TFM given in Eqs. (101)-(102) are recast into the following form in terms of the variables α_2 and $\widetilde{U}$ as,

$$\begin{pmatrix} \alpha_2 \\ \widetilde{U} \end{pmatrix}_t + \begin{pmatrix} \dfrac{-\widetilde{U}\Gamma'}{\Gamma^2} & \dfrac{1}{\Gamma} \\ \dfrac{-\widetilde{U}^2}{2}\left(\dfrac{\Gamma'}{\Gamma^2}\right)' & \dfrac{-\widetilde{U}\Gamma'}{\Gamma^2} \end{pmatrix} \begin{pmatrix} \alpha_2 \\ \widetilde{U} \end{pmatrix}_x = 0 \tag{173}$$

where $\widetilde{U} = \Gamma J$. The Eigenvalues of the system of equations in Eq. (173) are,

$$C_{1,2} = \frac{\widetilde{U}\Gamma'}{\Gamma^2}\left(-1 \pm \sqrt{\frac{2\Gamma'^2 - \Gamma\Gamma''}{2\Gamma'^2}}\right) \tag{174}$$

The stability criteria for the variational fixed flux model is dependent on $\dot{\Delta}$ defined as,

$$\dot{\Delta} = 2\Gamma'^2 - \Gamma\Gamma'' \tag{175}$$

where $\Gamma' = \partial\Gamma/\partial\alpha_2$ and $\Gamma'' = \partial^2\Gamma/\partial{\alpha_2}^2$ .For $\dot{\Delta} > 0$, the variational fixed flux model is hyperbolic as it will have real eigenvalues and $\dot{\Delta} = 0$ renders the model parabolic. For $\dot{\Delta} < 0$, the model becomes elliptic as the eigenvalues are imaginary for this case.

Wallis Model

The behavior of the variational fixed flux model for Wallis slug flow model for the Taylor bubble without confined vortex is analyzed here. The Γ for Wallis slug flow model in Eq. (143) is used for the calculation of $\dot{\Delta}$ as follows,

$$\Gamma = \frac{\left(\rho_2 + \rho_1\left(\dfrac{\alpha_s}{1-\alpha_s}\right)\right)}{\alpha_2} \tag{176}$$

$$\Gamma' = \frac{-\left(\rho_2 + \rho_1\left(\frac{\alpha_s}{1-\alpha_s}\right)\right)}{{\alpha_2}^2}$$

$$\Gamma'' = \frac{2\left(\rho_2 + \rho_1\left(\frac{\alpha_s}{1-\alpha_s}\right)\right)}{{\alpha_2}^3}$$

$$\dot{\Delta} = 2\Gamma'^2 - \Gamma\Gamma'' = 0$$

As seen from Eq. (176), the variational fixed flux model is parabolic for the Wallis's slug flow model, since $\dot{\Delta} = 0$ and the two eigenvalues coincide and give only one characteristic speed. The non-dimensional Eigen values ${C_{1,2}}^* = C_{1,2}/u_r = (1-\alpha_2)$ are shown in Fig. 23.

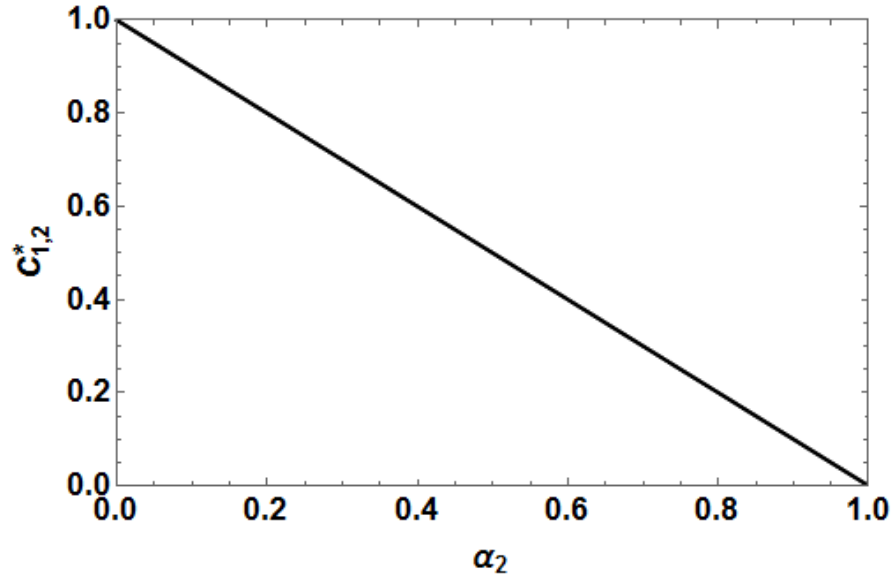

Figure 23: Non-dimensional Eigenvalues for Wallis Model

Vortex Model

The nature of the variational fixed flux TFM with a confined vortex behind the Taylor bubble is discussed here. The Eigenvalues of the system of equations in Eq. (173) are solved for the vortex model, with the Γ given in Eq. (171) and the non-dimensional Eigenvalues are shown in Fig. 24.

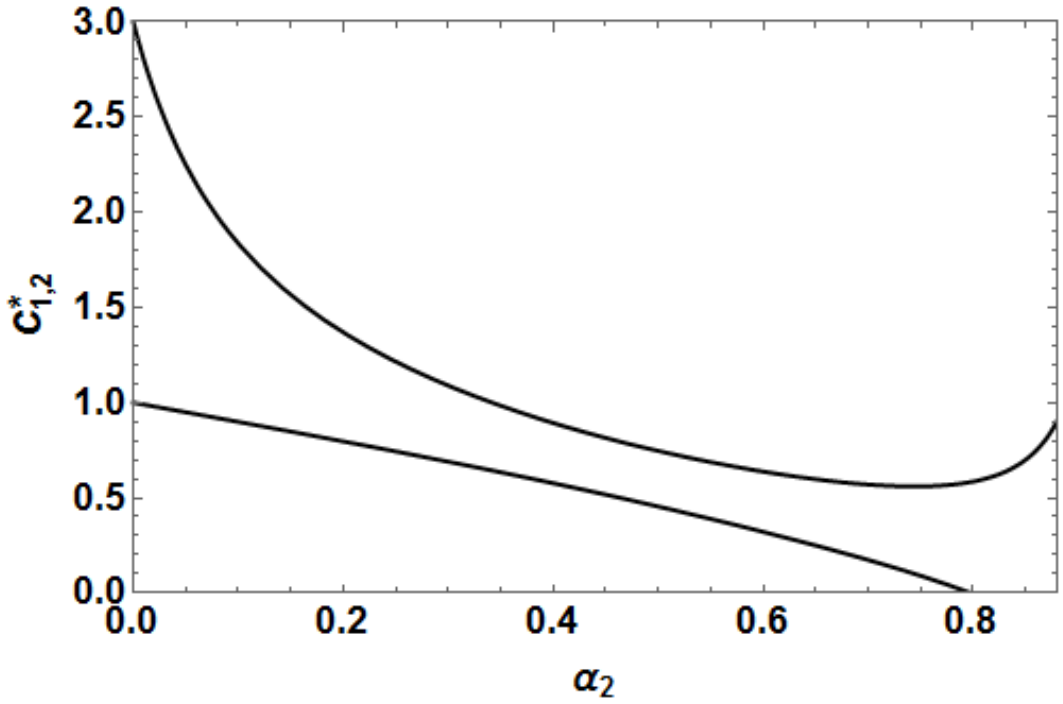

Figure 24: Non-dimensional Eigen values for confined vortex model

It is important to note that stability analysis with the vortex model is only valid for $\alpha_2 \leq \alpha_s$ and the presence of real Eigenvalues shows that the 1D variational Shallow Water TFM is hyperbolic even with a confined vortex behind the Taylor bubble. The addition of the vortex behind the Taylor bubble makes the variational fixed flux TFM hyperbolic from being parabolic.

2.1.1 Dispersion Analysis

The purpose of this section it to look into the linear stability behavior of the variational fixed-flux model in terms of dispersion relation. By including the drag and gravity forces into the momentum equation for the variational fixed flux TFM, the dispersion relation is obtained by perturbing the system of equations in Eq. (41)-(42) and recast into the form,

$$\boldsymbol{A}\frac{\partial}{\partial t}\delta\underline{\phi} + \boldsymbol{B}\frac{\partial}{\partial x}\delta\underline{\phi} + \boldsymbol{D}\frac{\partial^2}{\partial x^2}\delta\underline{\phi} + \frac{\partial \boldsymbol{F}}{\partial \underline{\phi}}\delta\underline{\phi} = 0 \tag{177}$$

where

$$\underline{\phi} = \left[\alpha_2, \widetilde{U}\right]^T \tag{178}$$

$$\boldsymbol{F} = \rho_1 \left[\frac{C_D}{D_{pipe}} \left(\frac{\widetilde{U}}{\Gamma\, \alpha_2\, (1-\alpha_2)} \right)^2 + \vec{g} \right]$$

$$\frac{\partial \boldsymbol{F}}{\partial \underline{\phi}} = \begin{pmatrix} 0 & 0 \\ F' & F_{\tilde{u}} \end{pmatrix} = \begin{pmatrix} 0 & 0 \\ \dfrac{\partial \boldsymbol{F}}{\partial \alpha_2} & \dfrac{\partial \boldsymbol{F}}{\partial \widetilde{U}} \end{pmatrix}$$

For a perturbation assumed to be a travelling wave given by,

$$\delta \underline{\phi} = \delta \underline{\phi}_0 e^{i(kx-\omega t)} \tag{179}$$

where $k = 2\pi/\lambda$ and the constraint equation for the growth rate reduces to following expression for a non-trivial solution to exist,

$$\det \left[\omega \boldsymbol{A} - k\boldsymbol{B} - ik^2 \boldsymbol{D} + \frac{\partial \boldsymbol{F}}{\partial \underline{\phi}} \right] \delta \underline{\phi} = 0 \tag{180}$$

and the dispersion relation is,

$$\omega_{1,2}(k) = \frac{1}{2} \left(-\frac{2k\widetilde{U}\Gamma'}{\Gamma^2} - iF_{\tilde{u}} \pm \frac{\sqrt{-4i\, F_{\alpha_2} k\, \Gamma^3 - {F_{\tilde{u}}}^2 \Gamma^4 + 2\, k^2\, M^2 \left(2\, \Gamma'^2 - \Gamma\Gamma''\right)}}{\Gamma^2} \right) \tag{181}$$

Wallis Model

The dispersion relation for Γ from the slug flow model of Wallis without drag and gravity forces is visualized Fig. 25.

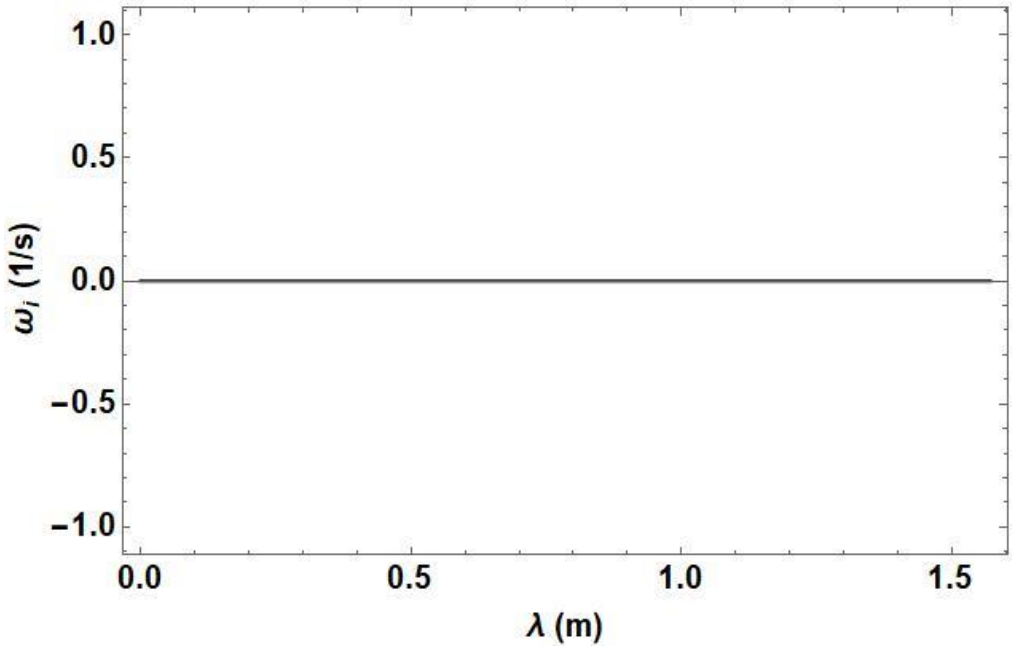

Figure 25: Dispersion relation for Wallis's slug flow model

The dispersion relation shown in Fig. 25 agrees with the stable parabolic nature of the variational fixed flux TFM obtained from the characteristic analysis for Wallis's slug flow model.

3.6 Interfacial Drag

The importance of the interfacial drag force for modeling the development of Taylor bubbles is discussed here. The variational Shallow Water TFM requires the constitutive models for the non-conservative (dissipative) interfacial drag force in addition to the conservative inertial forces. To model the clustering of local interfacial structures, the interfacial drag force needs to account for the acceleration of the dispersed bubbles based on the local void fraction and not on average void fraction. Hence, a localized drag coefficient has been used as opposed to using an averaged drag coefficient of Ishii and Chawla [42] for slug flow, which is based on average void fraction and is given by,

$$\langle c_D \rangle = 9.8\,(1-\alpha_2)^3 \tag{182}$$

The local drag coefficient c_D has been obtained from the experimental data of Cheng and Azzopardi [2] and Song et al. [3] using force balance between interfacial drag and gravity as displayed in Fig. 26.

$$c_D = e^{\left(1.3 + 9\alpha_2 - 44.4{\alpha_2}^2 + 45{\alpha_2}^3 - 13.5{\alpha_2}^4\right)} \tag{183}$$

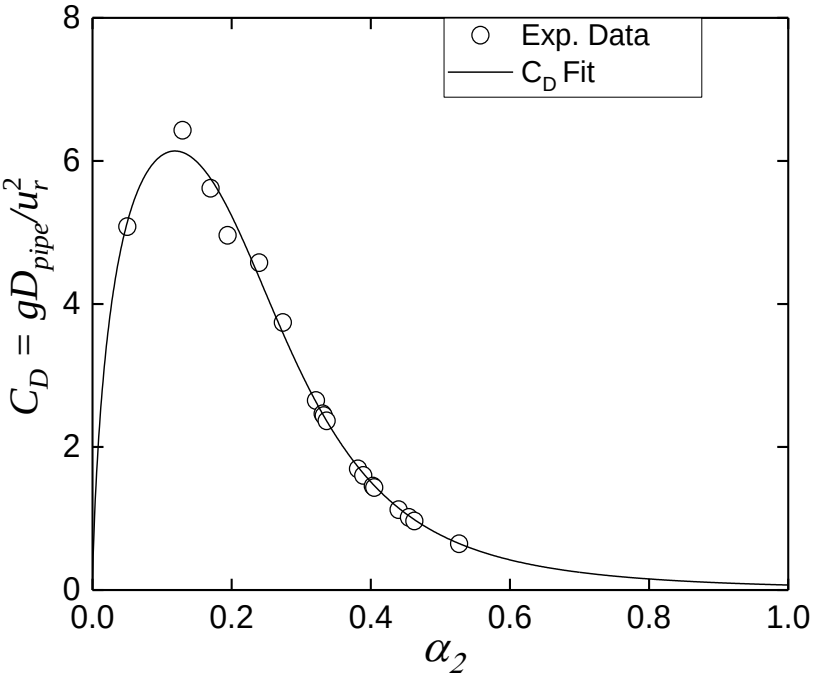

Figure 26: Local interfacial drag coefficient based on experimental data

In order to check if the localized c_D in Eq. (183) matches in an averaged sense with the average drag coefficient $\langle c_D \rangle$ in Eq. (182) for slug flow, the Eulerian time averaging procedure was used as shown below, to calculate $\langle c_D \rangle$ and $\langle \alpha_2 \rangle$ from the numerical simulation data for slug flows,

$$\langle c_D \rangle = \frac{\int_t^{t+\Delta t} c_D \, dt}{\Delta t} = \frac{\int_t^{t+\Delta t} \left(\frac{g D_{pipe}}{u_r^2}\right) dt}{\Delta t} \tag{184}$$

$$\langle \alpha_2 \rangle = \frac{\int_t^{t+\Delta t} \alpha_2 \, dt}{\Delta t} \tag{185}$$

The simulation data from the last 500 seconds of a 1000 seconds simulation at 0.5 m from the inlet of a 1 m long domain with periodic boundary conditions was used to calculate $\langle c_D \rangle$ and $\langle \alpha_2 \rangle$. The calculated $\langle c_D \rangle$ is compared with Ishii and Hibiki [17] as seen in Fig. 27. It can be seen that the average of the local drag coefficient falls in 90% agreement for $0.2 \leq \alpha_2 \leq 0.5$ range, which corresponds to the slug flow regime.

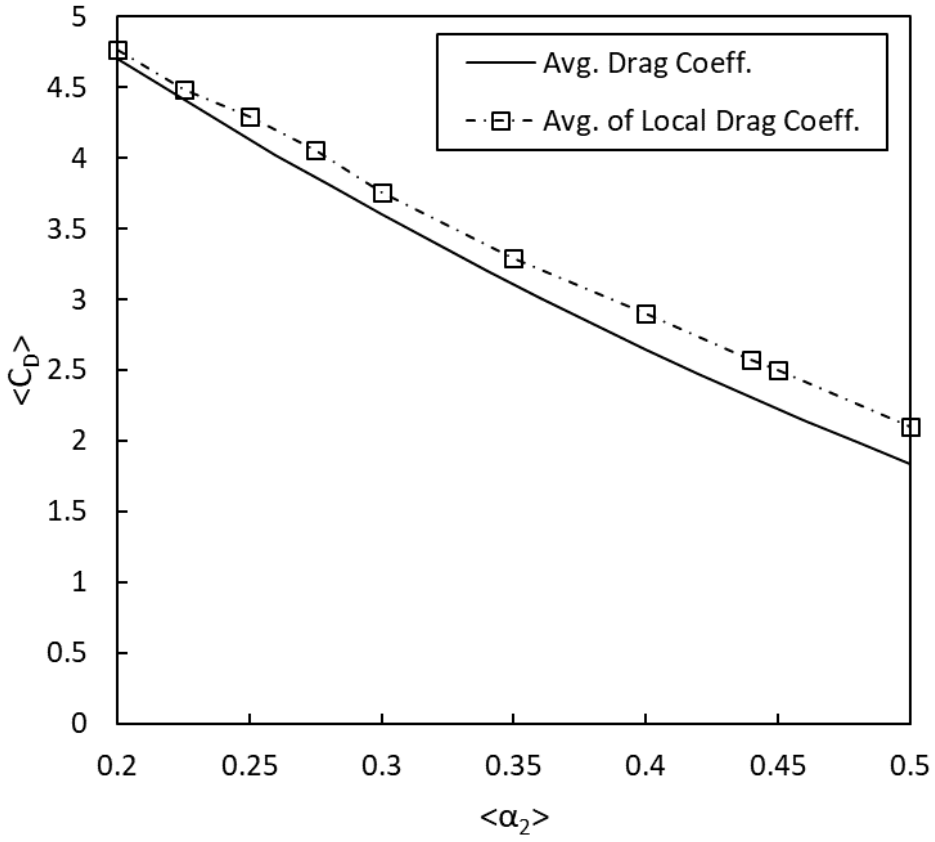

Figure 27: Comparison of the averaged interfacial drag coefficients

The use of localized drag coefficient induces SWT instability and the vortex model eliminates the KH instability as seen from dispersion relation in Fig. 28 for $X_0 = 4, b_w = 0.1$ and $\alpha_s = 0.92$. The model is stable for void fraction values of $\alpha_2 = 0.2$ and 0.7 which correspond to the bubbly flow and churn-annular flow regimes respectively. But the model is unstable for the intermediate void fraction range which corresponds to the clustered bubbly and slug flow regimes.

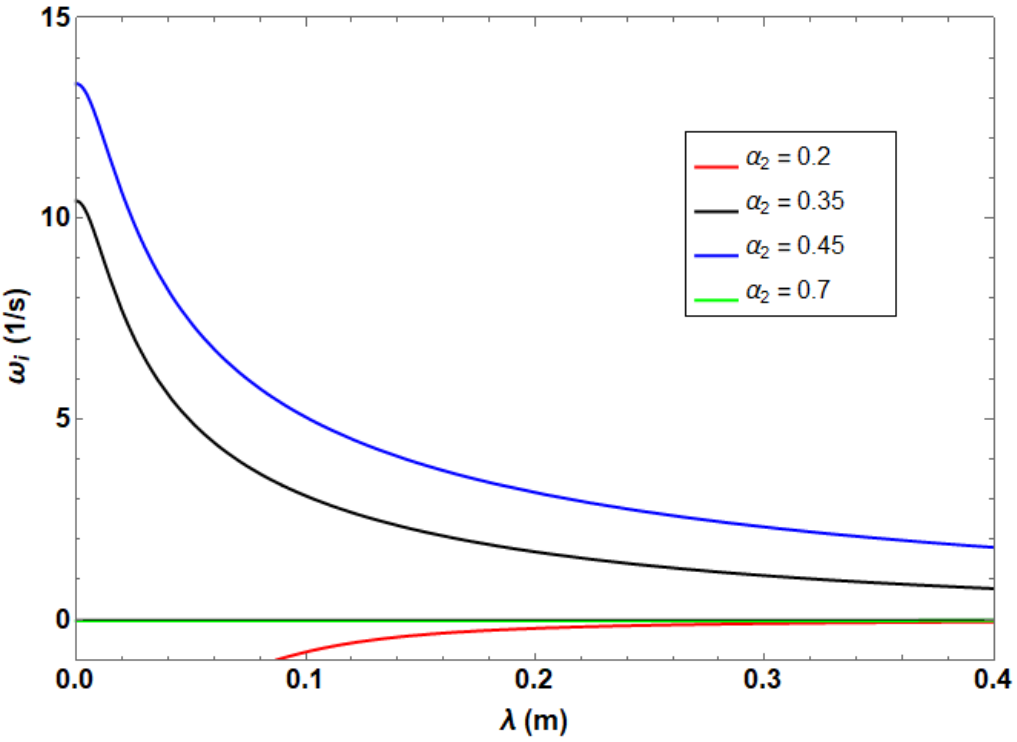

Figure 28: Dispersion relation for vortex model with local drag coefficient

The growth rate of the SWT instability in general is dependent on both the slope and magnitude of the interfacial drag coefficient and the same applies for making the 1D Shallow Water TFM unstable due to its resemblance to the 1D SWT equations. Using the fixed flux assumption $j_0 = 0$, the kinematic wave speed V_w following Whitham [8] and Wallis [9] is,

$$V_w = -\frac{F_{\alpha_2}}{\Gamma F_{\tilde{u}}} \tag{186}$$

The dispersion relation can then be written in terms of V_w as,

$$\omega_{1,2}(k) = -\frac{k\tilde{U}\Gamma'}{\Gamma^2} - \frac{iF_{\tilde{u}}}{2} \pm \sqrt{\left(i\frac{1}{2}F_{\tilde{u}} + \hat{c}k\right)^2 + ikF_{\tilde{u}}(V_w - C)} \tag{187}$$

where the dynamic wave speed C is,

$$C = \frac{\tilde{U}\Gamma'}{\Gamma^2}\left(-1 \pm \sqrt{\frac{2\Gamma'^2 - \Gamma\Gamma''}{2\Gamma'^2}}\right) \tag{188}$$

The kinematic stability criterion is then $V_w = C$, which can be simplified as,

$$\left(\frac{2\,\Gamma'}{\Gamma}+\frac{2-4\alpha_2}{\alpha_2\,(1-\alpha_2)}\right)-\frac{\sqrt{4\,\Gamma'^2-2\Gamma\Gamma''}}{\Gamma}=\frac{C_D{}'}{C_D} \tag{189}$$

The roots of the Eq. (189) for $0 \leq \alpha_2 \leq 1$ are shown in Fig. 29 where the R. H. S of Eq. (189) is plotted against the L. H. S for both the averaged and local drag coefficients using $X_0 = 4$, $b_w = 0.1$ and $\alpha_s = 0.92$. The stability map obtained from the dispersion relation is also shown in Fig. 30 to better visualize the SWT instability and the effect of using a localized drag coefficient. The stability map was obtained by taking the average of the dispersion relation at every 5 cm wavelength for $0 \leq \lambda \leq 1$. The roots of Eq. (189), where the curves intersect for the local drag coefficient define the upper and lower void fractions limits for the unstable region ($\omega_i > 0$) in Fig. 30. The model is unstable when L. H. S $>$ R. H. S of Eq. (189), which is equivalent to $V_w > \hat{c}$, as it is for the local drag coefficient. But the averaged drag coefficient of Ishii and Chawla [42] gives a stable model since L. H. S $<$ R. H. S as seen in Fig. 29, and has a stabilizing effect as opposed to the destabilizing effect of the local drag coefficient. Furthermore, the lower and the upper limits of α_2 for the unstable region in the stability map should define the lower bound and upper bound for the slug flow waves in the numerical simulations. It can be stated that the interfacial drag force with localized drag coefficient makes the variational 1D Shallow Water TFM model unstable while the model is unconditionally hyperbolic and well-posed. The drag force causes the void fraction waves to grow or decay. The amplitude of the fully developed slug flow waves should to some extent be determined by these limits and it would not be unreasonable to state that without the upper limit for α_2, the waves will continue to grow without any constraint. Hence it will limit the size of the Taylor bubbles in terms of local void fraction values. Moreover, the growth rate and non-linear evolution of the shape of the slug flow waves is dependent on the localized drag coefficient in conjunction with the $m(\alpha_2)$ from the vortex model used for the conservative forces.

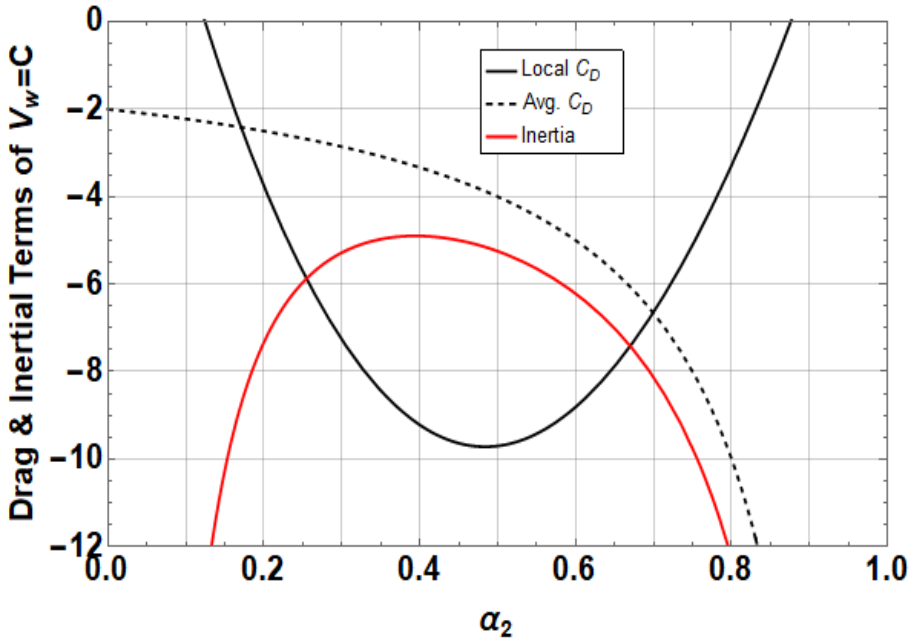

Figure 29: Effect of average and local interfacial drag on linear stability

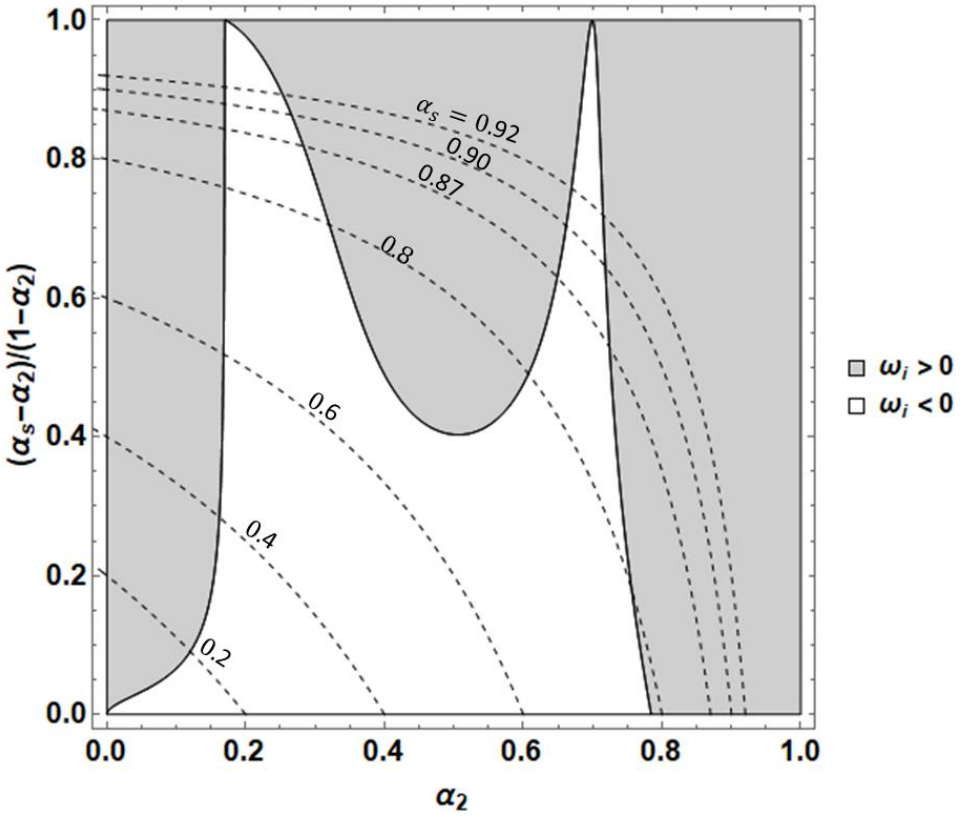

Figure 30: Linear stability map from dispersion relation

3.7 Numerical Simulations

3.7.1 Verification

Burgers Equation

For verification of the numerical simulations, the 1D variational Shallow Water TFM equations without the interfacial drag, gravity, and surface tension for the Γ from Wallis slug flow model are analyzed here. The Eq. (101)-(102) are written in terms of α_2, $\widetilde{U}$ and Γ as,

$$\frac{\partial \alpha_2}{\partial t} + \frac{\partial}{\partial x}\left(\frac{\widetilde{U}}{\Gamma}\right) = 0 \tag{190}$$

$$\frac{\partial \widetilde{U}}{\partial t} - \frac{\partial}{\partial x}\left(\frac{\Gamma' \widetilde{U}^2}{2\,\Gamma^2}\right) = 0 \tag{191}$$

By introducing $r_p = \rho_2/\rho_1 \ll 1$ for air-water two phase mixture in the definition of Γ,

$$\Gamma = \frac{1}{1-\alpha_2} + \frac{r}{\alpha_2} + \frac{(\alpha_s - \alpha_2)}{\alpha_2\,(1-\alpha_2)\,(1-\alpha_s)} = \left(\frac{\alpha_s}{1-\alpha_s}\right)\frac{1}{\alpha_2} \tag{192}$$

$$\Gamma' = -\left(\frac{\alpha_s}{1-\alpha_s}\right)\frac{1}{{\alpha_2}^2} \tag{193}$$

Using Eq. (193), the set of equations in Eqs. (190)-(191) can be simplified as,

$$\frac{\partial \alpha_2}{\partial t} + \frac{\partial \alpha_2 \widetilde{U}^*}{\partial x^+} = 0 \tag{194}$$

$$\frac{\partial \widetilde{U}}{\partial t} + \widetilde{U}^* \frac{\partial \widetilde{U}^*}{\partial x^+} = 0 \tag{195}$$

where $x^+ = (1-\alpha_s)x/\alpha_s$. We can see that the slug flow model of Wallis for negligible r_p simplifies the momentum equation of the 1D variational Shallow Water TFM equations into a Burgers equation as shown in Eq. (195). Furthermore, Eq. (195) is decoupled from the continuity equation given in Eq. (194). The importance of solving the Burgers equation for verification lies in the fact that it has the well-known analytical solution obtained by method of characteristics. Therefore, these equations are used next to verify the TFM for a piecewise linear initial condition. For a piecewise initial condition of the form,

$$\widetilde{U}^*(x^*(0),0) = \widetilde{U}_0{}^* = \tilde{a} + \tilde{b}\,x^+$$

$$\tilde{a} = 2.03$$

$$\tilde{b} = \begin{cases} 0.2x^+, & for\ x^+ \le 0.1 \\ -0.02\big(1 - 10(x^+ - 0.1)\big), & for\ 0.1 \le x^+ \le 0.2 \\ 0, & for\ x^+ \ge 0.2 \end{cases} \tag{196}$$

the analytical solution from the method characteristics is,

$$\widetilde{U}^*(x^*,t) = \frac{\tilde{a} + \tilde{b}x^+}{1 + \tilde{b}\,t} \tag{197}$$

Given in Fig. 31 is the comparison of the simulation results for different mesh sizes with the analytical solution, where a piecewise initial condition is used for $\widetilde{U}^*$. The simulations were run using a 1 m long domain with periodic boundary conditions for 2 seconds.

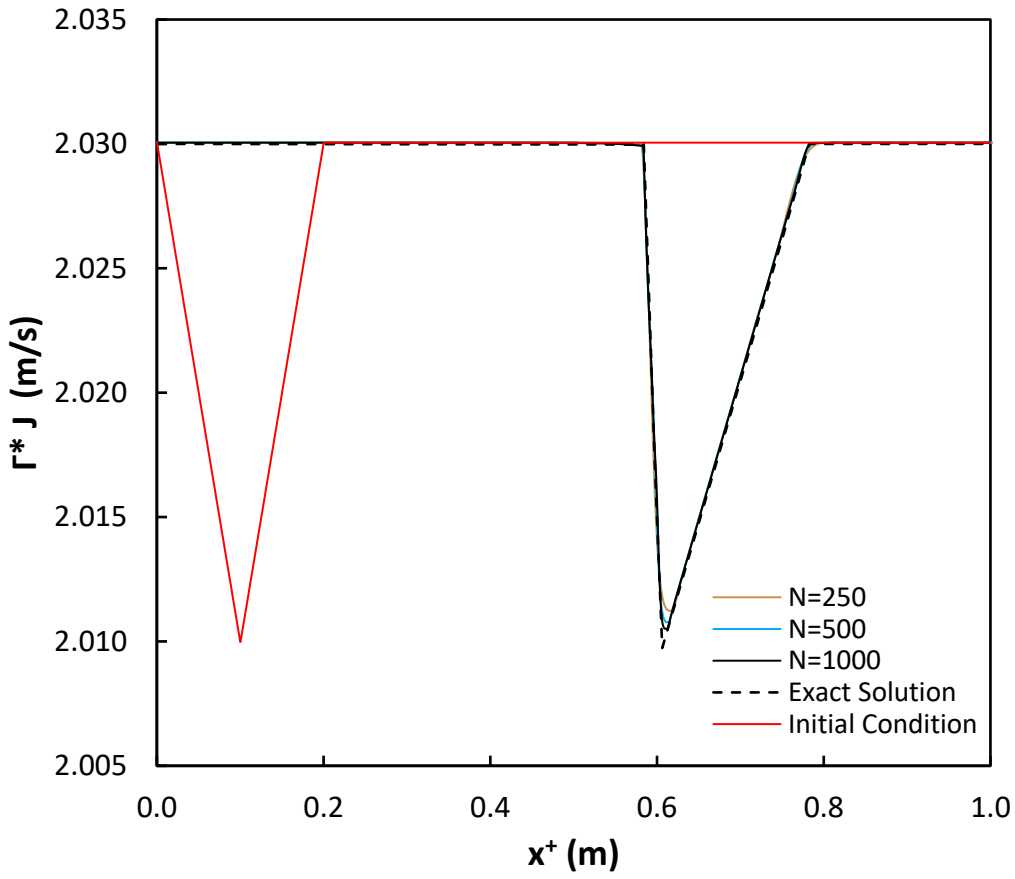

Figure 31: Comparison of Burgers equation simulations with the analytical solution

Void Propagation Equation

Once the solution of the momentum equations is verified, the next step is the solution of the continuity equation when coupled with the momentum equation of the variational Shallow Water TFM. A piecewise initial condition is used for α_2 as,

$$\alpha_2(\,x^+(0),0) = \alpha_{2_0} = \tilde{p} + \tilde{q}\,x^+$$

$$\tilde{p} = 0.5$$

$$\tilde{q} = \begin{cases} 0.05\,x^+, & for\ \ x^+ \le 0.1 \\ -0.05\big(1 - 10(\,x^+ - 0.1)\big), & for\ 0.1 \le\ x^+ \le 0.2 \\ 0, & for\ \ x^+ \ge 0.2 \end{cases} \tag{198}$$

The same initial condition as in the Burgers equation solution is used for $\widetilde{U}^*$. For $\widetilde{U}^*(x^+,t)$ given by Eq. (197), the solution for the continuity equation is,

$$\alpha_2(x^+,t) = \frac{\tilde{p} + \tilde{q}x^+ + \big(\tilde{b}\,t - \tilde{a}\,\tilde{q}\big)t}{(1+\tilde{b}\,t)^2} \tag{199}$$

Given in Fig. 32 is the comparison of the simulation results for different mesh sizes with the analytical solution for $\alpha_2(x^+,t)$.

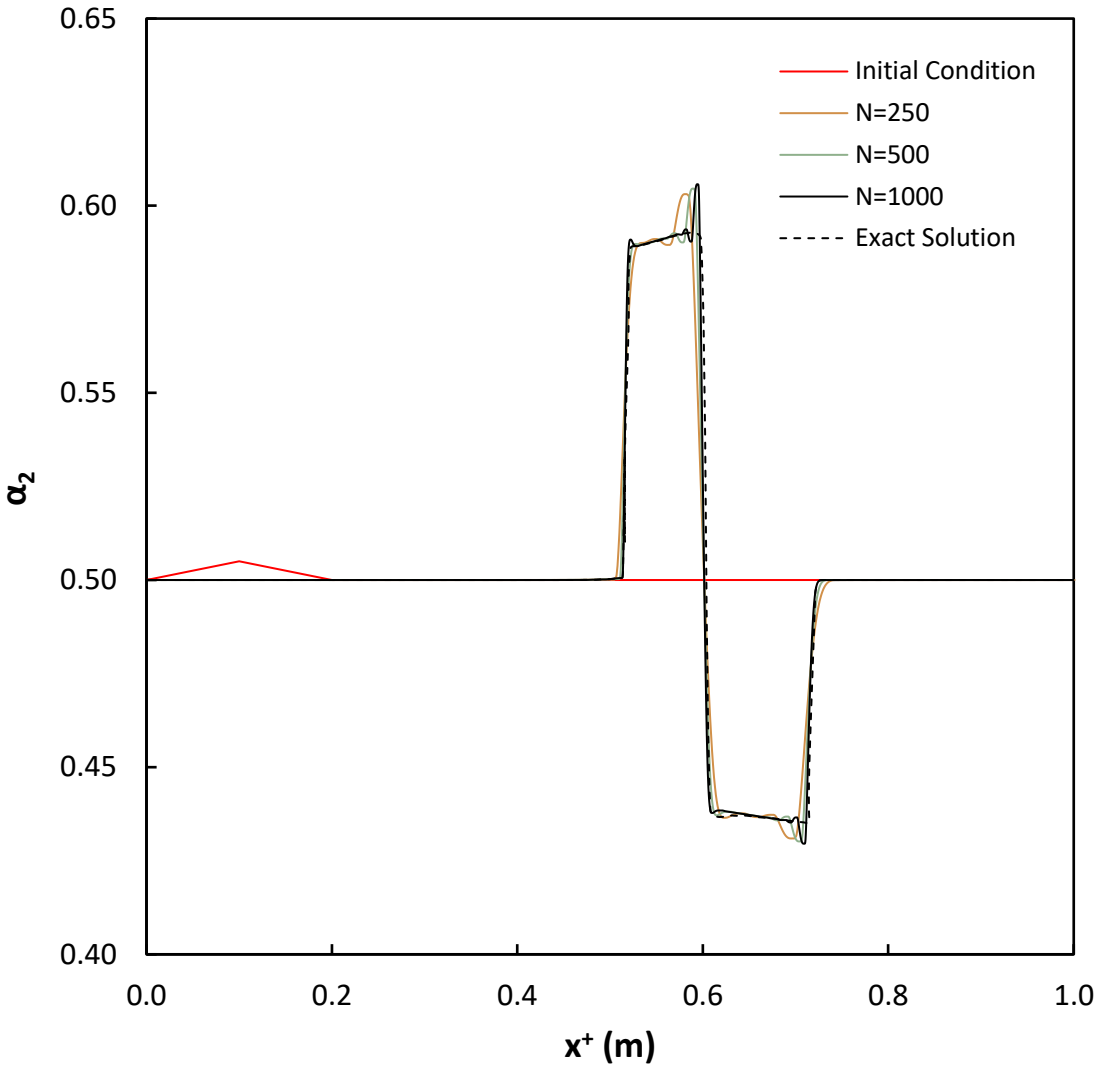

Figure 32: Comparison of void propagation solution with the analytical solution

Wave Propagation

The kinematically stable Wallis model with interfacial drag is used for verification here. The 1D Shallow Water TFM equations in Eq. (101)-(102) without the surface tension term are solved for the drag coefficient,

$$c_D = \frac{1-\alpha_2}{\alpha_2} \tag{200}$$

This C_D gives a stable Wallis model according to the dispersion relation in Fig. 33 for $\alpha_2 = 0.5$.

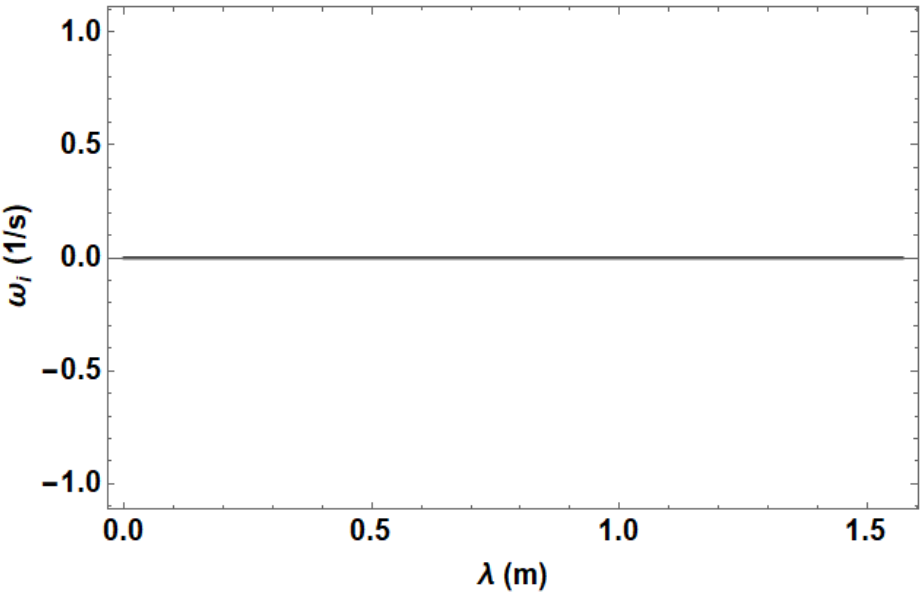

Figure 33 : Dispersion relation for kinematically stable Wallis model with simplified drag

This stable SWT wave propagation problem was solved numerically, and the simulation result for different mesh sizes is shown in Fig. 34 for the piecewise initial condition for α_2 and with $\Gamma^* J$= constant. It can be seen that a converged solution can be obtained as the number of nodes is increased.

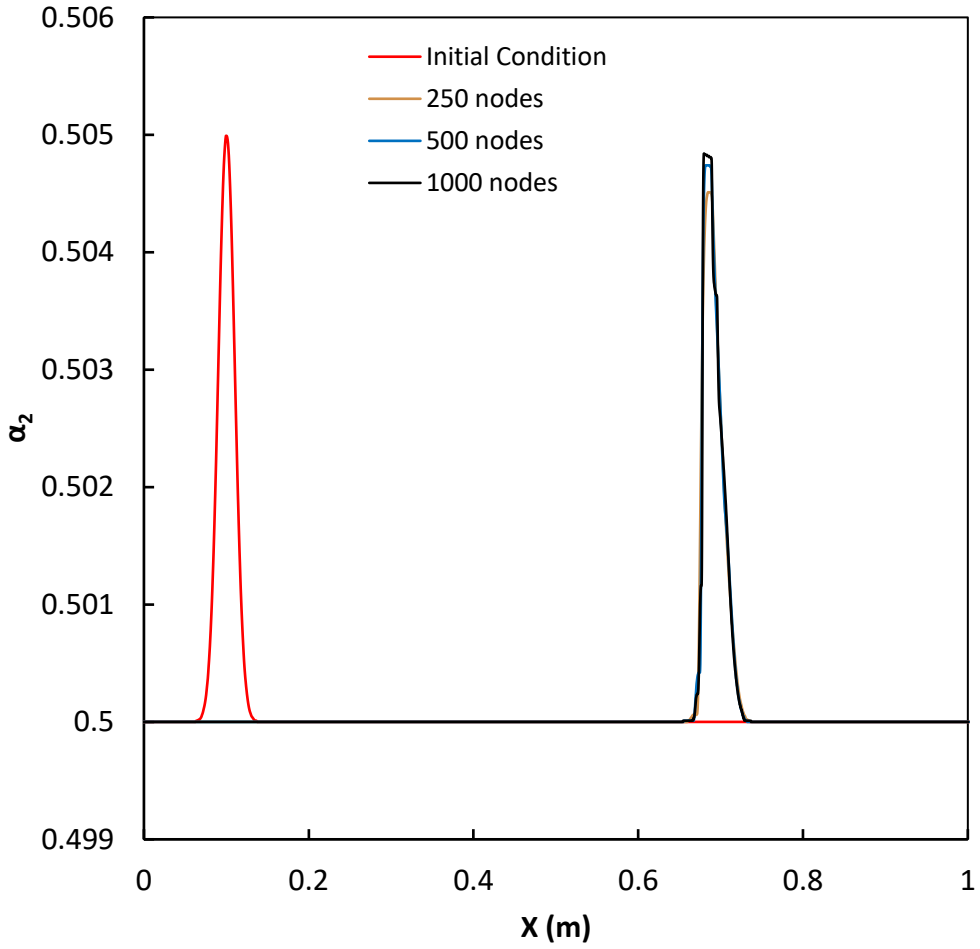

Figure 34: Simulation of stable wave propagation for Wallis model with simplified drag

3.7.2 Validation

The 1D variational Shallow Water TFM with the confined vortex model was used to perform numerical simulations for dispersed bubbly, clustered bubbly and slug flow regimes. The validation of the simulation results with the experimental data of Cheng and Azzopardi [2] and Song et al. [3] is discussed here. For the non-linear simulation results presented here, a mesh size $\Delta x = 1$ mm for the 1D spatial domain of length 1 m and the time step Δt, defined based on $\Delta t/\Delta x = 0.25$ s/m were used. The non-dimensional inertia Γ^* without using the simplification of $r_p = \rho_2/\rho_1 \ll 1$, the gas void fraction α_2 and $\widetilde{U}^* = \Gamma^* \mathrm{J}$ were calculated. The numerical simulations were run using periodic boundary conditions. The initial condition of α_2 and $\widetilde{U}^*$consisted of a sinusoidal perturbation with amplitude and wavelength of the order of 10^{-3} and 1 m respectively. Since the simulations were performed using equations for a frame moving with

constant j, the α_2 and $\widetilde{U}^*$ were obtained in the lab frame by translating the position of the probe accordingly. For this, the position of the probe in the moving j frame is first calculated using the MOD functionality in FORTRAN. Then the node to the left of the probe and the corresponding position are determined. This is followed by the calculation of α_2 and $\widetilde{U}^*$, by taking their position weighted average using node to the left of the probe as reference. Based on the parametric study discussed in Appendix 6.4, the vortex model with $X_0 = 4$, $b_w = 0.1$ and $\alpha_s = 0.92$, and the drag coefficient C_D defined in Eq. (183) were used for validation of the numerical simulations.

Slug Flow

Table 3 summarizes the air-water two-phase flow conditions from the experimental data of Cheng and Azzopardi [2] and Song et al. [3], used for validation of the slug flow simulation results.

Table 3: Flow conditions for numerical simulations of slug flow

Experiment	$L_{pipe}(m)$	$D_{pipe}(mm)$	$j_1\ (m/s)$	$j_2\ (m/s)$	α_2
Cheng and Azzopardi [2]	4.1	28.9	0.356	0.5033	0.463
Cheng and Azzopardi [2]	4.1	28.9	0.356	0.767	0.527
Song et al. [3]	3	25	0.275	0.364	0.405
Song et al. [3]	3	25	0.275	0.392	0.44

Fig. 35 and Fig. 36 show the temporal evolution of α_2 for the slug flow data of Cheng and Azzopardi [2] for mean gas void fraction of $\alpha_2 = 0.527$ and 0.463 respectively. The $\alpha_2(t)$ values were obtained at 0.5 m from the inlet of a 1 m periodic domain.

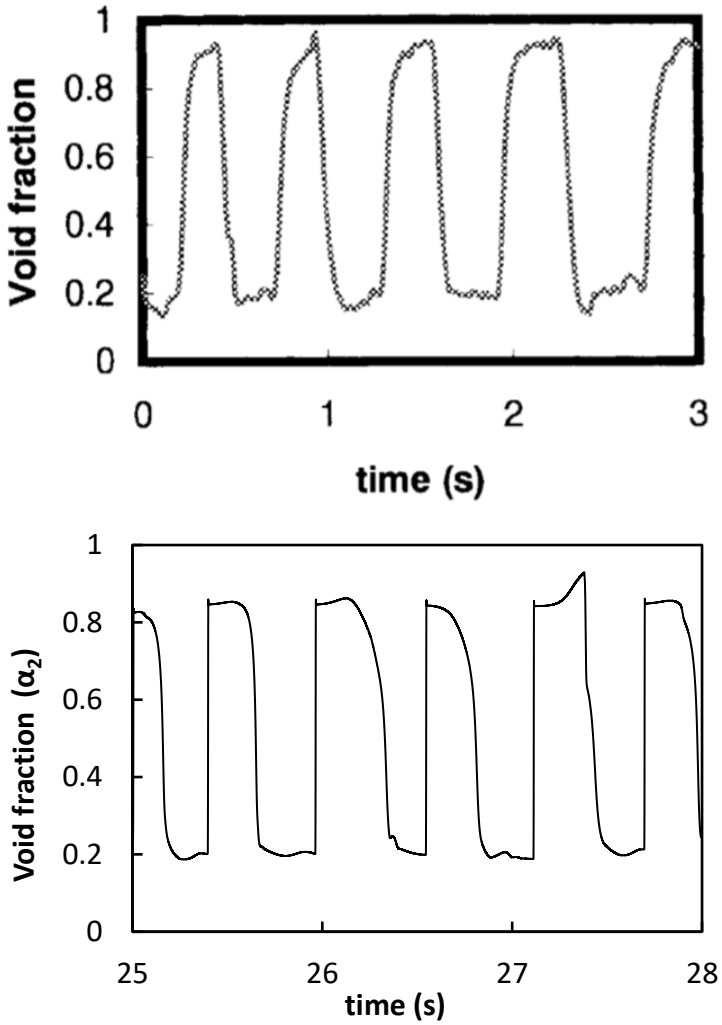

Figure 35: Comparison of simulation with data of Cheng and Azzopardi [2]

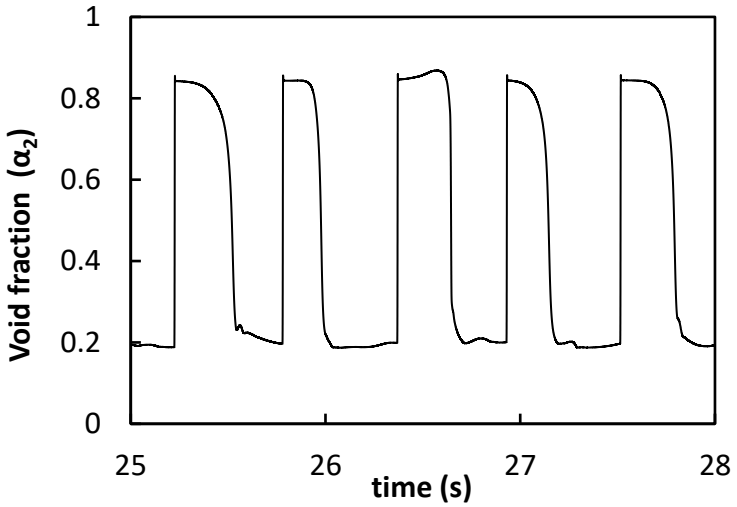

Figure 36: Numerical simulation result for Cheng and Azzopardi [2] data

The amplitude and frequency (number of pulses per second) of the slug flow waves from the data and simulations are compared below in Table 4 for $\alpha_2 = 0.527$and the error is less than 12%.

Table 4 : Comparison of simulation results with the data of Cheng and Azzopardi [2]

	Data	Simulation	Error (%)
Amplitude	0.7	0.65	7.1
Frequency (1/s)	1.5	1.67	11.3

Figs. 37-38 and Figs. 39-40 show the comparison of the numerical simulations with the experimental data of Song et al. [3], for mean gas void fraction of $\alpha_2 = 0.405$ and 0.44 respectively.

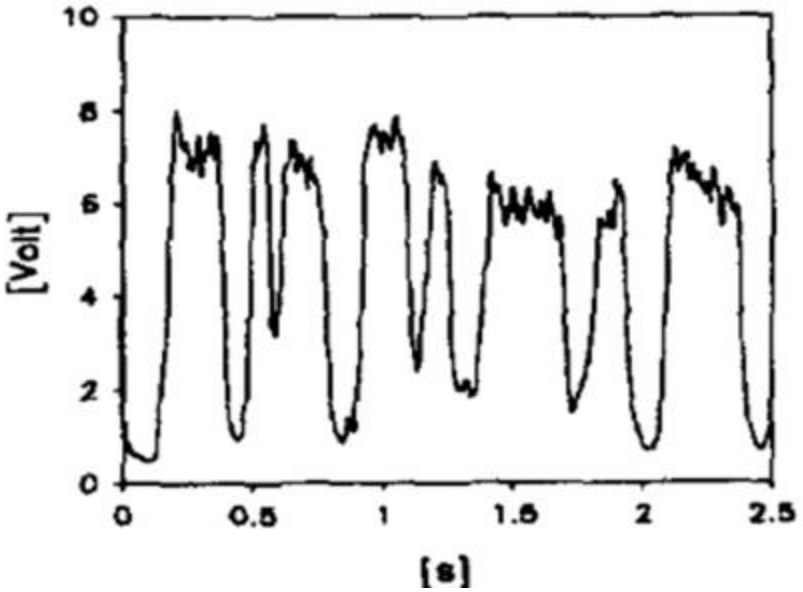

Figure 37: Voltage signal from Song et al. [3]

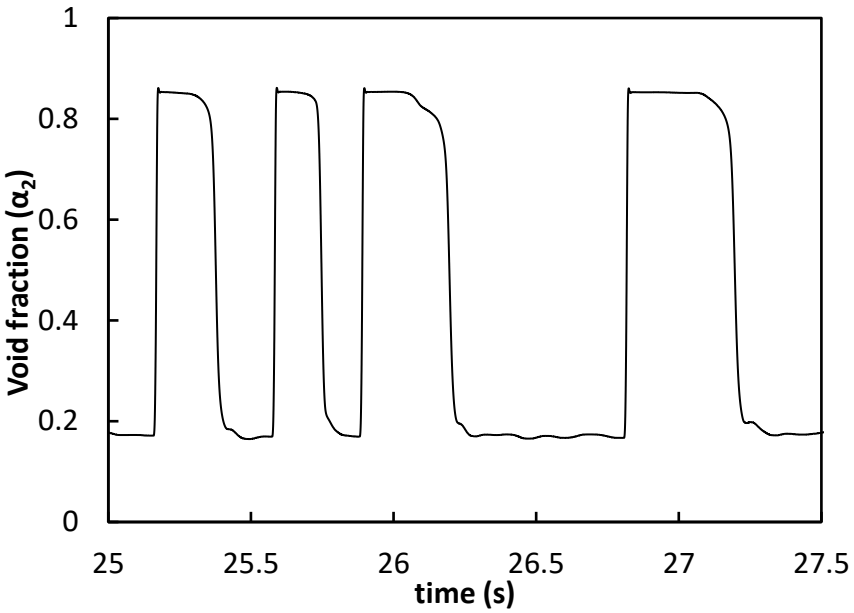

Figure 38: Numerical simulation result for the data of Song et al. [3]

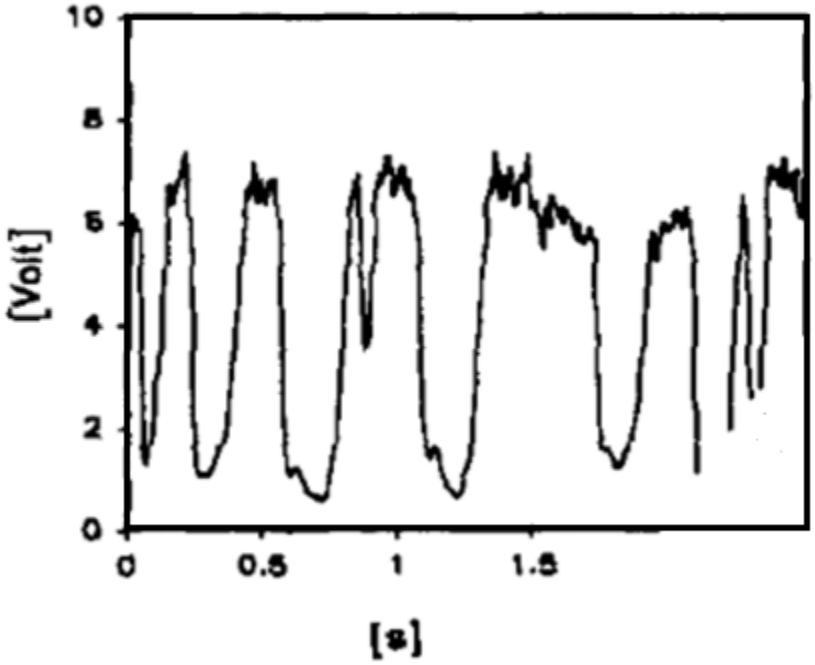

Figure 39: Voltage signal from Song et. al. [3]

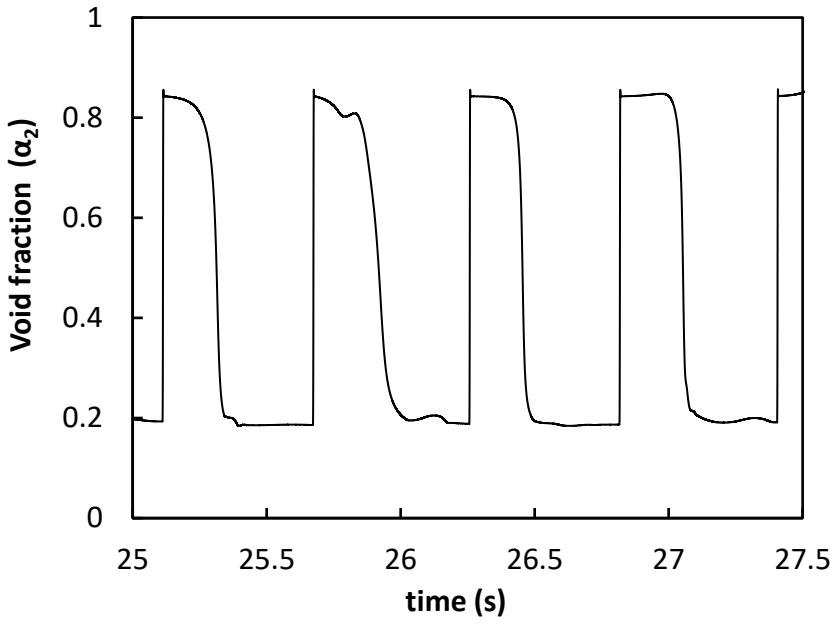

Figure 40: Numerical simulation result for the data of Song et al. [3]

The wave propagation properties are compared using the frequency and width of the slug flow pulses for the data of Song et al. [3] in Table 5 and agreement is within 41%. In addition, the wave propagation speeds from simulations are compared with the data in Table 4 and the agreement is within 15%.

Table 5: Comparison of numerical simulations with data of Song et al. [3]

α_2	Frequency (1/s)			Width (s)		
	Data	Simulation	Error (%)	Data	Simulation	Error (%)
0.405	2.7	1.6	40.7	0.3	0.325	8.3
0.44	2.4	1.8	25.0	0.35	0.3	14.3

Table 6: Comparison of wave propagation speeds for data of Song et al. [3]

α_2	Wave Propagation Speed C_w (m/s)		
	Data	Simulation	Error (%)
0.405	0.88	0.75	14.8
0.44	0.88	0.78	11.4

It can be seen that there is some discrepancy when the void fraction wave propagation properties from simulation are compared with that of the data. The discrepancy can be attributed to the lack of information regarding axial wake profiles for different average void fractions for slug flows

used to obtain the b_w and X_0 values chosen for the numerical calculation. To analyze the non-linear dynamics associated with the slug flow material waves, the two-dimensional (2D) phase space plot of $\widetilde{U}^* = \Gamma^* J$ and α_2 is used. The simulations were run for 5000 seconds and the trajectories of $\widetilde{U}^*$ and α_2 are shown in Figs. 41, 42 and 43 for mean gas void fraction of 0.405, 0.44 and 0.527, using the last 500 seconds of simulation data. It can be seen that though the trajectories seem chaotic as they cross each other as opposed to being well defined. But they are bounded and hence the model in Lyapunov stable since the growth of the void fraction waves is non-linearly bounded.

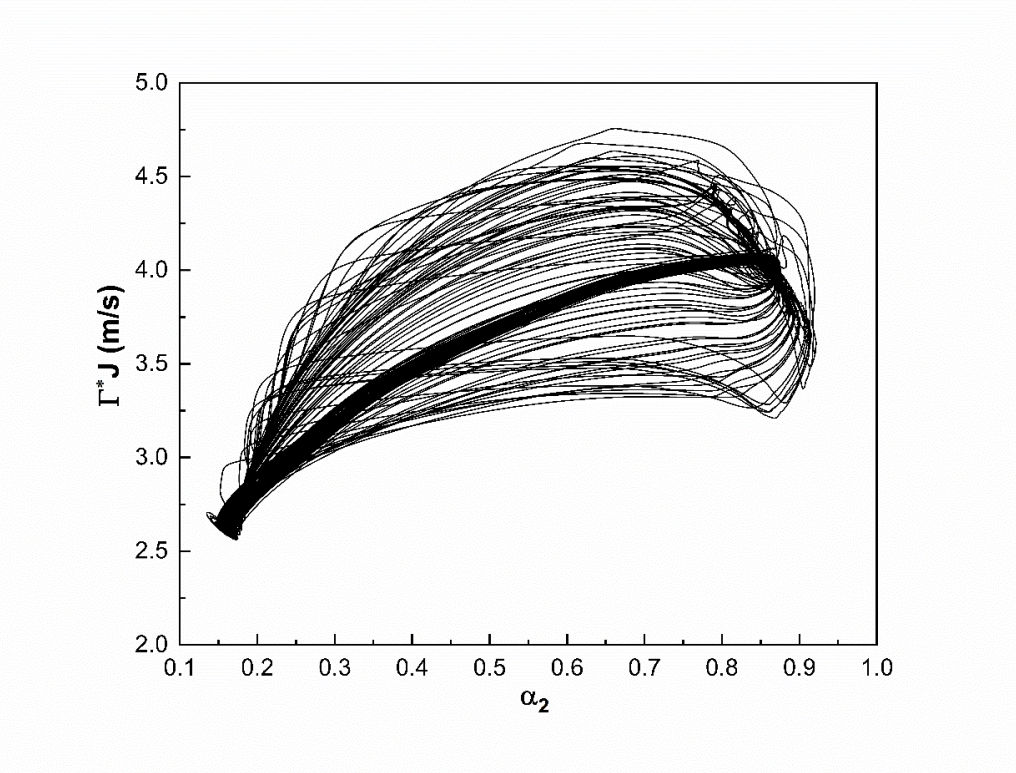

Figure 41: 2D Phase space plot for 40.5 % slug flow case of Song et al. [3]

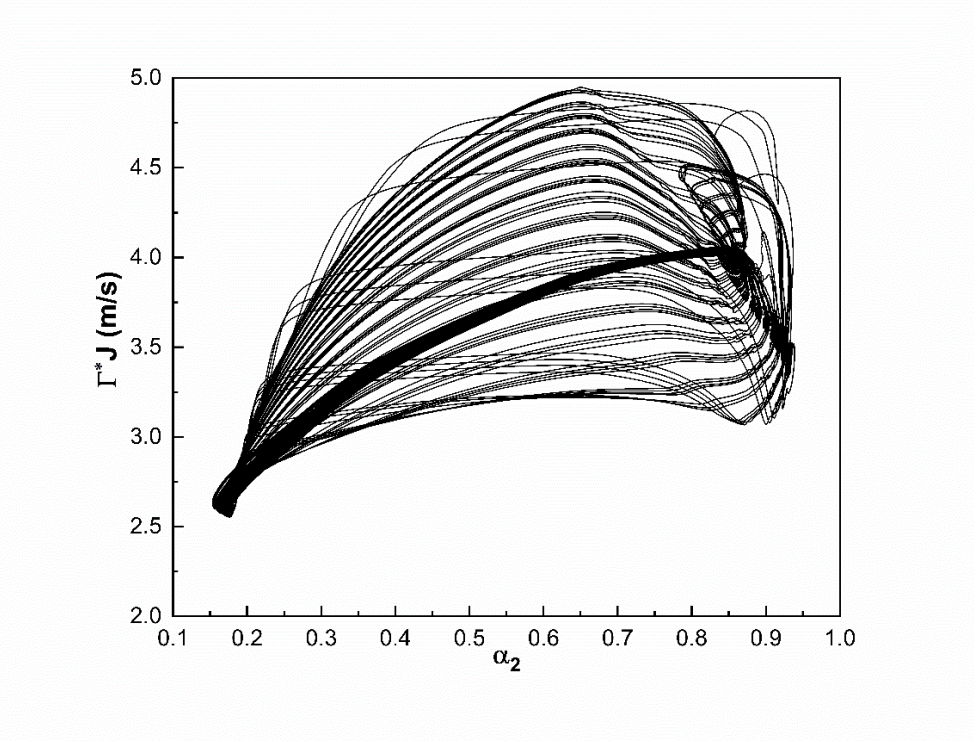

Figure 42: 2D Phase space plot for 46% slug flow case of Song et al. [3]

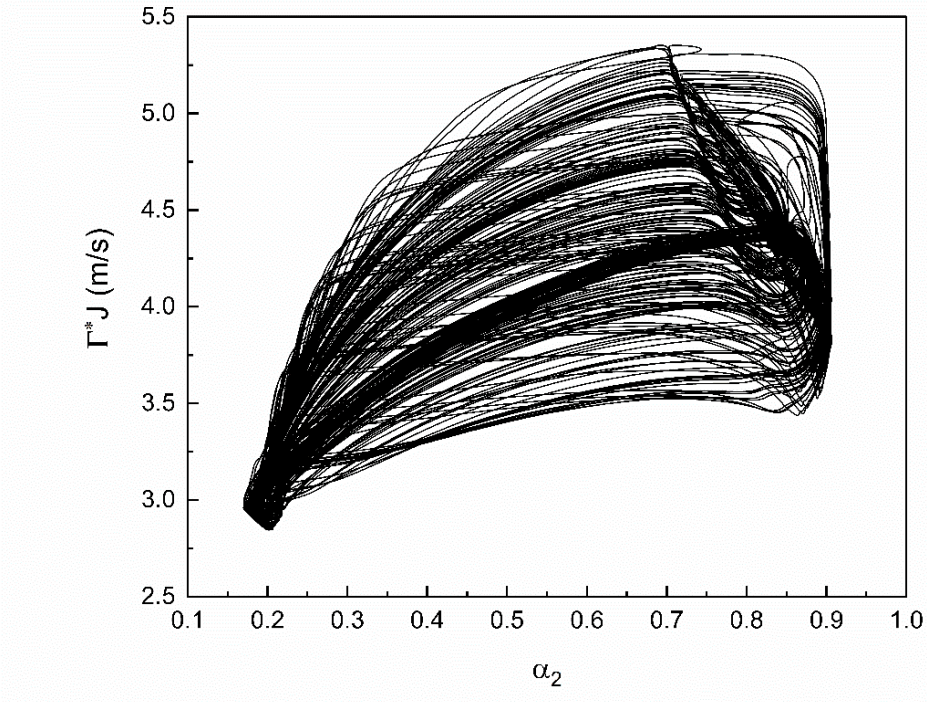

Figure 43: 2D Phase space plot for 52.7% slug flow case of Cheng and Azzopardi [2]

From the 2D phase space plots, the solutions look chaotic. For the grid convergence test, the temporal evolution of α_2 is visualized for different grid sizes are shown in Fig. 44.

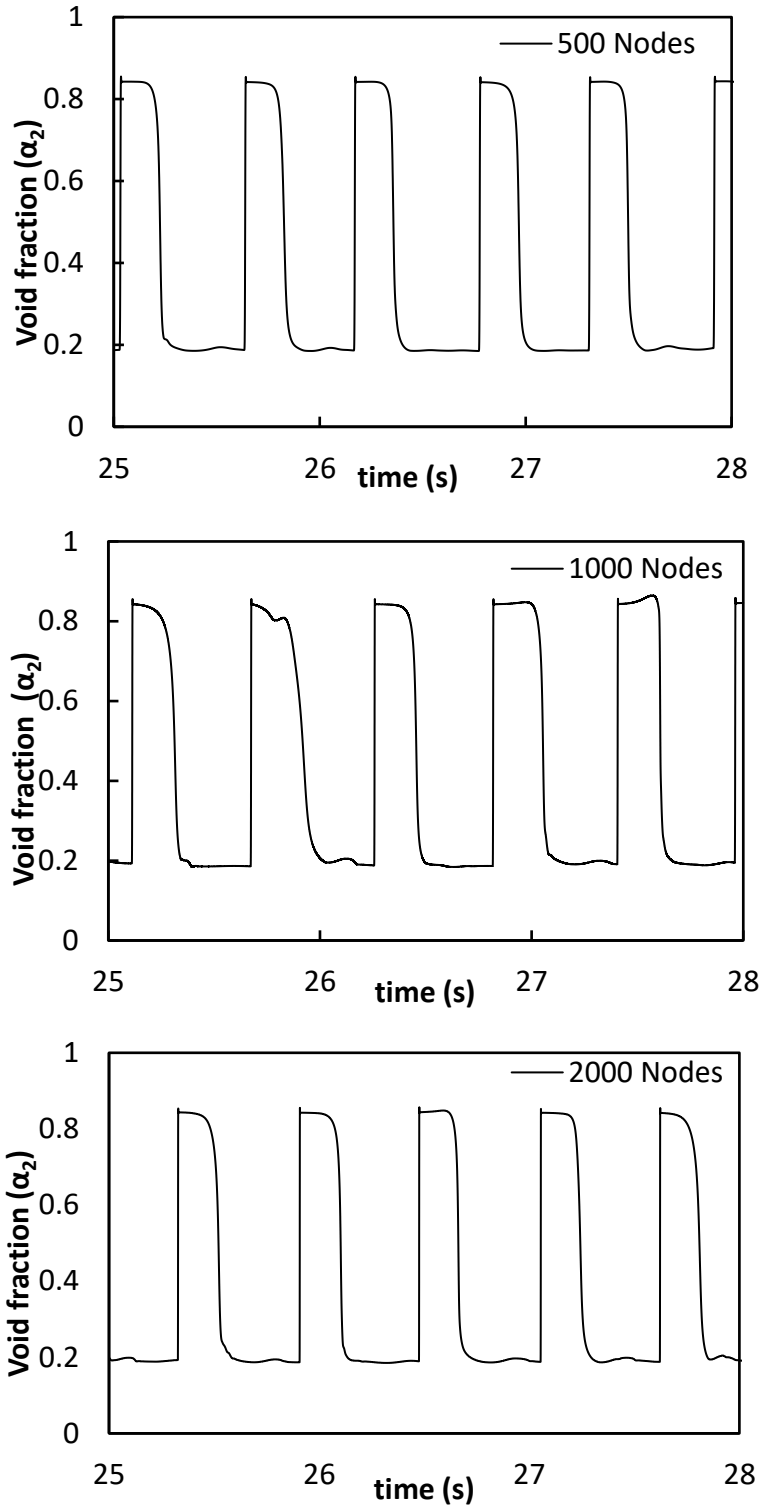

Figure 44: Slug flow at different mesh sizes for 52.7 % void fraction

To demonstrate chaos and grid convergence in the spectral sense, the amplitude spectra in the frequency domain of the interfacial structures is used. The simulations were run for 5000 seconds and the data from last 200 seconds were used. The data was collected at the center of the 1D domain and using the Fast Fourier Transform (FFT), the amplitude $|A\ (\alpha_2)|$ in the frequency domain is calculated as,

$$|A\ (\alpha_2)| = \frac{FFT(\alpha_2 - \langle\alpha_2\rangle)}{N/2} \tag{201}$$

where N is the number of nodes and $\langle\alpha_2\rangle$ is the mean gas void fraction. In the Fig. 45, it can be seen that the solution converges at 1000 nodes (1 mm mesh) and spectral convergence is obtained. Furthermore, the continuous distributions in the frequency domain demonstrate the chaotic nature of the interfacial structures for slug flow.

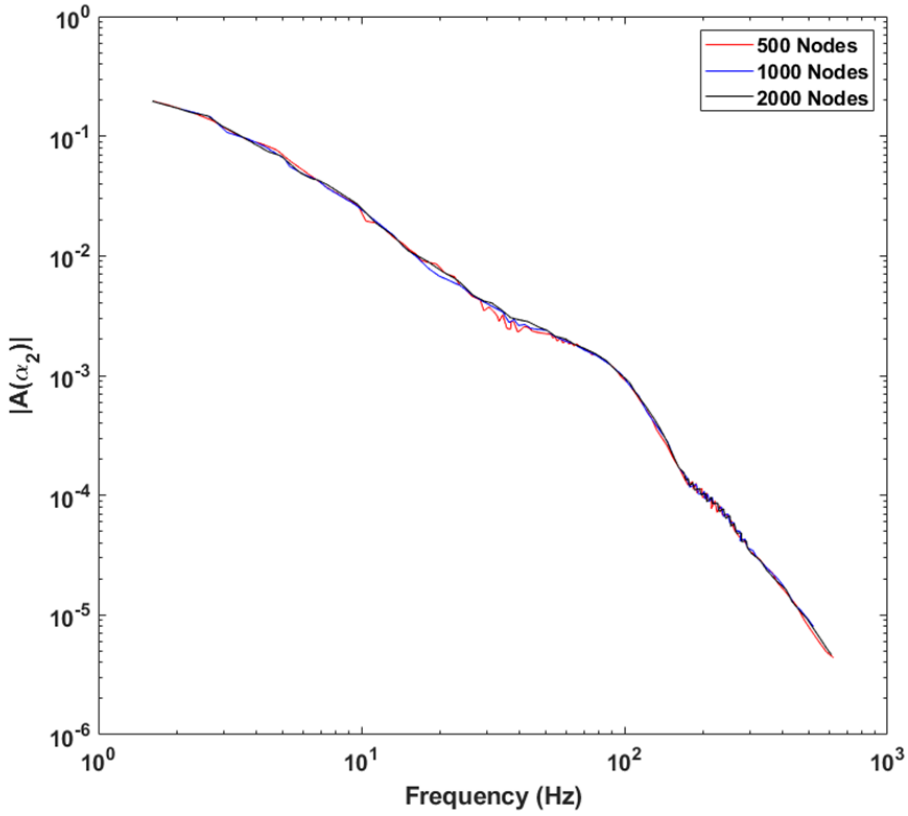

Figure 45: Slug flow amplitude spectra for 52.7 % void fraction

Clustered Bubbly Flow

In order to test the capability of the vortex model to resolve development of flow structures for clustered bubbly flows, the simulation results obtained for lower α_2 values in the range of $0.27 \geq \alpha_2 \leq 0.3$ are presented here. A typical time series plot of $\alpha_2 = 0.2$ from the clustered bubbly flow data of Cheng & Azzopardi [2] along with the simulation results for $\alpha_2 = 0.27$ and $\alpha_2 = 0.3$ are given in Fig. 46, Fig. 47 and Fig. 48 respectively.

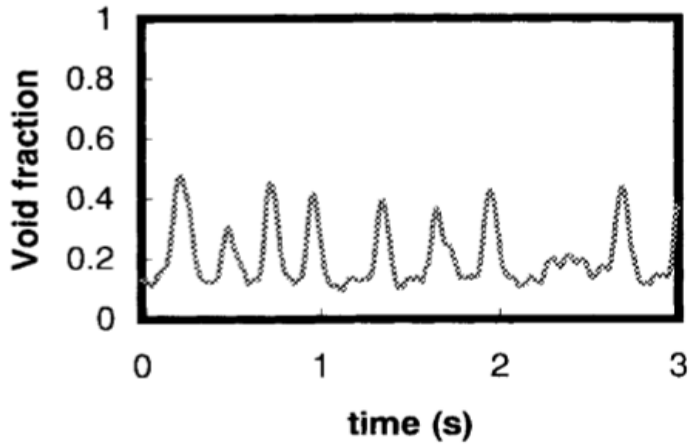

Figure 46: Clustered bubbly flow data of Cheng and Azzopardi [2]

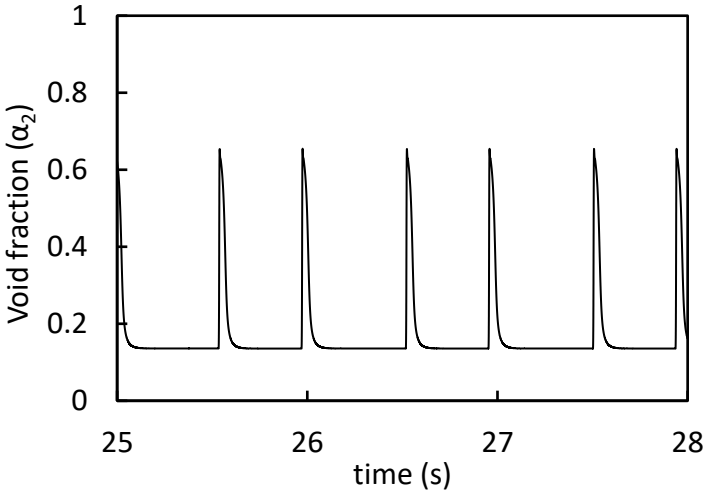

Figure 47: Clustered bubbly flow simulation for 27% void fraction

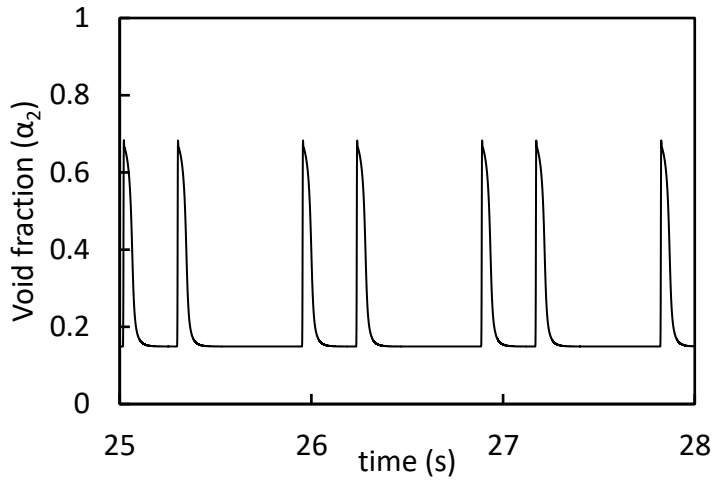

Figure 48: Clustered bubbly flow simulation for 30% void fraction

Similar to the slug flow simulations, the clustered bubbly flow simulations were run for 5000 seconds to visualize the 2D phase space trajectories for $\Gamma^* J$ as a function of α_2. From Fig. 49 and Fig. 50, the trajectories correspond to limit cycles as the trajectories are well defined and are not interwoven. Similar to slug flow regime, the model is found to be Lyapunov stable for clustered bubbly flow regime.

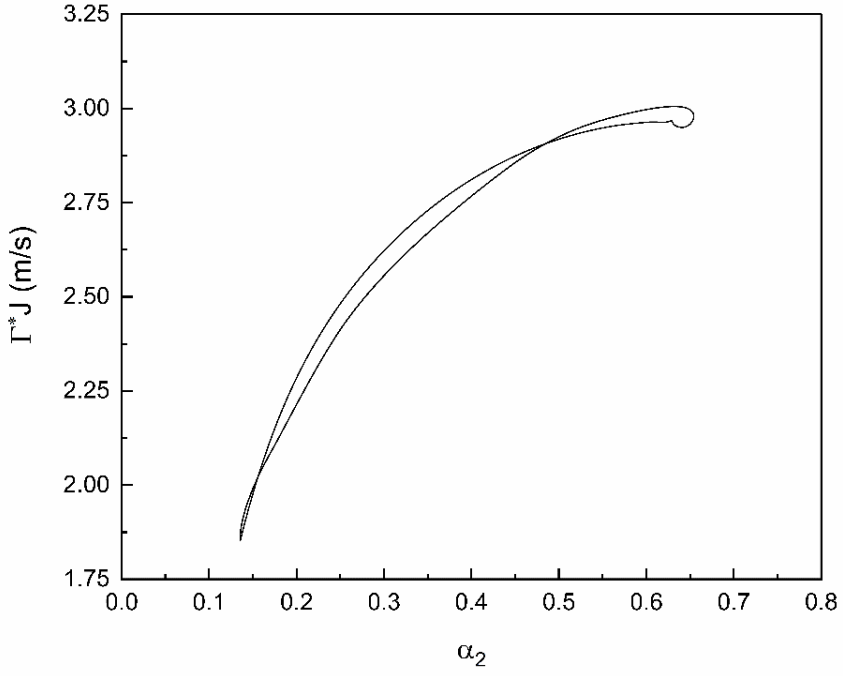

Figure 49: 2D phase space plot of clustered bubbly flow simulation at 27% void fraction

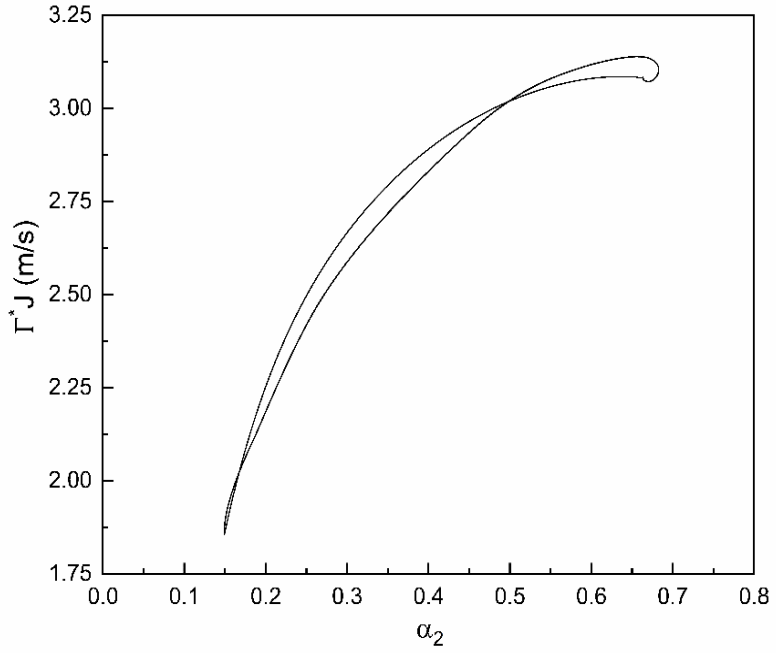

Figure 50: 2D phase space plot for clustered bubbly flow simulation at 30% void fraction

Performing the mesh refinement test further demonstrates the limit cycle (non-chaotic) behavior of the interfacial structures for bubble clusters as shown in Fig. 51, for mean gas void fraction of 27%. It can be seen that the solution converges at 1000 nodes or $\Delta x = 1$ mm.

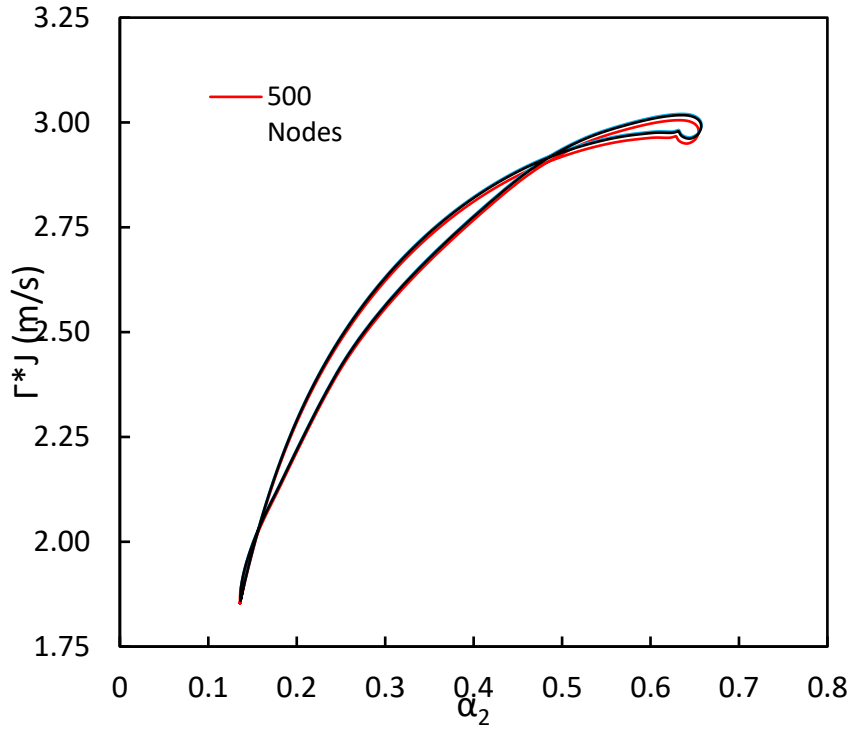

Figure 51: Grid convergence of 2D phase space plot for clustered bubbly flow simulation

Dispersed Bubbly Flow

The capability of the 1D Shallow Water TFM to simulate bubbly flow is tested here. Cheng and Azzopardi [2] report dispersed bubbly for lower value of $\alpha_2 = 0.13$ as shown in Fig 52. According to the stability map in Section 3.6, the model predicts stable dispersed bubbly flow in the range $0.15 \leq \alpha_2 \leq 0.26$ and the time series plot for $\alpha_2 = 0.15$ is given in Fig. 53. The perturbation present in the initial condition decays with time as the model is SWT stable as opposed to being unstable as is the case for clustered bubbly and slug flow regimes. But similar to the case of clustered bubbly flow regime, there is a discrepancy in the prediction capability of the model when it comes to stable dispersed bubbly flows. The model should have been stable for the lower void fractions where in general stable dispersed bubbly flow and this is due to high constant value of $\alpha_s = 0.92$ being used and for stable bubbly flow, the α_s should more or less follow $\alpha_s \cong \alpha_2$.

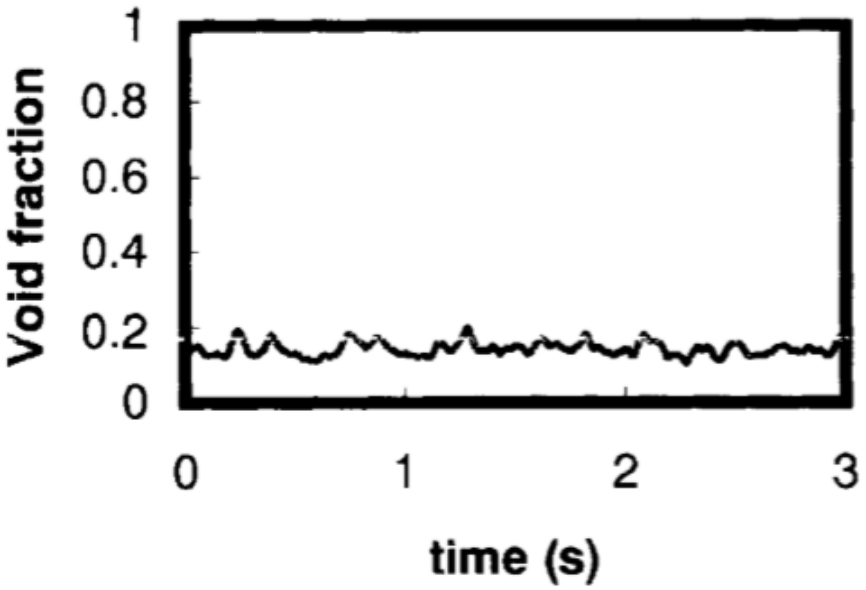

Figure 52 Time series plot of stable bubbly flow data from Cheng & Azzopardi [2]

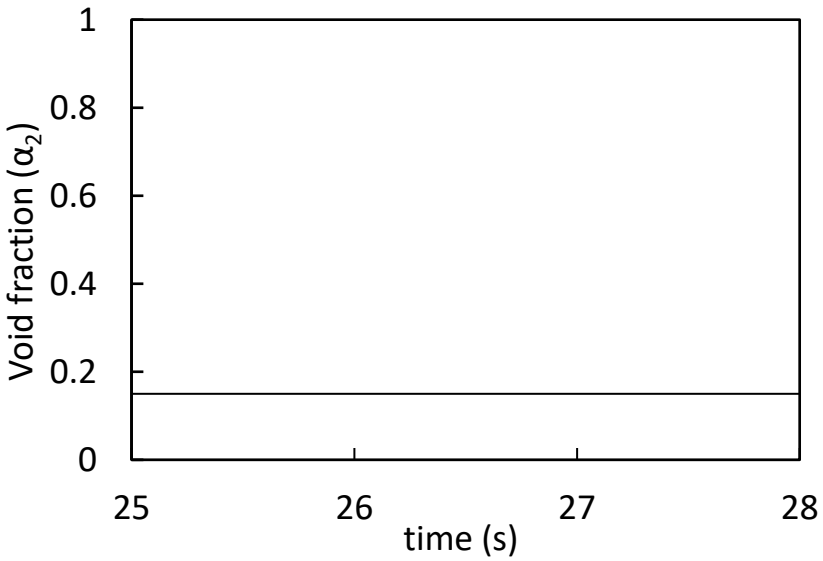

Figure 53: Stable dispersed bubbly flow simulation at 15% void fraction

4. CONCLUSIONS

4.1 Mechanistic TFM

1) The 1D mechanistic TFM of Ishii [1] can be made well-posed, unstable and Lyapunov stable provided appropriate physical mechanisms pertaining to the phasic interactions are included.
2) The physical mechanism of wake entrainment is proposed for clustering of dispersed bubbles leading to formation of bubble clusters, useful for predicting bubbly to slug flow regime transition in vertical adiabatic two-phase flows.
3) The wake entrainment force was derived from a first order linearization of the interfacial drag force using a churn turbulent flow drag law.
4) The mechanistic 1D Shallow Water TFM, which is an asymptotic case of the mechanistic 1D TFM, was used to analyze the local instability due to wake entrainment.
5) The linear stability analysis comprising of the characteristic and dispersion analyses was used to determine the stability of the TFM. Due to the presence of the wake entrainment instability, the 1D Shallow Water TFM was found to be KH unstable.
6) The numerical simulations were used to analyze the nonlinear stability of the 1D mechanistic TFM.
7) The simulations of the 1D Shallow Water TFM were validated for the case of dispersed and clustered bubbly flows:
    a) For the dispersed bubbly flow regime at lower void fractions, the void fractions waves are stable and there is no amplification because the wake entrainment effect is negligible as the bubbles are far away from each other and do not.
    b) For higher void fractions, the wake entrainment instability induced clustering. This caused the void fraction waves to grow, leading to the development of interfacial structures specific to bubble clusters.
8) The wavelengths and the wave speeds of the numerical calculations are in reasonable agreement with the experimental data of Cheng and Azzopardi [2] and Song et al. [3]. However, the amplitude of the void wave simulations is low when compared to the experimental data for bubble clusters.

9) The instabilities can be predicted with 3D CFD. However, due to the significant amount of numerical diffusion present in the CFD TFM solver in Fluent, very fine mesh sizes were necessary.

4.2 Variational TFM

1) A well posed and unstable 1D variational TFM capable of simulating the development of clusters and Taylor bubbles for vertical adiabatic air-water two-phase flows was proposed.
2) A comparison of the 1D mechanistic TFM with the variational TFM showed that there are additional conservative interfacial momentum transfer terms in the variational TFM, which make it objective, i.e., frame invariant (Geurst [4], [21]).
3) The variational approach was used to derive the 1D Shallow Water TFM equations following the formulation of Pauchon and Smereka [20]. It is shown that the void fraction and drift flux are the natural variables to model local two-phase instabilities.
4) Potential flow theory was used for formulation of the inertial coupling coefficient for a single bubble moving in liquid, applicable for dilute bubbly flows. The values of the virtual mass and interfacial pressure coefficients obtained from the inertial coupling coefficient agree with the values generally used in the mechanistic TFM for stable dispersed bubbly flows.
5) Potential flow theory was then used to model interaction between two bubbles arranged in an in-line configuration and the virtual mass coefficient is in decent agreement with the analytical solutions available in literature.
6) Using a lumped parameter model, objective constitutive models for the conservative interfacial forces were developed for wake entrainment through the formulation of the inertial coupling.
7) Starting from the Taylor bubble model of Wallis, a confined vortex behind the Taylor bubble was added to the lumped parameter model for wake entrainment.
8) The local drag coefficient was obtained from the experimental data using the kinematic approximation, i.e., the force balance between drag and gravity for the interfacial drag force.
9) The Eigenvalues of the 1D variational Shallow Water TFM were calculated using characteristic analysis. The model was found to be hyperbolic, i.e., with real Eigenvalues which represent the propagation speed of the void waves.
10) Through dispersion analysis, it was shown that the 1D variational Shallow Water TFM is SWT well-posed and SWT unstable.

11) For verification of the 1D variational Shallow Water TFM simulations, it was first shown for the model of Wallis [22] that when the gas to liquid density ratio is negligible, the momentum equation reduces to the well-known Burgers equation. Moreover, the Burgers equation was found to be decoupled from the continuity equation so verifications of the numerical solutions for both the continuity and momentum equations were possible.
12) For validation, the model was then solved numerically to simulate the development of interfacial structures associated with bubble clusters and Taylor bubbles:
13) For the slug flow regime at higher void fractions, the void fraction waves grow due to clustering and the unique interfacial structures associated with Taylor bubbles were obtained.
14) Extrapolation of the wake entrainment model for lower void fractions led to the formation of bubble clusters due to growth of the void waves. Discrepancy was found in the flow regime boundary prediction for clustered bubbly flows. The model predicts onset of clustered bubbly flow regime at void fractions higher than the experimental data.
15) When the model was extrapolated further to even lower void fractions, stable void fraction waves were obtained as the initial perturbations decay. But the extrapolation fails for very low void fractions.
16) The growth rate and development of the void fraction waves for clustered bubbly and slug flow were shown to be non-linearly bounded.
17) The comparison of wave propagation properties of the void fraction waves in terms of the frequency, amplitude, width and propagation speeds, agrees with the experimental data.
18) Thus, the short-wave two-phase flow simulation capability of the TFM is demonstrated for slug flow and the bubbly to slug flow regime transition in vertical adiabatic two-phase flows.

5. FUTURE WORK

The following recommendations are proposed:

1) The model can be improved by revising the definition of α_s for lower void fractions to make the 1D variational Shallow Water TFM is SWT stable for $\alpha_2 \leq 0.15$. The definition of α_s such that $\alpha_s \geq 0.87$ for unstable clustered bubbly and slug flow regimes is physically valid. However, for the stable dispersed bubbly flow regime, the α_s that can be attained should be approximately the same magnitude as that of α_2, i.e., $\alpha_s \approx \alpha_2$ would be more accurate.

2) The proposed 1D variational Shallow Water TFM can be more complete by adding a viscous diffusion term in the momentum equation. The viscous diffusion mechanism will be significant due to eddy diffusivity in the liquid slug region because of the presence of the toroidal vortex. This would require a localized formulation of the net viscosity based on the local void fraction and the effect of eddy diffusivity on the linear and non-linear stability of TFM will require more analysis.

3) The 1D industrial codes such as RELAP 5 use the full TFM. Since the 1D Shallow Water TFM is an asymptotic case of the 1D TFM, the constitutive models developed for the Shallow Water TFM may be transferred to the full four equation TFM for real-world engineering applications.

APPENDIX

A.1 Drag and Wake Entrainment Length Scales

The two experimental data sets of Cheng and Azzopardi [2] and Song et al. [3] are shown in Fig. 54 in a flow regime map,

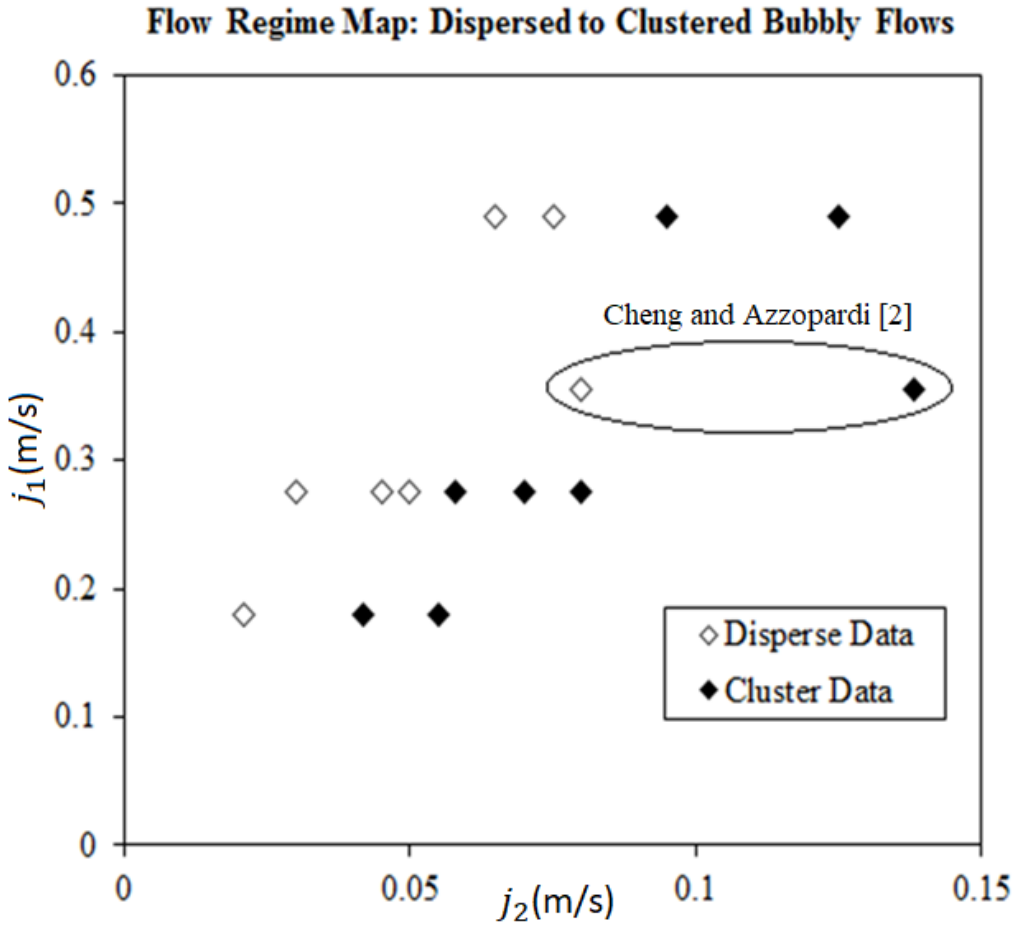

Figure 54 : Flow regime map for dispersed and clustered bubbly flow data

The marked data set in Fig. 54 is for the mean bubble diameter of 3.62 mm of Cheng and Azzopardi [2], while the rest of the data is for 4.8 mm of Song et al. [3] j_1 and j_2 correspond to the liquid and gas volumetric flux (superficial velocities) respectively and the flow regime map in Fig. 54 covers the dispersed and clustered bubbly flows. The experimental data sets of dispersed and clustered bubbles are separated from each other for given mean bubble diameter and flow conditions. Since the wake entrainment force is directly proportional to the square of the relative velocity, the

transition from dispersed to clustered bubbles can be predicted if the right relative velocity is obtained by choosing a suitable length scale combination for the interfacial drag and wake entrainment force. This is the motivation behind defining a relationship of length scales for the wake entrainment force and the interfacial drag force, L_{WE} and L_D, as $L_{WE} = 10L_D$. This is consistent with the wavelengths of void fraction waves for bubble clusters from experiments found to be approximately ten times the mean bubble diameter.

With the force balance between gravity and interfacial drag determining the relative velocity, $L_{Drag} = D_b$ for dispersed bubbles and $L_{Drag} = 2D_b$ for clustered bubbles were found to give a reasonable prediction of the range of relative velocity measurements as shown in Fig. 55.

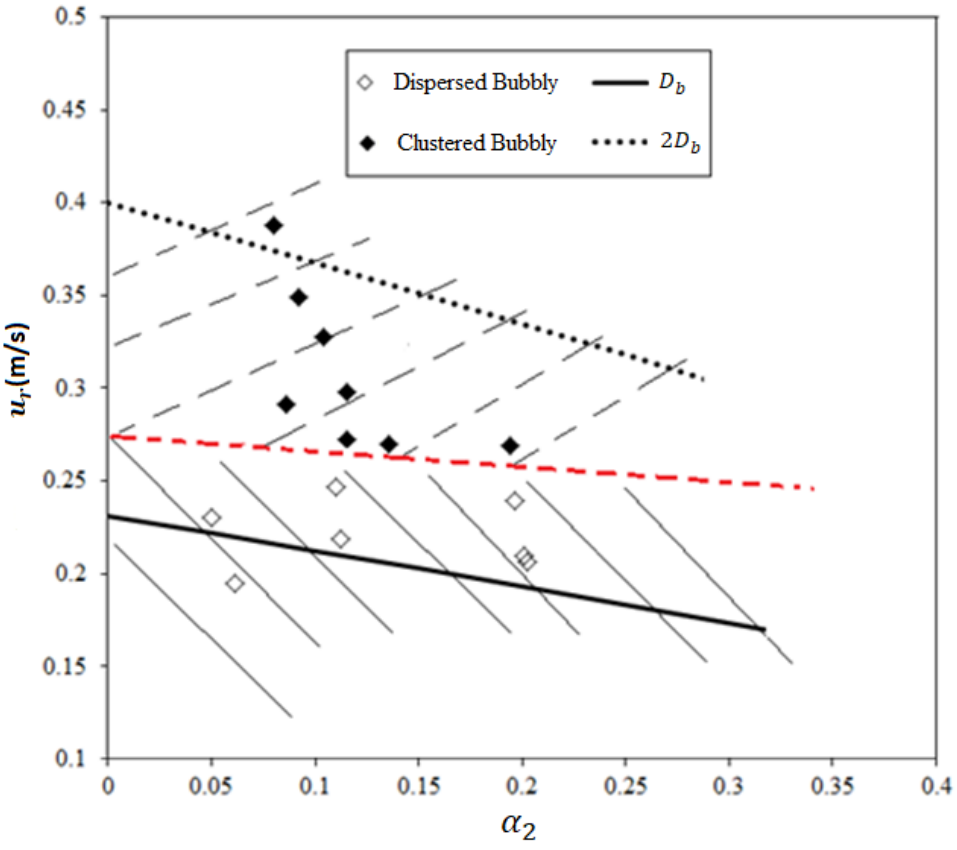

Figure 55: Relative velocity calculation using the kinematic approximation

A.2 Collision Force

The collision force model of Alajbegovic [44] is given by,

$$M^{coll} = -\nabla.\left[(\rho_2 + \rho_1 c_{vm})\, q(\alpha_2)\alpha_2^2\left(2\overline{u_2' u_2'} + \overline{u_2'.u_2'}I\right)\right] \tag{202}$$

where I is the identity tensor. The stress tensor in the gas phase and the liquid phase can be related using the assumption of equilibrium in turbulence as,

$$\overline{u_2' u_2'} = \frac{1}{1+\frac{\tau_p}{\tau_c}}\,\overline{u_1' u_1'} \tag{203}$$

Since eddies are generated due to presence of bubbles in the continuous liquid phase, their time constant τ_c is,

$$\tau_c = \frac{D_b}{u_r} \tag{204}$$

In the above equation, u_r is the relative velocity between the phases and D_b is the bubble diameter. From force balance on a single bubble, the relaxation time τ_p for bubbles when assumed to be solid spheres can be obtained as,

$$(\rho_2 + \rho_2\, c_{vm})\frac{du_2}{dt} = -\frac{3}{4}\,\frac{c_D\, Re\, \mu_1\, \mu_2}{D_b^2} \tag{205}$$

$$\tau_p = \frac{4}{3}\,\frac{(\rho_2 + \rho_1\, c_{vm})\, D_b^2}{c_D\, Re\, \mu_1} \tag{206}$$

Following Lopez de Bertodano et al. [38], the stress tensor for liquid phase due to bubble induced turbulence is,

$$\overline{u_1' u_1'} = \begin{bmatrix} 4/5 & 0 & 0 \\ 0 & 3/5 & 0 \\ 0 & 0 & 3/5 \end{bmatrix} \frac{1}{2}\, c_{vm}\, \alpha_2\, |u_r|^2 \tag{207}$$

Assuming the stress tensor to be isotropic for the bubble induced component,

$$M^{coll} = -c_{coll}\, \rho_1\, c_{vm}^2\, \nabla.[g\,(\alpha_2)\, \alpha_2^3\, |u_r|^2\, I] \tag{208}$$

For the 1D TFM, the collision can be reduced to,

$$M^{coll} = -c_{coll}\rho_1 c_{vm}^2\left[\left(3\alpha_2^2 u_r^2 q(\alpha_2) + \alpha_2^3 u_r^2\frac{dq(\alpha_2)}{d\alpha_2}\right)\frac{\partial \alpha_2}{\partial x} + +2\alpha_2^3 u_r q(\alpha_2)\frac{\partial u_r}{\partial x}\right] \tag{209}$$

where $q(\alpha_2)$ is the pair correlation function.

A.3 CFD Simulations

A.3.1 Methodology

In the previous section, it was shown that the wake entrainment instability can be triggered by adding the wake entrainment force term which of the form of a gradient of void fraction term. This section presents the extension of the in-house 1D mechanistic Shallow Water TFM results to the complete TFM present in commercial CFD package, ANSYS Fluent (version 15.0). Quasi-1D simulations were performed in a 2D domain to check if it is possible to simulate the growth of void fraction waves due to wake entrainment.

The computational domain and boundary conditions used for the Fluent calculations are given in Fig. 56 and Table 7 respectively. A constant volumetric flux is set at the inlet. The mesh size of 0.5 mm was used to counter high numerical diffusion present in the Eulerian TFM solver of Fluent. To cut down the computational cost due to very small mesh size being used, the dimensions of computational domain were reduced to 60 cm and 5 cm along axial and transverse direction respectively. Use of periodic fixed flux boundary condition at inlet and outlet didn't give convergent results, as the implementation of periodic boundary conditions in Fluent led to increase in the liquid and gas velocities with time, giving unrealistic velocity values. The MUSCL scheme (flux-limiter numerical scheme) was chosen for spatial discretization of momentum terms. The bounded second order implicit scheme for time advancement and Phase-Coupled SIMPLE scheme of pressure-velocity coupling were used. The Fluent simulations were run in parallel on 8 processors, for total physical time of 1 second due to high computational cost associated with using 0.5 mm mesh.

The collision and wake entrainment forces were included in the momentum equations of the TFM through User Defined Functions (UDFs), loaded dynamically within ANSYS Fluent to modify and add to its standard features. The UDFs are defined using DEFINE macros provided by Fluent and are compiled first and then built into the library prior to initializing the domain and running the respective Fluent case files. An additional UDF was defined for the purpose of storing the void fraction as well as velocity gradient, since the collision force, wake entrainment and interfacial pressure terms are defined in terms of these gradients. Table 8 gives a brief outline of the different UDFs used for the CFD calculations.

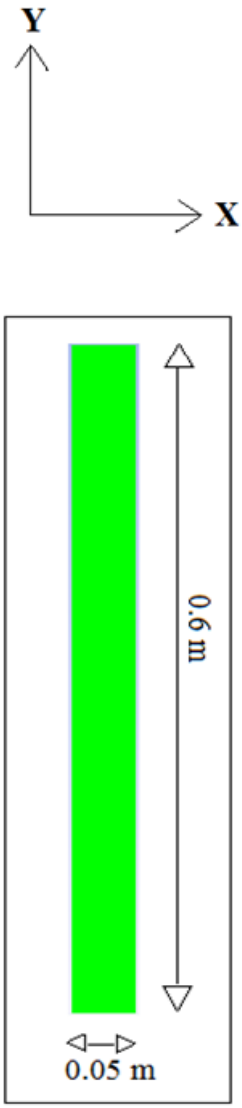

Figure 56: Quasi-1D domain used for CFD simulations in Fluent

Table 7: Boundary conditions used in Fluent for quasi-1D simulations

Boundary Conditions	
Top	Pressure Outlet
Bottom	Velocity Inlet
Left	Symmetry
Right	Symmetry

Table 8: List of UDFs used for the TFM solver in ANSYS Fluent

UDF (.c file)	Flow Direction	Purpose
PintSource_x.c	X	Add interfacial pressure, collision force terms
PintSource_y.c	Y	Add interfacial pressure, collision force & wake entrainment terms
Store_void_grad.c	X and Y	Create memory locations for storing void fraction & velocity gradients
VF_in.c	Y	Initialization of the domain with perturbed void fraction profile
CD.c	X and Y	Modify interfacial drag coefficient

A.3.2CFD Results

The transport of a Gaussian wave was used to check the feasibility of predicting void wave instabilities using Eulerian TFM solver in Fluent. Three different grid sizes of 1.2 mm, 0.6 mm and 0.3 mm were used along the axial direction. The grid size used for transverse direction (x-axis) was 1.25 mm and the simulations were run for 5 seconds. Fig. 57 shows the contour plot of the propagation of the Gaussian wave using quasi 1D simulation in Fluent for 0.6 mm grid size. The initially perturbed void wave grows in size, as the void wave peak reaches up to 27% from the initial peak of 25%.

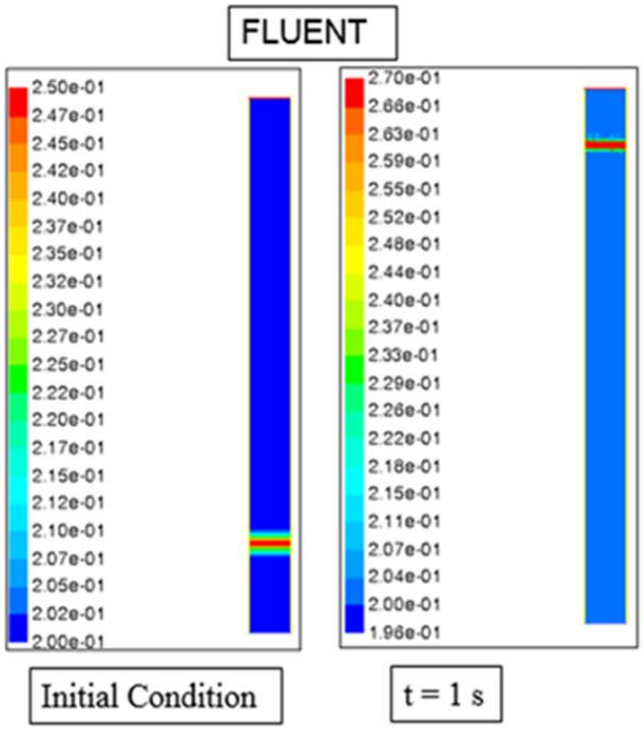

Figure 57: Contour plot of void fraction from Fluent using 0.5 mm mesh in axial direction

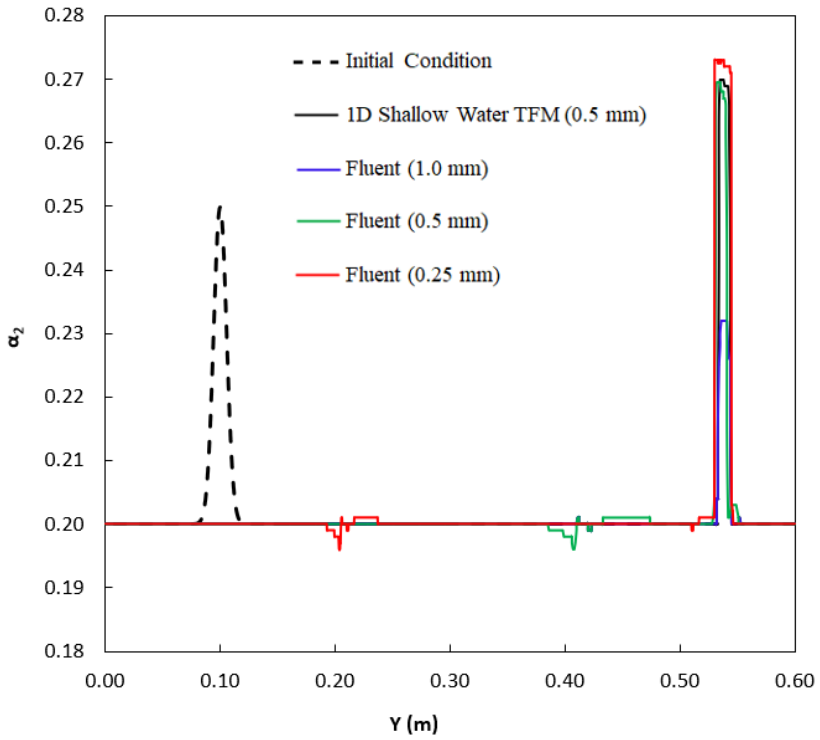

Figure 58: Comparison of Shallow Water TFM and CFD simulations for different grid sizes

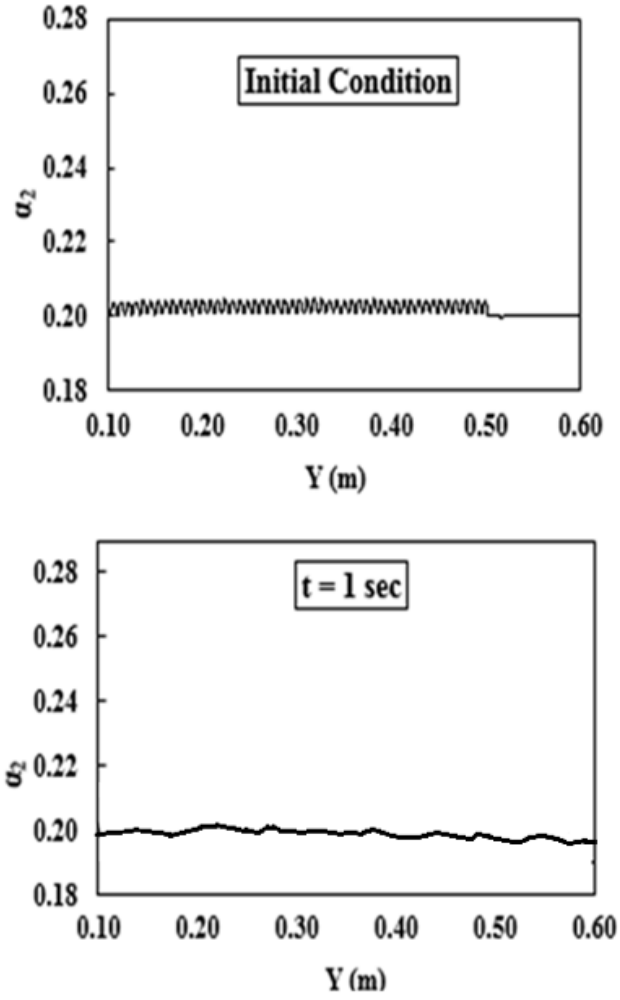

Figure 59: Fluent results with perturbed initial condition for mesh size of 1 mm

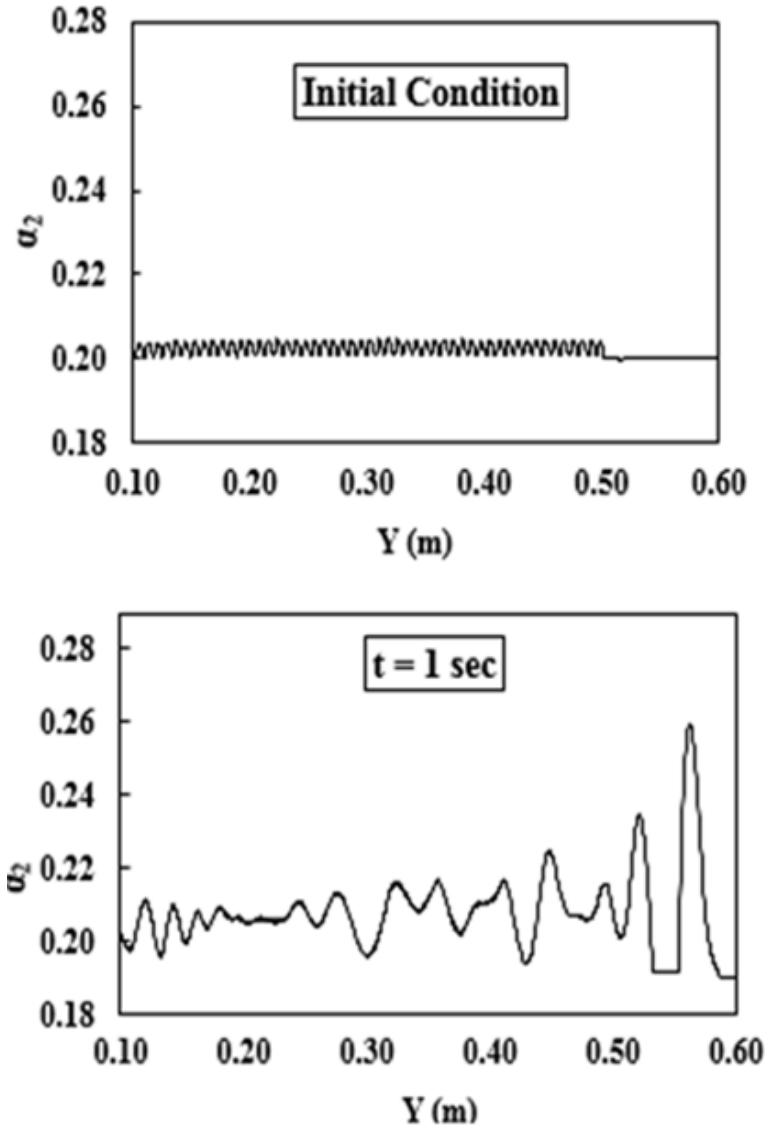

Figure 60: CFD results with perturbed initial condition for mesh size of 0.5 mm

A comparison of the 1D Shallow Water TFM results with the quasi-1D CFD results is also shown Fig. 58. It can be seen that the void wave does not grow unless a fine mesh of 0.5 mm is used due to high numerical viscosity present in the TFM solver of Fluent. Also, a fully converged solution could not be demonstrated for the mesh sizes used. As the next step, the domain was initialized with a perturbed void fraction profile similar to the 1D Shallow Water TFM calculations. As seen in Fig. 58, the perturbed void fraction waves get attenuated for a coarse mesh of 1 mm. But the waves do grow in amplitude in Fig. 60 only when a fine mesh of 0.5 mm is used and this agrees with the results in of Fig. 58. Also, the wavelengths of the void fraction waves in Fig. 60 are in

reasonable agreement with the most dangerous wavelength of ≈ 5 cm obtained from the dispersion analysis. It can be concluded that the stability analysis of 1D Shallow Water TFM to CFD calculations. But the prediction of growth of void waves due to wake entrainment instability requires use of very fine mesh sizes and this leads to high computational cost associated with CFD calculations, as has been verified for quasi 1D simulations (8-9 hours). The computational cost for full 3D CFD simulations look prohibitive at this time. A rough estimate based on the computations of Vaidheeswaran [46] for a bubble plume with a mesh size of 1 mm is that a similar simulation would take 8-12 months.

A.4 Parametric Study

The aim of the parametric study presented here is to determine the values of X_0, b_w and α_s parameters in the inertial coupling coefficient of the confined vortex model. Since the main objective of the current work is to have a well-posed and unstable 1D Shallow Water TFM that can simulate flow regime transition from dispersed bubbly to clustered bubbly and slug flow, the following criteria for evaluation of the values for X_0, b_w and α_s parameters are defined:

a) A stable bubbly flow regime should exist for $0 < \alpha_2 \leq 0.2$. If any perturbation is introduced in α_2 and/or ΓJ, the perturbation should decay to a steady state value.
b) An unstable region is needed for $0.2 \leq \alpha_2 \leq 0.3$ for the clustered bubbly flow regime. Any perturbation introduced in α_2 and/or ΓJ should lead to growth and non-linear evolution of the void fraction waves corresponding to the interfacial structure of bubble clusters.
c) An unstable region for $0.3 \leq \alpha_2 \leq 0.55$ for the slug flow regime is required. Any perturbation introduced in α_2 and/or ΓJ will lead to growth and non-linear development void fraction waves associated with the Taylor bubbles.

An overlapping criterion for all the three flow regimes is that the shape, amplitude and frequency of the void fraction signals obtained from the numerical simulations should resemble the experimental measurements. The three criteria (a, b, c) are an idealization and give a reference point against which the required parametric study can be performed. The complicated thermo-fluid dynamics of two-phase flows are dependent on various factors like fluid properties, operating pressure, flow geometry and flow boundary conditions. These affect the onset and transition of different two-phase flow patterns. For example, the clustered bubbly flow regime can start for void fractions as low as $\alpha_2 = 0.10$ depending on the inlet flow conditions. Nevertheless, the

aforementioned criteria still serve as a good starting point for the parametric study, such that stable dispersed bubbly, unstable clustered bubbly and slug flow regimes can be resolved dynamically while simultaneously confirming to the experimental observations as much as possible.

A.4.1Calibration of Vortex Parameters

The calibration for the range of X_0 and b_w values is obtained from air-water slug flow experiments of Shemer et al. [57]. The axial profile of centerline velocity for the confined vortex behind a Taylor bubble in a 26 mm dimeter pipe and for $Re_L = 13800$ is chosen, as it is closest to the slug flow data of Song et al. [3] for α_2 = 0.405 in a 25 mm diameter pipe. A comparison of the flow conditions from the two different experimental data sets is given in Table 9.

Table 9: Comparison of the flow conditions for calibration of vortex parameters

Data	$D_{pipe}(m)$	$u_1\ (m/s)$	$u_2\ (m/s)$	Re_L
Song et al. [3]	0.025	0.46	0.73	12951.53
Shemer et al. [57]	0.026	0.53	0.81	13800

According to the definition of vortex velocity $u_w(x^*, r^*)$ in Eq. (163), the axial distribution of the centerline velocity is,

$$\frac{u_w(x^*, 0)}{u_2} = X_0 \left(\frac{1}{x^* + 1}\right) \tag{210}$$

Based on vortex velocity at the trailing edge of the Taylor bubble $x^* = 0$, X_0 can be varied. Since $x^* = x/H_w$, with H_w as an appropriate length scale for vortex decay, H_w can be defined as a function of the pipe diameter D_{pipe} as,

$$H_w = c_w D_{pipe} \tag{211}$$

The axial distribution of the centerline velocity will be,

$$\frac{u_w(x^*, 0)}{u_2} = X_0 \left[\frac{1}{\left(\frac{x}{c_w D_{pipe}}\right) + 1}\right] \tag{212}$$

Now from the definitions of α_2 and α_s in the lumped parameter model and for $H_g/D_{pipe} = 3$ from the data of Shemer et al. [57], the D_{pipe}/H ratio and b_w can be written as,

$$\frac{D_{pipe}}{H} = \frac{\alpha_2}{3\,\alpha_s} \tag{213}$$

$$b_w = \frac{c_w\,\alpha_2}{3\,\alpha_s} \tag{214}$$

Hence a range of b_w values can be obtained for different c_w values, which determine the rate of axial vortex decay. For first approximation, assuming that the differences in the flow geometry and flow conditions in Table 9 do not lead to much variation in the mean void fraction value of $\alpha_2 = 0.405$, three sets of X_0 and b_w values are given in Table 10 for $\alpha_s = 0.92$.

Table 10: Set-I, II and III vortex parameters

	c_w	b_w	X_0
Set-I	1	0.2	5
Set-II	0.5	0.1	4
Set-II	0.25	0.05	3

The axial profile of the confined vortex's centerline velocity from the lumped parameter model for the three sets of X_0 and b_w values is shown in Fig. 61 for $Re = 13800$ and $D_{pipe} = 26\ mm$ from the data of Shemer et al. [57]. The range of X_0 and b_w values obtained do cover an acceptable range with regard to the vortex intensity and the axial decay rate of the vortex velocity. A small discrepancy near the trailing edge of the Taylor bubble does exist and this inconsistency is ignored as a first approach for the modeling work presented.

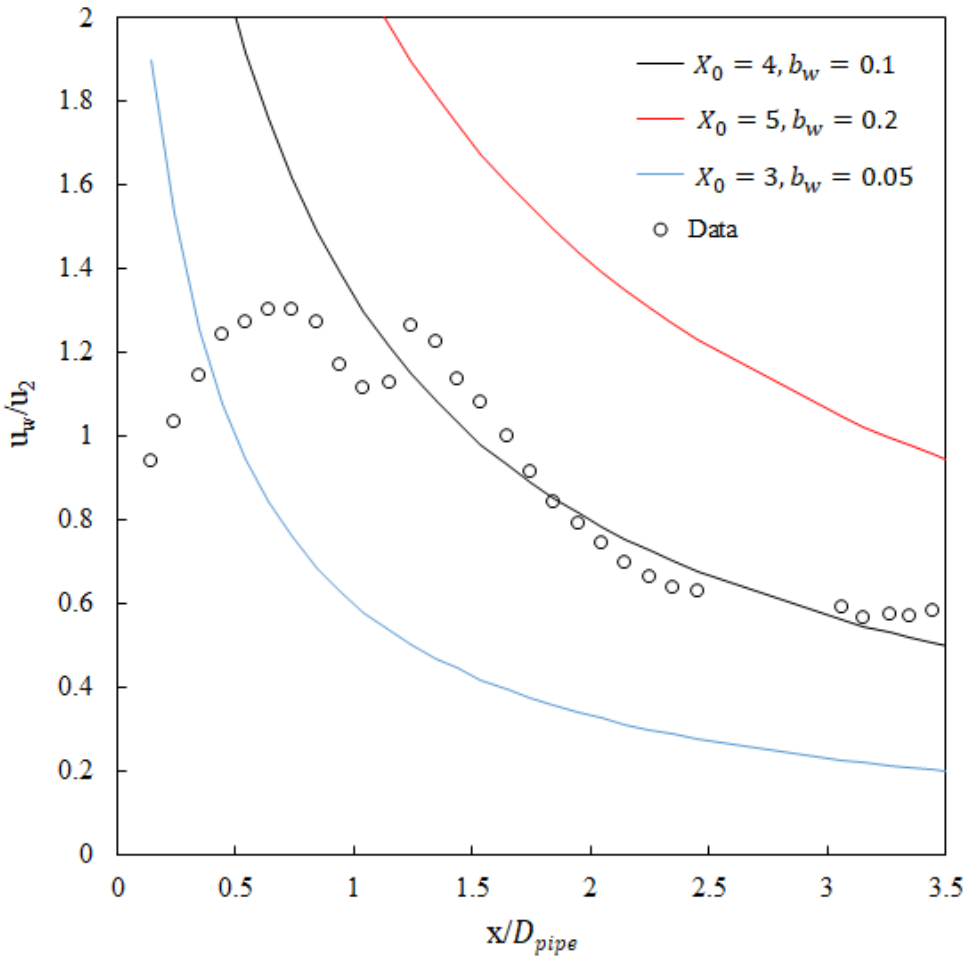

Figure 61: Calibration of vortex parameters for centerline vortex velocity

A.4.2 Effect of Vortex Parameters on Linear and Non-linear Stability

The linear and non-linear stability of the 1D variational Shallow Water TFM are used for analyzing the effect of X_0 and b_w parameters. The goal is to find a fixed set of X_0 and b_w values that can resolve development of interfacial structures for dispersed bubble, clustered bubbly and slug flow regimes such that the three criteria stated before are satisfied. The stability map from dispersion relation and the numerical simulations are employed for linear and non-linear stability analysis. For bubble clusters and Taylor bubbles, the value of $\alpha_s \approx 0.90$. From the stability map, it was found that as the value of α_s increases, the range of α_2 for which the model is SWT unstable increases along with an increase in the amplitude of the void fractions waves. The optimum value of $\alpha_s = 0.92$ was chosen such that the model is unstable for widest possible range of α_2 to cover

both the clustered bubbly and slug flow regimes and the growth of void fraction waves is bounded. The simulation results presented were performed using a 1 mm mesh size and for $\alpha_s = 0.92$.

The stability map for $X_0 = 5, b_w = 0.2$ from Set-I is shown in Fig. 62 and the numerical simulations for mean gas void fraction of 0.4, 0.44 and 0.5 are shown in Fig. 63 respectively.

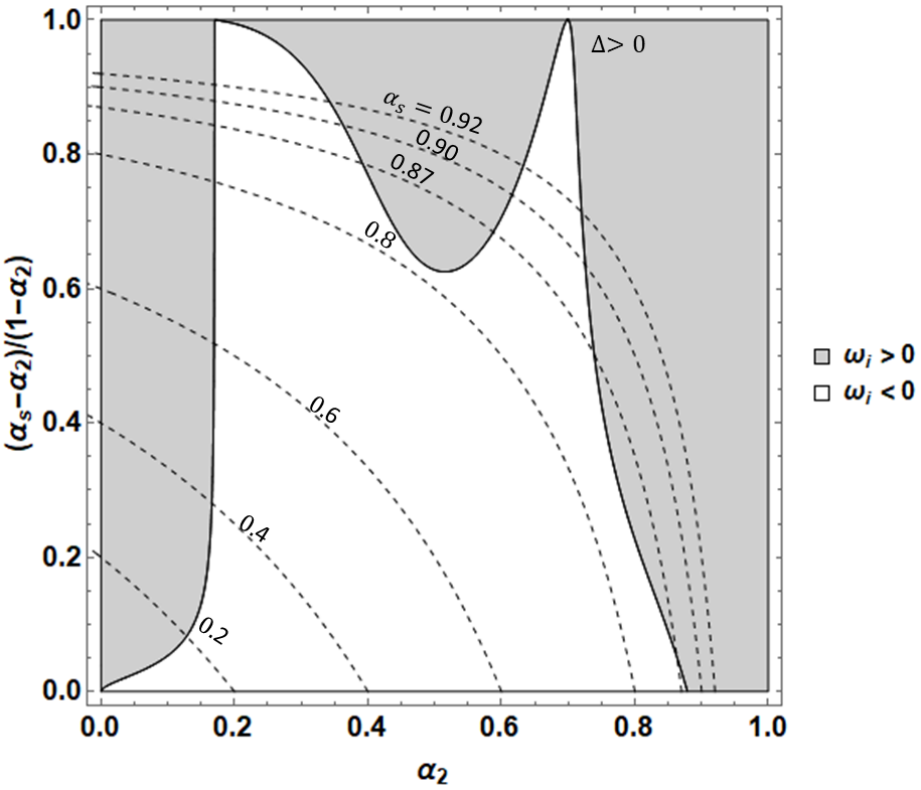

Figure 62: Stability map for Set-I vortex parameters

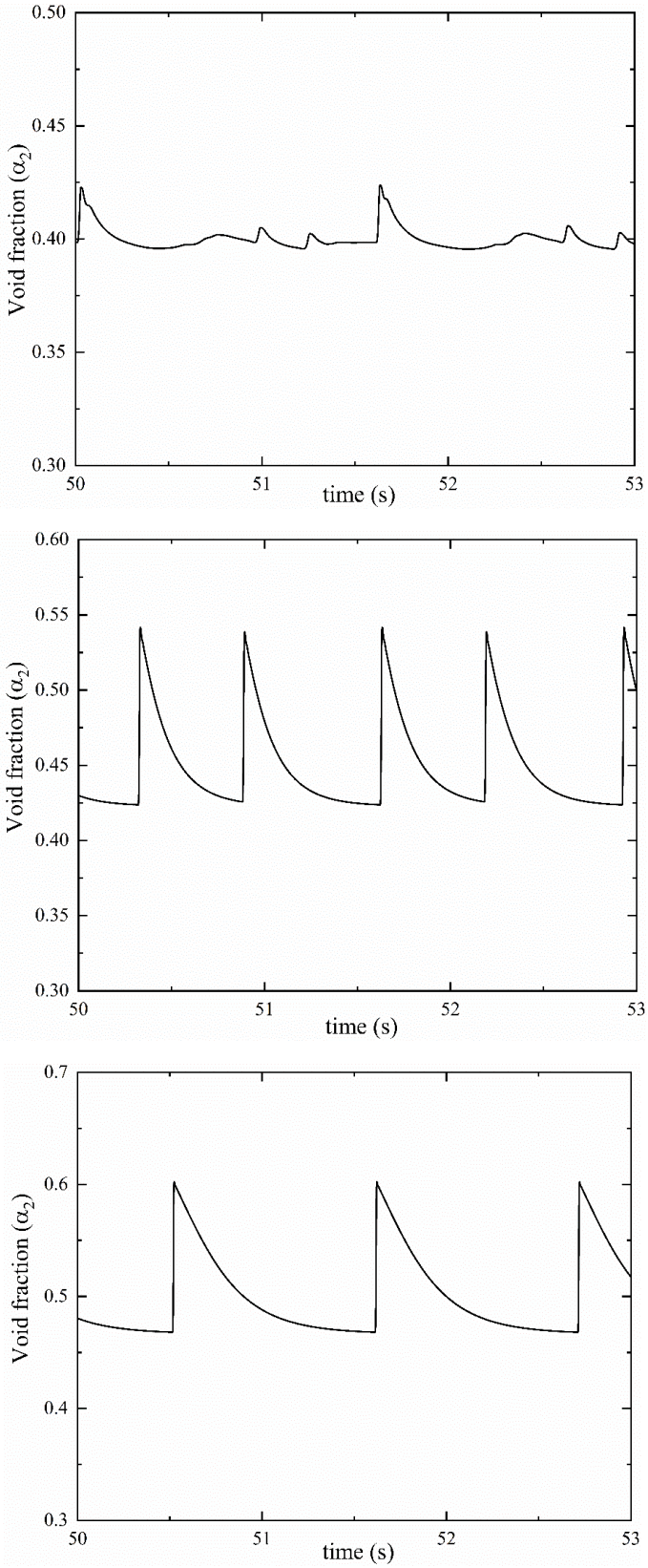

Figure 63: Set-I results for 40%, 44% and 50% mean void fraction (top to bottom)

For $X_0 = 5, b_w = 0.2$ and $\alpha_s = 0.92$, the model is stable as evident from the stability map in the range of $0.15 \leq \alpha_2 < 0.4$. From first observation, Set-I fails to account for the unstable clustered bubbly flow regime. Though the model is unstable for the slug flow regime in the range of $0.4 \leq \alpha_2 \leq 0.5$, the void fractions signals from the simulations do not resemble the experimental data in terms of their shape and amplitude. Moreover, the growth rate is also underpredicted as it takes close to 50 seconds for the void waves to grow and evolve. For Set-III, the stability map with $X_0 = 3, b_w = 0.05$ is displayed in Fig. 64 and Fig. 65 shows the simulation results for mean void fraction of 0.3, 0.4 and 0.44 respectively.

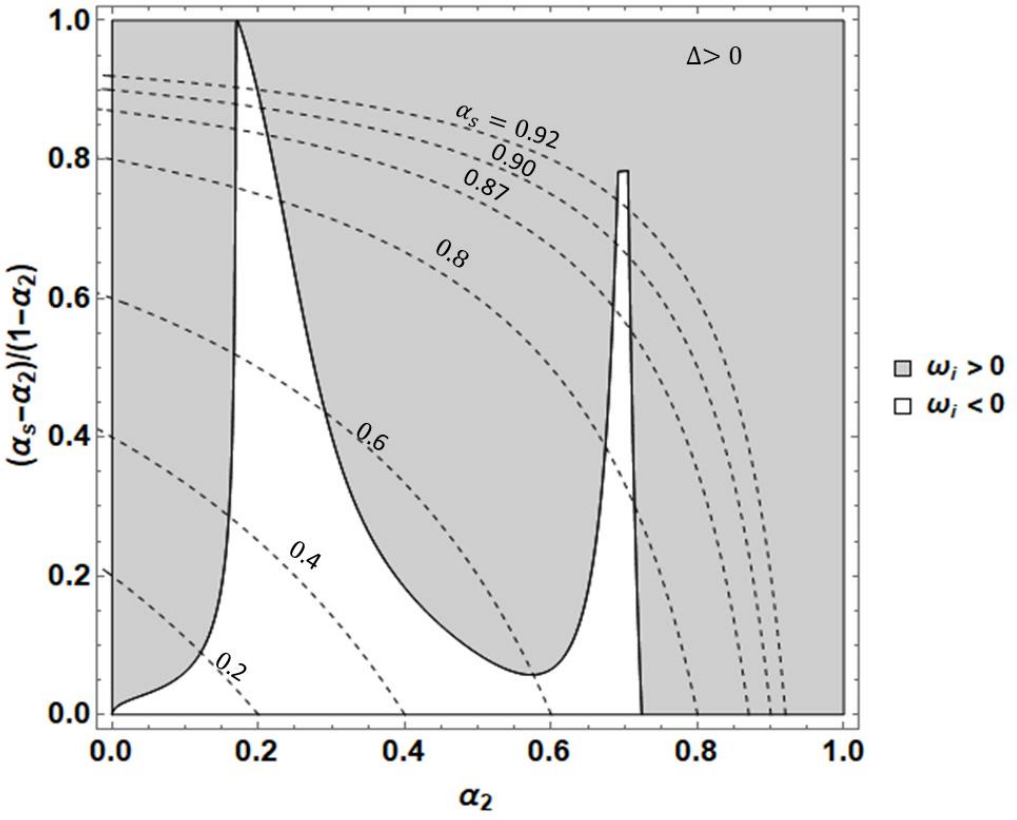

Figure 64: Stability map for Set-II vortex parameters

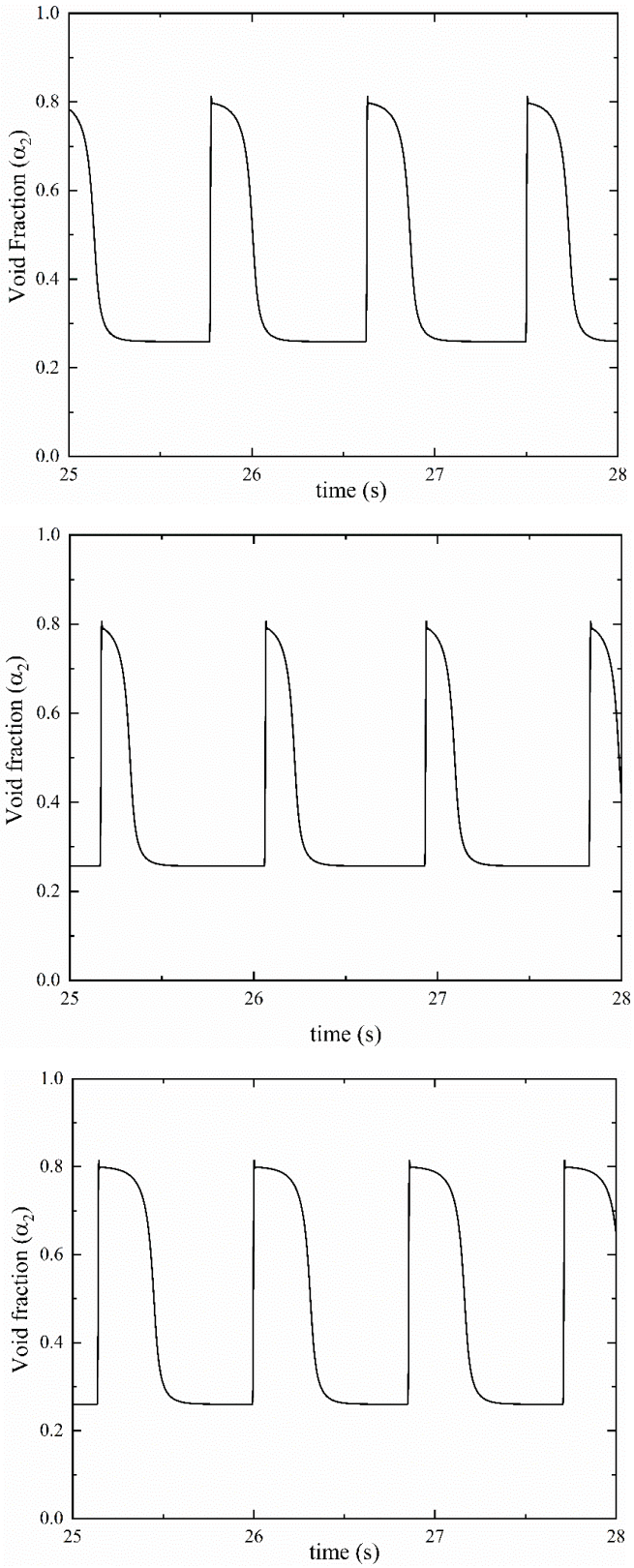

Figure 65: Set-III results for 30%, 40% and 44% void fraction (from top to bottom)

For $X_0 = 3, b_w = 0.05$, the model is unstable according to the stability map in the range of $0.22 \leq \alpha_2 < 0.5$. But the void fraction waves resemble that of the slug flow regime even for low void fraction range where it is desired to have a clustered bubbly flow regime. Though the growth rate is more than that of Set-I and is reasonable, the model predicts slug flow regime throughout the unstable region and hence fails to capture the clustered bubbly flow regime. At last, the stability map for $X_0 = 4, b_w = 0.1$ from Set-II are given in Fig. 66. The numerical simulation results for mean gas void fraction of 0.27, 0.3, 0.4 and 0.5 are shown in Fig. 67 respectively.

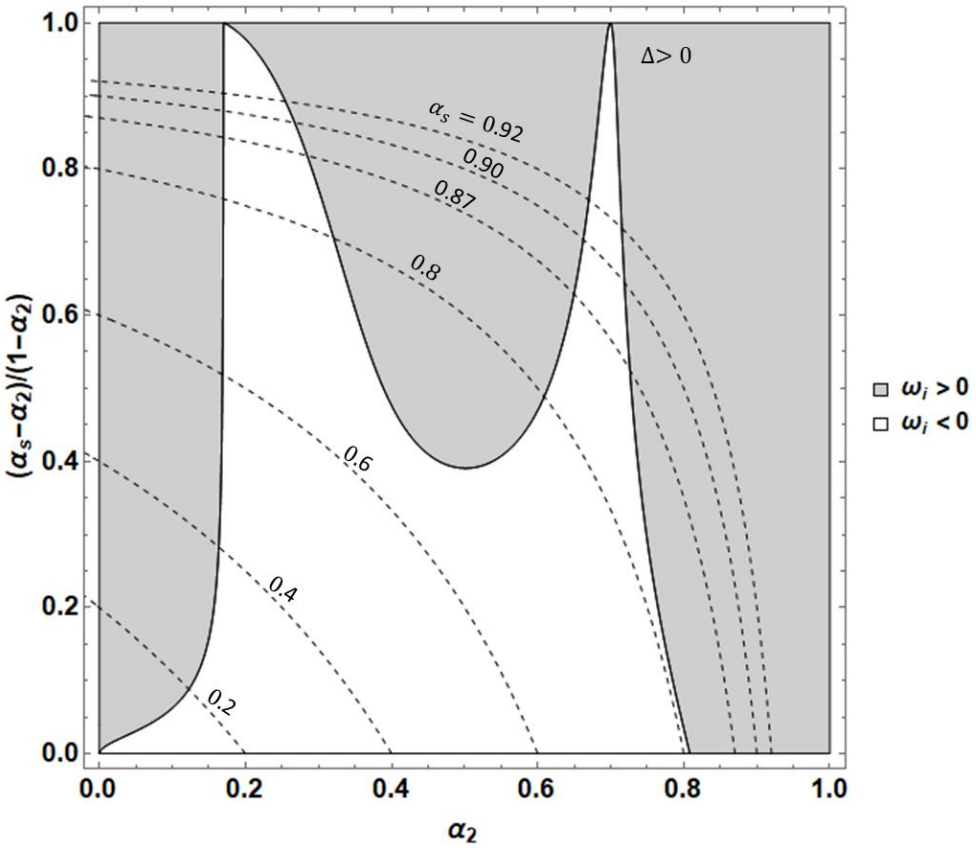

Figure 66: Stability map for Set-III vortex parameters

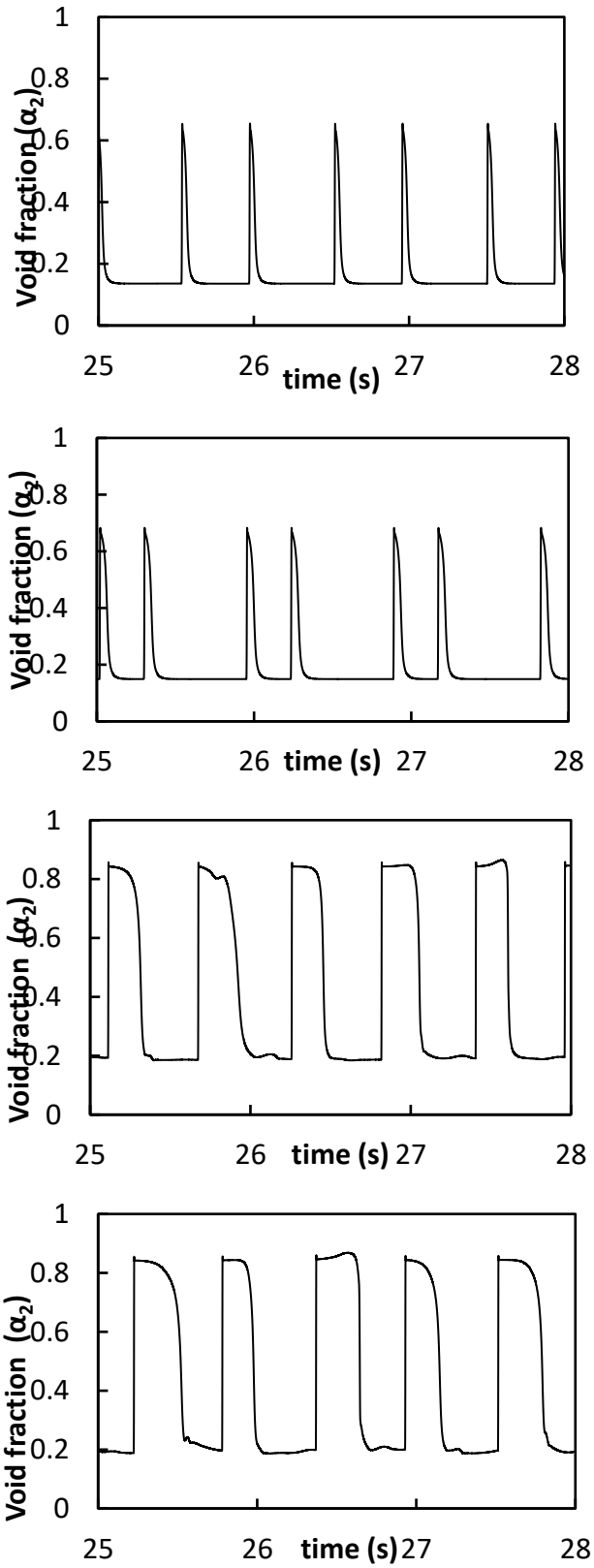

Figure 67: Set-II results for 27%, 30%, 40% and 50% void fraction (from top to bottom)

For $X_0 = 4, b_w = 0.1$, the model is unstable according to the stability map in the range of $0.27 \leq \alpha_2 \leq 0.5$. For the intermediate void fraction values of $\alpha_2 = 0.27$ and 0.3, the void fraction waves resemble clustered bubbly flow regime. In addition, for $0.4 \leq \alpha_2 \leq 0.5$, the void fractions waves are similar to the slug flow regime. The growth rate is similar to that of Set-III and the shape of the waves is similar to that observed in the experiments. This confirms the capability of the model to predict clustered bubbly flow and slug flow regimes dynamically as stated in the criteria. Hence $X_0 = 4, b_w = 0.1$ and $\alpha_s = 0.92$ are by far the best possible values that can be assigned to the vortex model and are chosen for validation of the numerical simulation results.

REFERENCES

[1] M. Ishii, Thermo-Fluid dynamic theory of two-phase flow, Paris: Eyrolles, 1975.

[2] H. Cheng, J. H. Hills and B. J. Azzopardi, "Effects of Initial Bubble Size on Flow Pattern Transition in a 28.9 mm Diameter Column," *International Journal of Multiphase Flow*, vol. 28, pp. 1047-1062, 2002.

[3] C. Song, H. No and M. Chung, "Investigation of Bubble Flow Developments and its Transition Based on the Instability of Void Fraction Waves," *International Journal of Multiphase Flows*, vol. 21, no. 3, pp. 381-404, 1995.

[4] J. Geurst, "Virtual mass in two-phase bubbly flow," *Physica A: Statistical Mechanics and its Applications*, vol. 129, no. 2, pp. 233-261, 1985.

[5] R. Davies and S. G. Taylor, "The mechanics of large bubbles rising through extended liquids and through liquids in tubes," in *Dynamics of Curved Fronts*, Marseille, Academic Press, 1988, pp. 377-392.

[6] L. C. Ruspini, P. C. Marcel and A. Clausse, "Two-phase flow instabilities: A review," *International Journal of Heat and Mass Transfer*, vol. 71, pp. 521-548, 2014.

[7] M. Lopez de Bertodano, W. Fullmer, A. Clausse and V. Ransom, Two-Fluid Model Stability, Simulation and Chaos, Springer International Publishing, 2017.

[8] G. B. Whitham, Linear and Nonlinear Waves, Wiley-Interscience, 1974.

[9] G. B. Wallis, One Dimensional Two-Phase Flow, New York: McGraw-Hill, 1969.

[10] G. Nassos and S. Bankoff, "Propagation of density disturbances in an air–water flow," in *Proceedings of the Third International Heat Transfer Conference*, Chicago, 1966.

[11] Y. Mercadier, "Contribution to the study of propagations of void fraction perturbations in two-phase air-water flows with bubbles (PhD Thesis in French)," Inst. National Polytechnique de Grenoble, Grenoble (France), 1981.

[12] A. Matuszkiewicz, J. Flammand and J. Boure, "The bubble–slug flow pattern transition and instabilities of void fraction waves," *International Journal of Multiphase Flow*, vol. 12, no. 2, pp. 199-217, 1987.

[13] J. Park, R. Lahey Jr. and D. Drew, "The measurement of void waves in bubbly two-phase flows," in *Proceedings of the 6th International Meeting Nuclear Reactor Thermal-Hydraulics*, Grenoble, 1993.

[14] T. Taha and Z. Cui, "CFD Modelling of Slug Flow in Vertical Tubes," *Chemical Engineering Science* , pp. 676-687, 2006.

[15] M. Abdulkadir, V. Hernandez-Perez, S. Lo, I. Lowndes and B. Azzopardi, "Comparison of Experimental and Computational Fluid Dynamics (CFD) Studies of Slug Flow in a Vertical Riser," *Experimental Thermal and Fluid Science* , pp. 468-483, 2015.

[16] F. Galleni and R. Issa, "Mechanistic Simulation Of Slug Flow In Vertical Pipes Using The One-Dimensional Two-Fluid Model," *Multiphase Science and Technology*, pp. 229-245, 2015.

[17] M. Ishii and T. Hibiki, Thermo-fluid Dynamics of Two-phase Flow, 2 ed., New York: Springer, 2011.

[18] D. Drew and R. Lahey Jr., "The virtual mass and lift force on a sphere in rotating and straining inviscid flow," *International Journal of Multiphase Flow*, vol. 13, no. 1, pp. 113-121, 1987.

[19] G. B. Wallis, "On Geurst's equations for inertial coupling in two-phase flow," University of Minnesota, 1989.

[20] C. Pauchon and P. Smereka, "Momentum Interactions in Dispersed Flow: An Averaging and a Variational Approach," *International Journal of Multiphase Flows,* vol. 18, pp. 65-87, 1992.

[21] J. Geurst, "Variational principles and two-fluid hydrodynamics of bubbly liquid/gas mixtures," *Physica A: Statistical Mechanics and its Applications,* vol. 135, no. 2-3, pp. 455-486, 1986.

[22] G. B. Wallis, "Inertial coupling in two-phase flow: Macroscopic properties of suspensions in an inciscid fluid," *Multiphase Science and Technology,* vol. 5, no. 1-4, pp. 239-361, 1990.

[23] L. Wijngaarden, "Hydrodynamic interaction between gas bubbles in liquid," *Journal of Fluid Mechanics,* vol. 77, pp. 27-44, 1976.

[24] P. Smereka and G. W. Milton, "Bubbly Flow and its relation to conduction in composites," *Journal of Fluid Mechanics,* vol. 233, pp. 65-81, 1991.

[25] J. Kok, "Kinetic energy and added mass of hydrodynamically interacting gas bubbles in liquid," *Physica A: Statistical Mechanics and its Applications,* vol. 148, no. 1-2, pp. 240-252, 1988.

[26] D. Gidaspov, "Round table discussion (RT-12): Modelling of two-phase flow," in *Proceedings of the 15th International Heat Transfer Conference* , Tokyo, 1974.

[27] D. Drew and S. L. Passman, Theory of Multicomponent Fluids, New York: Springer, 1998.

[28] J. D. Ramshaw and J. A. Trapp, "Charactersitics, stability, and short-wavelenght phenomena in two-phase flow equation systems," *Nuclear Science and Engineering,* vol. 66, pp. 93-102, 1978.

[29] C. Pauchon and S. Banerjee, "Interphase Momentum Interaction Effects in the Averaged Multifield Model, Part 1: Void Propagation in Bubbly Flows," *International Journal of Multiphase Flow,* vol. 12, pp. 559-573, 1986.

[30] D. Barnea and Y. Taitel, "Kelvin-Helmholtz stability criteria for stratified flow: viscous versus non-viscous (inviscid) approaches," *International Journal of Multiphase Flow,* vol. 19, no. 4, pp. 639-649, 1993.

[31] W. Fullmer, V. Ransom and M. Lopze de Bertodano, "Linear and nonlinear analysis of an unstable, but well-posed, one-dimensional two-fluid model for two-phase flow based on the inviscid Kelvin–Helmholtz instability," *Nuclear Engineering and Design,* vol. 268, pp. 173-184, 2014.

[32] M. Ishii and K. Mishima, "Two-fluid model and hydrodynamic constitutive relations," *Nuclear Engineering and Design,* vol. 82, no. 2-3, pp. 107-126, 1984.

[33] D. Drew, "Mathematical modeling of two-phase flows," *Annual Review of Fluid Mechanics* , vol. 15, pp. 261-291, 1983.

[34] C. Morel, Mathematical Modelling of Disperse Two-Phase Flows, New York: Springer, 2005.

[35] N. Zuber, "On the dispersed two-phase flow in the laminar flow regime," *Chemical Engineering Science,* vol. 19, no. 11, pp. 897-917, 1964.

[36] J. Stuhmiller, "The influence of interfacial pressure forces on the character of two-phase flow model equations," *International Journal of Multiphase Flow,* vol. 3, no. 6, pp. 551-560, 1977.

[37] S. Antal, R. Lahey and J. Flaherty, "Analysis of phase distribution in fully developed laminar bubbly two-phase flow," *International Journal of Multiphase Flow,* vol. 17, no. 5, pp. 635-652, 1991.

[38] M. Lopez de Bertodano, R. Lahey Jr. and O. Jones, "Turbulent bubbly two-phase flow data in a triangular duct," *Nuclear Engineering and Design,* vol. 146, no. 1-3, pp. 43-52, 1994.

[39] R. Auton, "The lift force on a spherical body in a rotational flow," *Journal of Fluid Mechanics,* vol. 183, pp. 199-218, 1987.

[40] A. Tomiyana, H. Tamai, I. Zun and S. Hosokawa, "Transverse migration of single bubbles in simple shear flows," *Chemical Engineering Science,* vol. 57, no. 11, pp. 1849-1858, 2002.

[41] T. Frank, J. Shi and A. Burns, "Validation of eulerian multiphase flow," in *Third International Symposium on Two,* Pisa, 2004.

[42] M. Ishii and T. Chawla, "Local drag laws in dispersed two-phase flow," Argonne National Lab Report, Lemont, Illinois, 1979.

[43] S. Chapman and T. Cowling, The Mathematical Theory of Non-uniform Gases: An Account Of The Kinetic Theory Of Viscosity, Thermal Conduction And Diffusion In Gases, New York: Cambridge University Press, 1991.

[44] A. Alajbegovic, D. Drew and R. Lahey Jr., "An analysis of phase distribution and turbulence in dispersed particle/liquid flows," *Chemical Engineering,* vol. 174, no. 1, pp. 85-133, 1999.

[45] N. Carnahan and K. Starling, "Equations of state for non-attracting rigid spheres," *Journal of Chemical Physics,* vol. 51, no. 2, pp. 635-636, 1969.

[46] A. Vaidheeswaran, "Well-posedness and convergence of cfd two-fluid model for bubbly flows (PhD Thesis)," Purdue University , West Lafayette, 2015.

[47] Y. Sato, "Liquid velocity distribution in two-phase bubble flow," *International Journal of Multiphase Flow,* vol. 2, no. 1, pp. 79-95, 1975.

[48] S. B. Pope, Turbulent Flows, Cambridge: Cambridge University Press, 2000.

[49] P. Gaskell and A. Lau, "Curvature-compensated convective transport: SMART, a new boundedness-preserving transport algorithm," *International Journal for Numerical Methods in Fluids,* vol. 8, pp. 617-641, 1988.

[50] N. Waterson and H. Deconick, "Design principles for bounded higher-order convection schemes - a unified approach," *Journal of Computational Physics ,* pp. 224-182, 2007.

[51] S. Gottileb and C. W. Shu, "Total variation diminishing runge-kutta schemes," *Mathematics of Computation,* vol. 67, no. 221, pp. 73-85, 1998.

[52] R. Sliger and G. Whitham, "Variational principles in continuum mechanics," *Proceedings of The Royal Society A,* vol. 305, no. 1480, pp. 1-25, 1968.

[53] A. Bedford and D. Drumheller, "A variational theory of immiscible mixtures," *Archive for Rational Mechanics and Analysis,* vol. 68, no. 1, pp. 37-51, 1978.

[54] A. Clausse, "Lagrangian-density derivation of the equations of single-fluid and two-fluid Flows," *International Journal of Heat and Technology,* vol. 21, pp. 13-20, 2003.

[55] P. Zilsel, "Liquid Helium II : The hydrodynamics of the Two-Fluid Model," *Physical Review,* vol. 79, no. 2, pp. 309-313, 1950.

[56] M. Bentwich and T. Miloh, "On the exact solution for the two-sphere problem in axisymmetrical potential flow," *Journal of Applied Mechanics,* vol. 45, pp. 463-468, 1978.

[57] L. Shemer, A. Gulitski and D. Barnea, "On the turbulent structure in the wake of Taylor bubbles rising in vertical pipes," *Physics of Fluids,* vol. 19, no. 3, pp. (03518) 1-13, 2007.

[58] M. Ishii and T. Hibiki, Thermo-fluid Dynamics of Two-Phase Flow, New York: Springer Science+Business Media, 2006.